Design of the Cherenkov TOF whole-body PET scanner using GATE simulation

Marharyta Alokhina

université PARIS-SACLAY

NNT : 2018SACLS279

Thèse de doctorat

Design of the Cherenkov TOF whole-body PET scanner using GATE simulation

Thèse de doctorat de l'Université Paris-Saclay et de Taras Shevchenko National University of Kyiv
préparée à l'Université Paris-Sud au sein du CEA-Saclay

Ecole doctorale n°576 Particules, Hadrons, Énergie, Noyau, Instrumentation, Imagerie, Cosmos et Simulation (PHENIICS)
Spécialité de doctorat: Imagerie médicale et radioactivité

Thèse présentée et soutenue à Gif-sur-Yvette, le 20 Septembre 2018, par

Marharyta Alokhina

Composition du Jury :

Achille Stocchi Professeur, Université Paris-Sud, Directeur de Recherche, Laboratoire de l'Accélérateur Linéaire	Président
Gérard Montarou Directeur de Recherche, CNRS, Laboratoire de Physique de Clermont-Ferrand	Rapporteur
Klaus Peter Schäfers Professeur, Westfälische Wilhelms-Universität Münster	Rapporteur
Oleg Bezshyyko Professeur, Taras Shevchenko National University of Kyiv	Examinateur
Viatcheslav Sharyy Ingénieur-chercheur, IRFU, CEA	Directeur de thèse
Igor Kadenko Professeur, Taras Shevchenko National University of Kyiv	Co-directeur de thèse

To my parents

Contents

List of abbreviations and acronyms

CRC ... contrast recovery coefficient

CRT ... coincidence resolving time

CT ... computed tomography

DOI ... depth of interaction

DQR ... dark count rate

FOV ... field of view

GATE ... Geant4 Application for Tomographic Emission

IRFU ... Institute of Research into the Fundamental Laws of the Universe

kcps ... kilo counts per second

LOR ... line of response

MCP ... micro-channel-plate

MLEM ... Maximum Likelihood Expectation Maximization

MRI ... Magnetic Resonance Imaging

NEMA ... National Electrical Manufacturers Association

OP-OSEM ... Ordinary Poisson Ordered-Subset Expectation Maximization

PET ... positron emission tomography

PMT ... photo-multiplier tube

ROI ... region of interest

SiPM ... silicon photo-multiplier

SNR ... signal-to-noise ratio

TOF ... time-of-flight

TTS ... transit time spread

Résumé

Dans cette thése, nous présentons la conception et l'étude de performance d'un tomographe par émission de positrons (TEP) corps entier utilisant la radiation Tchérenkov avec et sans capacité de temps-de-vol. Nous les comparons aux paramètres correspondants de la machine TEP commerciale Discovery D-690 de General Electrics. Nos résultats sont basées sur des simulations GATE et tiennent en compte des recommandations du Standard NEMA NU 2-2007 pour les scanners TEP.

Le logiciel GATE est un logiciel de simulation Monte Carlo développé par la collaboration OpenGATE sur la base du logiciel Geant4. Il permet de simuler les installations de tomographie par émission de positrons, la tomographie par transmission, la radiothérapie et l'imagerie optique. En particulier, il permet de mener des études complexes commençant par le suivi de chaque particule dans le cristal jusqu'à la prédiction finale de réponse du détecteur.

De plus, nous avons calculé nos images TEP à l'aide de l'algorithme de reconstruction MLEM implémenté dans le logiciel "open-source" CASToR développé par la collaboration française. La qualité d'image (plus précisément, les coefficients de récupération du contraste) est comparable à la qualité d'image permises par le scanner TEP conventionnel.

Le Chapitre 1 passe en revue la tomographie par émission de positrons en tant que technique de médecine nucléaire. La premier paragraphe est consacré au principe fondamental de la tomographie, qui repose sur la désintégration β^+ du traceur radioactif. Le positron émis s'annihile avec un électron du tissu. Deux rayons gamma de 511 keV sont émis "dos-à-dos" et peuvent être enregistrés en coïncidence par la paire de détecteurs dédiés. Les lignes de réponse (LOR) relient les points de détection des deux photons et permettent de reconstruire la distribution de traceur lorsque un nombre de coïncidences suffisant est accumulé. Typiquement un examen dure 20 minutes avec un taux de comptage de quelques millions de coïncidences par seconde. Dans le deuxième paragraphe, les avantages et les limites de trois configurations de scanners TEP sont examinés: les scanners pour petits animaux, les scanners cérébraux et les scanners corps entier. À titre d'exemple, les paramètres géométriques du scanner commercial corps entier, Discovery D-690 de General Electrics, sont présentés. Le troisième paragraphe décrit la procédure de production d'isotopes pour le TEP, y compris le principe de fonctionnement du cyclotron, la configuration de la source d'ions et la production d'émetteurs de positrons.

La quatrième partie du Chapitre 1 est consacrée décrit les processus physiques intervenant dans le TEP, tels que la désintégration des positrons, l'interaction des photons de haute énergie avec la matière (l'effet photoélectrique et la diffusion Compton et l'atténuation correspondant du nombre de photons, l'interaction des photons

optiques avec la matiére. Enfin, le modéle UNIFIED de Geant4 est d'ecrit car nous l'utilisons pour simuler la propagation des photons optiques (réflexion, réfraction, absorption). À la fin du Chapitre 1, un cas particulier d'interaction des particules chargées avec la matiére, le rayonnement de Tchérenkov est décrit en détails.

Le Chapitre 2 décrit une revue de l'instrumentation pour la TEP. Le premier paragraphe examine les paramètres principaux des détecteurs pour la TEP, tels que la sensibilité, l'énergie, les résolutions spatiales et temporelles. Les deuxième et troisième paragraphes décrivent respectivement les approches conventionnelles (basées sur les cristaux scintillants) et non conventionnelles (utilisant d'autres matériaux de détection tels que liquides et gaz). Le quatrième paragraphe est consacré à l'acquisition de données et au format de données utilisées en TEP. Plus précisément, les définitions de l'événement unique (single) dans TEP, trois types de coïncidences (true, random et scatter) et, en outre, les régles de sélection de coïncidences disponibles dans GATE sont présentés. Dans la cinquième partie du Chapitre 2, deux algorithmes de reconstruction d'image en TEP, analytique et itératif, sont discutés. En particulier, le logiciel CASToR qui est utilisé pour la reconstruction d'image implémentes les algorithmes de reconstruction itératives. Le sixième paragraphe décrit la normalisation de données et trois types de corrections utilisés dans la TEP, à savoir, les corrections d'atténuation, de diffusion et les corrections de coïncidences fortuites. L'application de ces corrections est nécessaire pour obtenir une image d'une bonne qualité. Tout d'abord, les photons d'annihilation situés à différents endroits du corps du patient ou du fantôme traversent différentes épaisseurs et s'atténuent donc différemment selon le chemin. Le scanner TEP typique contient des milliers de cristaux disposés en blocs et reliés à plusieurs centaines de PMT. En raison des variations du gain des PMT et de la variation des paramètres physique du détecteur, l'efficacité de détection varie d'une paire de détecteur à l'autre, ce qui entraîne une non-uniformité des données brutes. Une procédure de normalisation est utilisée pour réduire cet effet. Les coïncidences fortuites sont dues à une coïncidence aléatoire de photons de deux désintégrations différentes. Les coïncidences fortuites créent un arrière-plan non corrélés d'une image TEP acquise et diminuent donc le contraste d'image si aucune correction n'est appliquée aux données. La section suivante, discute des quatre axes principaux d'amélioration de l'imagerie TEP: reconstruction de la profondeur d'interaction (DOI), passage de l'imagerie 2D à l'imagerie 3D, utilisation des modalités combinées avec TEP, telles que la tomodensitométrie ou l'imagerie par résonance magnétique. Le Chapitre 2 se termine par une présentation du principe de la technique du temps de vol.

Le Chapitre 3 présente les résultats de simulation obtenus dans cette thèse. Il commence par une description du logiciel de simulation GATE. Dans le deuxième paragraphe, notre choix du fluorure de plomb cristallin (PbF_2) comme radiateur Tchérenkov est expliqué. L'histoire de l'utilisation du PbF_2 pour la détection de

particule et de ses propriétés y est présentée. L'attention principale est portée sur l'analyse des processus internes dans le cristal PbF_2. Nous avons analysé les propriétés des particules générées sur chaque étape de la production et de leur transport dans le cristal. En particulier, nous présentons dans de chapitre la distribution des nombres d'électrons par photon de 511 keV, le spectre d'énergie des électrons générés, la distribution des nombres de photons générés par électron, la distribution des photons générés par électron en cas de photoionisation uniquement (la sélection par une énergie électronique supérieure à 423 keV a été appliquée), le spectre des photons optiques par longueur d'onde générée dans un cristal de fluorure de plomb. Le principe de photodétection, le mode de fonctionnement et les principales caractéristiques du photomultiplicateur à micro-canaux (MCP-PMT) sont examinés dans la troisiéme partie du Chapitre 3.

Un paramètre crucial de la simulation est la description de l'interface optique entre le cristal de fluorure de plomb et la surface de la photocathode. Nous avons examiné deux options possibles pour l'interface optique: 1) le collage ("adhérence") moléculaire est simulé comme une absence de tout media entre le cristal PbF_2 et la fenêtre PMT et la distance entre le cristal et la fenêtre est égale à zéro; 2) L'usage de gel optique OCF452 (densité 2.33 g/cm^3, transparent pour les photons de longueur d'onde λ supérieure à 300 nm, indice de réfraction de 1.572 à 400 nm).

Pour réduire les pertes de photons à l'interface optique dans le cas du collage moléculaire, nous avons simulé la fenêtre PMT faite avec le saphir d'épaisseur 1.3 mm car ce matériau présente un indice de réfraction similaire à celui du cristal PbF_2. Nous avons également inclus dans les simulations l'efficacité quantique d'une photocathode bialcaline et deux options pour l'efficacité d'absorption des photons optiques: un cas idéal avec une efficacité quantique de 100 % et réaliste, extrait de la fiche technique.

Dans le cas du collage moléculaire, nous avons observé que nous détectons un nombre significatif de photons de longueur d'onde 250 - 300 nm, ce qui n'est pas possible si le gel optique est utilisé en raison de son manque de transparence. Le nombre correspondant de photoélectrons générés à la photocathode est présenté. Comme le montre le spectre, nous devons définir un seuil de détection inférieur à un photoélectron afin d'obtenir une efficacité de dtection supérieure à 30 %. C'est la raison principale pour laquelle, dans ce projet, nous ne pouvons pas d'utiliser les photodetecteur SiPM. En effet, ces détecteurs ont un taux de comptage d'obscurité (DQR) extrêmement élevé, d'environ 100 kHz/mm^2, lorsque le seuil de détection est inférieur à un photoélectron. Cela entraîne un grand nombre de coïncidences fortuites et rend irraliste l'utilisation de SiPM dans un scanner Tchérenkov, sans réduire le DQR, par exemple, par le nouveau design de SiPM, ou par le refroidissement à basses températures.

L'efficacité de collection des photons optiques dépend directement du revêtement

du cristal. Pour étudier l'influence du revêtement de cristal sur l'efficacité totale et la résolution temporelle du scanner, nous avons étudié divers types de revêtement et de traitement de la surface du cristal. Nous avons présenté résultats pour trois types de surface de cristal PbF_2: blanc diffus, noir et poli. Le revêtement blanc diffus réfléchit la lumière de manière uniforme et indépendamment de l'angle d'incidence avec une probabilité d'environ 95 %. La surface noire absorbe 100 % de la lumière incidente et seul les photons optiques qui vont directement à la photocathode à partir du point d'interaction peuvent être enregistrés. De ce fait, la dispersion de la longueur des parcours de photons est minimale et la résolution en temps est optimisée, au prix d'un rendement faible, car seul un petit nombre de photons est enregistré. Pour le revêtement poli, les photons suivent la lois de Fresnel de transmission et de réflexion et les surfaces sont peintes en blanc sur la face arrière, avec une probabilité de réflexion de 95 %.

Nous avons estimé la résolution en temps (coincidence resolving time or CRT) pour trois types de revêtement de cristal avec une source radioactive ponctuelle placée au centre entre deux cristaux. Nous avons constaté que le revêtement noir permet d'atteindre des résolutions en temps "optiques" extrêmement élevées, mais les technologies PMT actuelles ne nous permettent pas de l'utiliser pleinement, et le détecteur final sera limité par le temps de transit (TTS) du PMT. En plus, cette configuration a une efficacité presque trois fois plus faible que les deux autres, ce qui dégrade les performances du scanner. Nous avons simulé une épaisseur de cristal deux fois plus élevée (20 mm). Nous observons une dégradation considérable du CRT, et l'amélioration modeste de l'efficacité de la détection.

Enfin, sur la base de nos résultats avec deux cristaux, nous avons simulé le scanner dans une configuration corps entier. Nous avons choisi d'associer un seul cristal PbF_2 à chaque anode du MCP-PMT, et donc chaque module de détection est composé d'un PMT et de 64 cristaux de taille $6.5 \times 6.5 \times 10$ (20) mm^3, collés ensemble. Nous avons supposé que chaque cristal individuel est optiquement isolé des voisins et sa surface est de type blanc diffus. La configuration avec trois anneaux de détection donne un champ de vue (FOV) axial de 180 mm. Nous avons testé deux diam'etres d'anneau de détecteur de 81 cm et 91 cm. Chaque anneau est constitué de 43 ou 48 blocs de détection et pour les diamètres de 81 cm et 91 cm, le nombre total de PMT est en conséquence de 129 ou 144. Le nombre total de cristaux est de 8256 ou 9216. Nous avons constaté que le taux de "noise equivalent count" (NECR) est optimal pour un diamètre de 81 cm. Nous avons également édié l'option d'un blindage de plomb pour protéger le scanner des photons hors FOV. Nous avons constaté qu'un blindage en forme d'anneau avec un diamètre intérieur de 70 cm, un diamètre extérieur de 108 cm et une épaisseur de 3 cm réduit la contribution en dehors du FOV et améliore NECR de 20 %.

Le Chapitre 4 conclut les études réalisées et présente l'estimation de la perfor-

mance TEP envisagée, en particulier: calcul de CRT, de NECR, des coefficients de recouvrement de contraste (CRC) et de la résolution spatiale du scanner simulé conformément au norme NEMA NU 2-2007. Le premier paragraphe décrit le test pour une estimation plus réaliste du CRT lorsque l'écart TTS du temps PMT de 80 ps est pris en compte. Nous avons simulé un fantôme de test en polyéthylène, identique à celui utilisé pour le calcul du NECR. Comme on pouvait s'y attendre, les meilleures performances sont obtenues pour le cristal de 10 mm d'épaisseur monté par adhérence moléculaire. Nous avons observé une dégradation importante, plus forte que anticipée, dans la configuration avec une épaisseur de cristal de 20 mm. Le troisième paragraphe est consacré à l'estimation de la résolution spatiale du scanner. Nous observons une dégradation entre le centre de FOV à une périphérie de 4,5 à 6,5 mm, qui est comparable à la résolution spatiale du scanner conventionnel Discovery D-690. La configuration en collage mol'eculaire a une résolution spatiale comparable à celle du gel optique et légèrement améliorée lorsque comparée à la résolution spatiale des scanners classiques. Cela s'explique par le fait que dans notre configuration, la taille du cristal et le champ de vue sont similaires à ceux du scanner classique, mais nous utilisons des cristaux de PbF_2 de faibles paisseurs, 10 mm, et donc l'erreur de parallaxe en raison de l'incertitude sur le DOI est plus petite. De plus, le cristal PbF_2 a une fraction photoélectrique deux fois plus élevée que les cristaux LYSO et, donc le nombre d'événements avec deux points de conversion (une diffusion Compton puis une photo-ionisation) est plus petit. La résolution spatiale de tels événements est se dégrade, lorsque ces conversions ont lieu dans les deux cristaux différents.

Le Chapitre 4 se termine par une estimation de la qualité d'image du scanner TEP Tchérenkov. Cette procédure n'est pas triviale en raison des corrélations complexes de plusieurs aspects du systéme. La norme NEMA propose de comparer la qualité d'image des différents systèmes à l'aide d'un fantôme de qualité d'image normalisé simulant une condition d'examen clinique. Le fantôme avec atténuation non uniforme est rempli d'un liquide radioactif représentant léactivité de fond. Il contient quatre sphères "chaudes", ayant une activité 4 ou 8 fois supérieure à celle de l'activité de fond et deux sphères "froides", c'est-à-dire, sans activité. Six sphères avec les diamètres différents sont utilisées pour estimer le recouvrement de contraste après reconstruction d'image, tandis que la région de fond est utilisée pour estimer la variabilité de bruit. L'utilisation des photons Tchérenkov pour la création d'un scanner TEP nécessitera le développement de la correction diffuse, qui dépasse le cadre de la présente étude. Afin de pallier l'absence de corrections diffuses et fortuites, nous avons reconstruit l'image TEP en ne prenant en compte que les vraies coïncidences. La reconstruction d'une telle image peut être vue comme une reconstruction "parfaite" de toutes les coïncidences lorsque des corrections fortuites et de dispersion parfaites seront appliquées. Nous avons observé que le contraste recon-

struit est plus petit que pour le scanner conventionnel, mais la valeur obtenue reste raisonnable pour identifier toutes les sphères de contraste élevé (8 fois de bruit de fond) et identifier les deux plus importants au contraste faible (4 fois de bruit de fond).

L'étude présentée dans ce manuscrit a démontré que l'efficacité de détection à base de processus Tchérenkov (relativement peu lumineux) est compensée par le gain obtenu par la technique de temps-de-vols. Le scanner Tchérenkov peut être utilisé en PET et atteindre des performances équivalentes à la technologie conventionnelle basée sur les cristaux à scintillation. Même si les performances du scanner Tchérenkov ne sont pas suffisamment motivante actuellement, nous nous attendons à ce queavec l'amélioration des technologies de photodétection et, en particulier, de la résolution en temps des PMT, cette approche devienne plus intéressante soit en utilisant des radiateurs Tchérenkov purs, soit utilisant des cristaux scintillants avec une production significative de lumière Tchérenkov.

Abstract

In this PhD thesis we have designed and estimated main characteristics of the foreseen whole-body Cherenkov PET scanner with and without TOF potential and compared them with corresponding parameters of the commercial PET machine Discovery D-690 by the General Electrics. Our results are based on the various modelings in the GATE simulation software and take into account the recommendations of the NEMA NU 2-2007 Standard for PET scanners.

The code GATE (Geant4 application for emission tomography, transmission tomography, radiotherapy and optical imaging) is a handy Monte Carlo tool developed by the OpenGATE collaboration which allows to hold a complex investigation from tracking every single particle inside the crystal to the final prediction of the integral detector response.

In addition, we have reconstructed several PET medical images using MLEM reconstruction algorithm via code CASToR developed by Service Hospitalier Frédéric Joliot (SHFJ). The evaluated image quality (more precisely, contrast recovery coefficients) is comparable with image quality provided by conventional PET scanner as was expected.

Chapter 1 reviews the positron emission tomography as nuclear medicine technique in terms of physics. The first paragraph is dedicated to the fundamental principle of the positron emission tomography which is based on β^+ radioactive decay of the tracer. An emitted positron annihilates with an electron of the tissue. As a result of annihilation, two 511-keV gamma rays are emitted back-to-back and may be registered by the dedicated pair of detectors. The line-of-response (LOR) joins two points where photons are detected and allows to reconstruct the tracer distribution when sufficient number of LORs are accumulated. The typical rate for PET scanning is millions LORs per second. In the second paragraph three types of the PET scanners, namely small-animal PET scanners, brain PET scanners and whole-body PET scanners, their advantages and limitations are considered. As an example for comparison geometrical parameters of the commercial whole-body hybrid PET scanner Discovery D-690 by General Electrics were presented. The description of the procedure of the isotope production for PET including the principle of the operation of a cyclotron, the ion source configuration and the positron emitter production are given in the third paragraph. The fourth part of Chapter 1 is dedicated to the theory of the physical processes in PET such as a positron decay, interaction of the high energy photons with matter (photoelectric and Compton scattering effects, disregarding the pair production because energy of 511 keV is not enough) attenuation of photons, interaction of optical photons with matter (a photon is considered to be optical when its wavelength is much greater than the typical atomic spacing), Rayleigh and Mie scattering. At last, the UNIFIED model was described because

the medium boundary interactions in the Geant4 and the GATE employ this model. At the end of Chapter 1 the Cherenkov radiation was considered as a particular case of the charged particles interaction with matter.

Chapter 2 outlines a review of the instrumentation in PET. The first paragraph considers the general parameters of the detectors for PET such as sensitivity, energy, spatial and timing resolutions. The second and third paragraphs describe the conventional (based on scintillator crystals) and non-conventional (based on another detection materials such as liquids and gases) approaches respectively. The fourth paragraph is dedicated to data acquisition and data format in PET. More precisely, the definitions of the single event in PET, three types of coincidences (true, random and scatter) and, in addition, the coincidence policies available in the GATE are given. In the fifth part of the second Chapter two image reconstruction algorithms in PET, analytical and iterative, are discussed. The code CASToR was used for image reconstruction. The sixth paragraph includes the normalization and three types of corrections normally used in PET, namely attenuation, scatter and random corrections. The application of these corrections is necessary because of their influence on the reconstructed data. First of all, the annihilation photons from different locations in the patient body or phantom traverse different thicknesses, thus, they attenuate differently by the media before arrival to the detection surface. Secondary, PET scanner consists of thousands of detection crystals arranged in blocks and attached to several hundred PMTs. Because of the variations in the gain of PM tubes, the location of the detector in the block, and the physical variation of the detector, the detection efficiency of a detector pair varies from pair to pair, resulting in non-uniformity of the raw data. The procedure designed to reduce this effect is called the normalization. Thirdly, due to a large coincidence timing window and the enormous number of lines-of-response the random coincidences exist. They arise when two unrelated photons enter the opposing detectors and are temporally close enough to be recorded within the coincidence timing window. For such events, the system produces a false coincident event. Random coincidences add the uncorrelated background counts to an acquired PET image and hence decrease the image contrast if no corrections are applied to the acquired data. Four main directions of the improvement in PET: reconstruction of the depth of interaction (DOI), the transition from 2D-PET to 3D-PET imaging, the usage of the combined modalities such as Computer Tomography (CT) and Magnetic Resonance Imaging (MRI) with PET are discussed in the seventh paragraph. Chapter 2 ends with the basic principle of the time-of-flight technique.

Chapter 3 reports our simulation results. It begins with a description of the GATE simulation software and explicates our choice of the Cherenkov radiator in the second paragraph. The history of discovery of lead fluoride crystal and its properties are shown there. The main attention is paid to analysis of the inner

processes in the PbF_2 crystal. We have tracked each generated particle and every interaction inside the detector material step by step. The distribution of the numbers of the electrons per each 511-keV gamma, the energy spectrum of the generated electrons, the distribution of the numbers of generated photons per single electron, the distribution of generated photons per electron in case only photoionization (the selection by electron energy bigger than 423 keV was applied), the spectrum of the optical photons by wavelength generated into lead fluoride crystal were shown in this part of the thesis. The definition of the procedure of photodetection, the mode-of-operation and main characteristics of the micro-channel-plate photomultiplayer (MCP-PMT) were discussed in the third part of Chapter 3.

The crucial part of the simulation is the description of the optical interface between lead fluoride crystal and the surface of the photocathode. We have considered two possible options of the optical interface: 1) molecular bonding, which is simulated as an absence of any media between PbF_2 crystal and PMT window, in the simulation it is possible if distance equals zero; 2) interface with the optical gel OCF452 (density 2.33 g/cm^3, transparent for photons with wavelength λ bigger than 300 nm, refractive index 1.572 at 400 nm)

For decreasing losses of the optical photons at the optical interface in the case of the molecular bonding, we simulated the sapphire layer of 1.3mm as an optical window because this material has the similar refractive index compare to PbF_2 crystal. Also we have included in the simulations the Bialkali photocathode with the thickness of 0.1 mm and two options for absorption efficiency of the optical photons, an ideal case with 100 % and realistic quantum efficiency which was taken from datasheet.

We have observed that we detect a significant number of photons below wavelength of 300 nm, which is not possible if the optical gel is in use due to its transparency. The corresponding number of photoelectrons, generated at the photocathode is presented. As far as the spectrum is considered, we need to provide a detection threshold below one photoelectron in order to have a reasonable detection efficiency above 30 %. This is the main reason, why in this project we could not consider the use of the SiPM. Indeed, those detectors has an extremely high dark count rate (DQR), about of 100 kHz/mm^2, when detection threshold is below one photoelectron. This leads to the huge number of the random coincidences and make the use of SiPM in Cherenkov scanner unrealistic, without reducing the DQR either by the new SiPM design or by cooling it down.

The ability of the optical photon collection directly depends on the crystal coating. For investigation the influence of the crystal coating on the total efficiency and timing resolution of the scanner, we have provided the probability options for various reflection types, including possible irregularities of the surface, e.g. surface roughness. We have considered three different types of the PbF_2 crystal process-

ing: diffuse white, black and polished. The diffuse white coating reflects the light uniformly and independently of the incidence angle with probability of about 95 %. The black surface absorbs 100 % of incident light and only optical photons which go directly to the photocathode from the interaction point. Thereby, the photon dispersion is the minimal and the best timing resolution can be achieved but with low efficiency, because only a small number of the generated photons has no reflection. The polished coating obeys the Fresnels laws for transmission and reflection, the angle of reflection is equal to the angle of incidence. In this case we have simulated a polished-back-painted optical surface with 95 %-reflectivity.

We have estimated the CRT for three different crystal coatings with point-like radioactive source placed in the center of field-of-view (FOV). We have observed that the black coating allows to reach extremely high CRT performance, but current PMT technologies do not allow us to use it fully, and final CRT will be limited by the Transit Time Spread (TTS) of the PMT. Additionally, this configuration, has almost 3 times lower efficiency, that will degrade the scanner performance. The increasing the thickness by a factor of two degrades significantly the CRT performance, but improves the detection efficiency only marginally.

Finally, according to our results with two back-to back crystals we have simulated the whole-body scanner geometry. We chose to associated a single PbF2 crystal to each anode of the MCP-PMT. It results in the detection modules made with one PMT and 64 crystals with the size 6.5 $\times$ 6.5 $\times$ 10 (20) mm^3, glued together. We have assumed, that each individual crystal is optically isolated from the neighbors and has the diffuse white surface as described above. The configuration with three detector rings gives the axial FOV of 180 mm. We have tested two ring diameters 81 cm and 91 cm. We found that the optimal NECR characteristics are for the diameter 81 cm. Each ring consists of 43 or 48 detection blocks and for 81 cm and91 cm diameters the total number of PMT is 129 or 144 correspondingly. The total number of crystals is 8256 or 9216. We have also studied the lead shielding option for protecting the scanner from the out-of-FOV photons. We found that an annulus-shape shielding with the internal diameter of 70 cm, external diameter of 108 cm and thickness of 3 cm reduces the out-of-FOV contribution by a factor of 0.2.

Chapter 4 concludes the performed studies and outlines perspectives for the being foreseen PET performance estimation based on the CRT, Noise Equivalent Count Rates (NECR) calculation, contrast recovery coefficients (CRC) and spatial resolution of the scanner according to the NEMA NU 2-2007.

The first paragraph describes the test for more realistic CRT estimation of the performance when the TTS of PMT of 80 ps was taken into account. We have simulated a polyethylene test phantom, the same as was used for the NECR calculation and shown in the second paragraph. As was expected, the best CRT performance is obtained for a 10 mm thick crystal with molecular bonding. We have observed a

significant degradation, more than expected, for the configuration with the crystal thickness of 20 mm. The third paragraph is dedicated to estimation of the spatial resolution of the scanner. It degrades from the center FOV to a periphery from 4.5 to 6.5 mm on each axis respectively and comparable with spatial resolution of the conventional scanner Discovery D-690. The estimated uncertainty is about half of the voxel size, i.e $\pm$ 0.25 mm. The configuration with molecular bonding has spatial resolution comparable with optical gel configuration and slightly better than spatial resolution of the conventional scanners. This is explained by the fact that in our configuration the crystal size and FOV are similar to the conventional scanner, but we study the PbF_2 crystal with small thickness, 10 mm, and hence smaller parallax error due to the uncertainty on DOI. In addition, PbF_2 crystal has a two times higher photo-electric fraction than LYSO crystals and, consequently, the number of events with two conversion points (one Compton scattering and one photo-ionization) is smaller. Such events with two conversion points have worse spatial resolution, when if these conversions happen in the different crystals.

Chapter 4 ends with prediction of the image quality of the foreseen Cherenkov PET scanner. It is non-trivial procedure due to the complex interplay of many different aspects of the system performance. The standard NEMA proposes to compare the image quality of different systems using a standardized image quality phantom that simulates a clinical imaging condition. The proposed phantom with non-uniform attenuation is filled with background activity. It contains four hot spheres, e.g. spheres with activity significantly higher than the background one, and two cold spheres, e.g. spheres with no activity. Six spheres have different diameters and are used to estimate the contrast recovery after the image reconstruction, while background region is used to estimate the background variability.

The usage of the Cherenkov photons for creation a PET scanner requires another development of the random correction, which goes beyond the scope of the current study. In order to mitigate the absence of the scatter and random corrections, we reconstructed the PET image by taking into account only true coincidences. Indeed, the reconstruction of such image could be viewed as a reconstruction of all coincidences when perfect random and scatter corrections are applied. We can reasonably expect that the result of the image reconstruction with random and scatter corrections will be located somewhere between two boundary cases: (1) image produced by all coincidences without any corrections and (2) image created by only true coincidences. As was expected, the increasing of quantity of iteration increases the CRC, but at the cost of the larger background fluctuations. We have studied the influence of the reconstruction parameters such as number of iterations and subsets on the image quality.

The study presented in this manuscript demonstrated that the Cherenkov detection technology could reach the equivalent or even better performance than the

conventional technology based on the scintillation crystals. In particular, we have estimated that the TOF NECR values of the foreseen Cherenkov scanner are comparable or even better than ones reached by the commercial machine. The image quality parameters, i.e., contrast recovery versus background fluctuation are slightly worse than the chosen example of the commercial scanner, but this comparison still requires further optimization of the reconstruction parameters.

Introduction

Positron emission tomography (PET) is a powerful nuclear imaging technique widespread nowadays in Oncology, but also in Cardiology and Neuropsychiatry [1]. The PET technology, which is aimed at the observing of the metabolic processes in the tissue and diagnosing of disease, uses an intravenous injecting of a radioactive tracer to a patients body. Nowadays more than 200 various radioactive tracers are available at the global pharmaceutical market and their usage mainly depends on their physicochemical properties and the purpose of the study. When a whole-body scan is performed, an average activity required to obtain an image with a good quality ranges from 3 to 5 MBq/kg (or 150 - 400 MBq in total), which corresponds to an effective dose of about 8 to 25 mSv whole-body PET/CT protocols today for an adult [2]. This circumstance limits the use of the whole-body PET scanning to cases with a positive risk-benefit ratio [3]. One of the main objectives in development of the new PET scanners is radiation dose reducing received by the patient according to the ALARA principle with keeping the same image quality, or, alternatively, improving the image quality without an increase in the received dose.

The first theoretical works on the improvement of the PET imaging by adding the time-of-flight (TOF) information were started in the 1980s [4, 5, 6, 7, 8, 9, 10]. Unfortunately, only during the last decade the first commercial PET scanner was equipped with TOF capability. Recently the best commercially available scanner reaches the CRT of about 325 ps (FWHM) [11]. The standard approach for conventional PET devices is to use the scintillator crystals for gamma detection. As it known, scintillation is a rather slow process and for the fastest scintillators the decay time of the fast component of the signal is of the order of 1 ns, but for crystals widely used in PET it is about 40 ns and more (see Tab. 2.1).

An alternative approach consists of detecting the Cherenkov photons. The 511-keV gamma is converted into an energetic electron through the photoionization or the Compton effects. If the material has a sufficiently large refractive index and consequently small speed of light, the recoil electron is relativistic in the media. In such a condition, the recoil electron produces photons mainly in the blue and ultraviolet ranges. These photons can be detected by a photomultiplier attached to the crystal. The Cherenkov radiation is extremely fast process and optical photons are radiated at the timescale of several picoseconds. This approach allows to achieve very fast detection with the resolution in time limited mainly by two effects: dispersion of the photon pathlengths and time resolution of the photodetector device. One of the best candidate as a Cherenkov radiator is crystalline lead fluoride, PbF_2. It produces no scintillation light, but only the Cherenkov radiation. It has a high density of about 7.8 g/cm^3 and one of the highest photoelectric fraction, 46 % [12]. Due to these properties, it is possible to create an efficient gamma detector with a very thin

crystal of the order of 10 mm thick and hence minimize its length and dispersion of the photon trajectories. The ability to detect 511-keV photons and create the Cherenkov PET module has been demonstrated in the works by Korpar [13, 14, 15]. It was reported, since this crystal radiates only Cherenkov light, the overall number of photons is small and total detection efficiency is limited to 10 % or smaller. This low detection efficiency is a major limiting factor for making very fast TOF-PET devices. The CaLIPSO group at the Institute of Research into the Fundamental Laws of the Universe (IRFU) is doing a feasibility study of using these type of crystals to build a whole-body TOF-PET performance (PECHE project).

Chapter 1

Positron Emission Tomography

1.1 Main Principle

Positron Emission Tomography (PET) is a nuclear imaging technique which allows the detection of very small (pico-molar) quantities of biological substances which are labelled with a positron emitter [16]. Most commonly used radioactive tracers are based on ^{11}C, ^{15}O, ^{13}N, and ^{18}F, but for some special medical reasons other isotopes can be applied. For instance, ^{68}Ga is typically used for brain imaging. The ^{64}Cu metal ion is used for studies involving copper metabolism (Menkes' syndrome and Wilson's disease), nutrition, and copper transport. The radionuclide ^{82}Rb is mainly used in myocardial perfusion studies and evaluation of blood-brain barrier changes in patients with Alzheimer's-type dementia. The advantages of positron labelled substances are their very high specificity (molecular targeting), the possibility of using biological active substances without changing their behavior by the label, and fulfillment of the tracer principle.

The half-live times of the radioactive isotopes involving in PET are within from several minutes (2 min for ^{15}O) to several hours (109 min for ^{18}F), which necessitates a nearby cyclotron and radiochemistry facility. The half-life time should be prolonged enough for injection and distribution of the radioactivity inside the object will be scanned and at the same time not so long, because of the minimization of the dose for the patient (ALARA Principle) [17].

Imaging of the regional tracer concentration is accomplished by the unique properties of positron decay and annihilation (see Tab. 1.1). After the emission from the parent nucleus, the energetic positron traverses a few millimeters distance through the tissue until it becomes thermalized by electrostatic interaction between the electrons and the atomic nuclei of the media and combines with a free electron to form

a positronium. Lower positron energy is encouraged in this case because it leads to smaller positron range in the medium and better spatial scanner resolution. The positronium decays by annihilation, generating a pair of gamma rays which travel in nearly opposite directions with an energy of 511 keV each. The opposed photons from positron decay can be detected by using pairs of collinearly aligned detectors in coincidence (see Fig. 1.1). This is the reason why PET is much more sensitive (factor > 100) than the conventional nuclear medical technique, namely single photon emission tomography (SPECT) using gamma cameras and lead collimators.

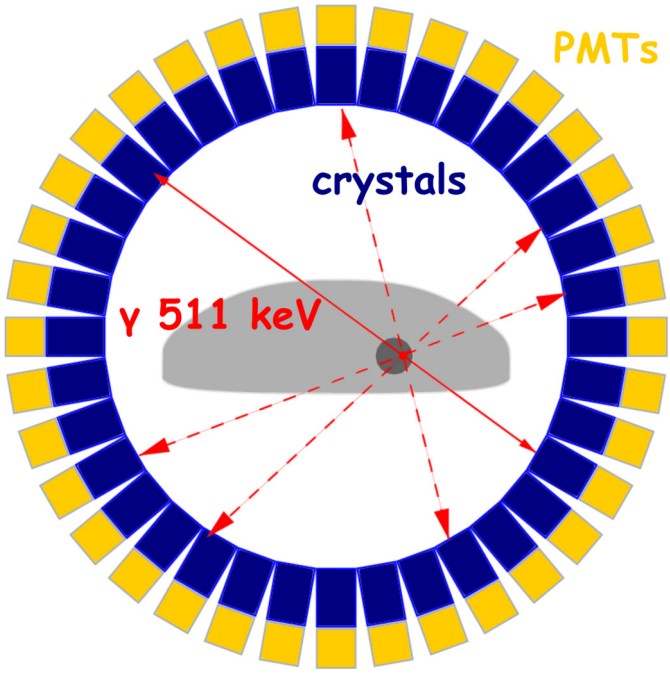

Figure 1.1: Each annihilation produces two 511 keV photons traveling in opposite directions and these photons may be detected by the detectors surrounding the subject. The detector electronics are linked so that two detection events unambiguously occurring within a certain time window may be called coincident and thus be determined to have come from the same annihilation. These coincidence events can be stored in arrays corresponding to projections through the patient and reconstructed.

Various scanner configurations can be used but usually detector pairs of the PET system are installed in a ring-like pattern, which allows measurement of radioactivity along lines through the organ of interest at a large number of angles and radial distances. The purpose of PET measurement is to save the angular-distance information and apply it for image reconstruction in three dimensions (3D PET).

1.2 Types of PET scanners

The parameters of a PET tomograph depend on:
1) the purpose of the study (experimental research machine or conventional medical tomograph),
2) object will be scanned (small animals, brain, whole human body),
3) type of the detection material (liquid, gas, solid crystal),
4) in addition CT or MRI-based modality,
5) with/without TOF capability.

Based on preceding parameters all PET scanners can be divided into three subcategories:

1) *Small-animal PET scanners* are commonly used in different preclinical studies and providing the best image resolution. Typical spatial resolution for this type of scanners is about of 1 mm^3. Because of the importance of animal work in drug development (evaluation of the biodistribution and pharmacokinetic properties of the medicaments *in vivo* in animals prior to their clinical use in humans), several small-animal PET scanners are now commercially available by manufacturers such as Siemens Medical Solutions, General Electrics Healthcare, Bioscan (i.e., see Fig. 1.2) [18].

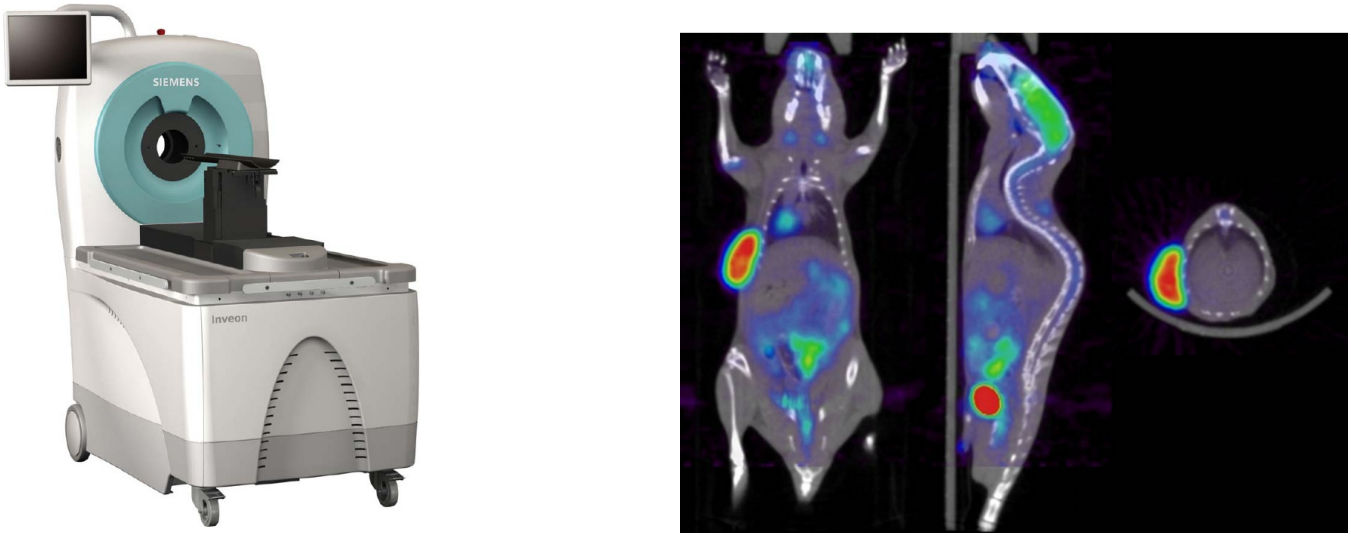

(a) (b)

Figure 1.2: Inveon small-animal PET scanner by Siemens (a) and PET imaging of a rat with tumor (b).

2) For brain cancer diagnosing and for determine different types of dementia in medical routine preferable use *brain-PET scanners* (see Fig. 1.3). They provide a good spatial resolution about of 2.5 mm on each axis [19].

3) *Whole-body PET scanners* have much bigger diameter of the detector's ring

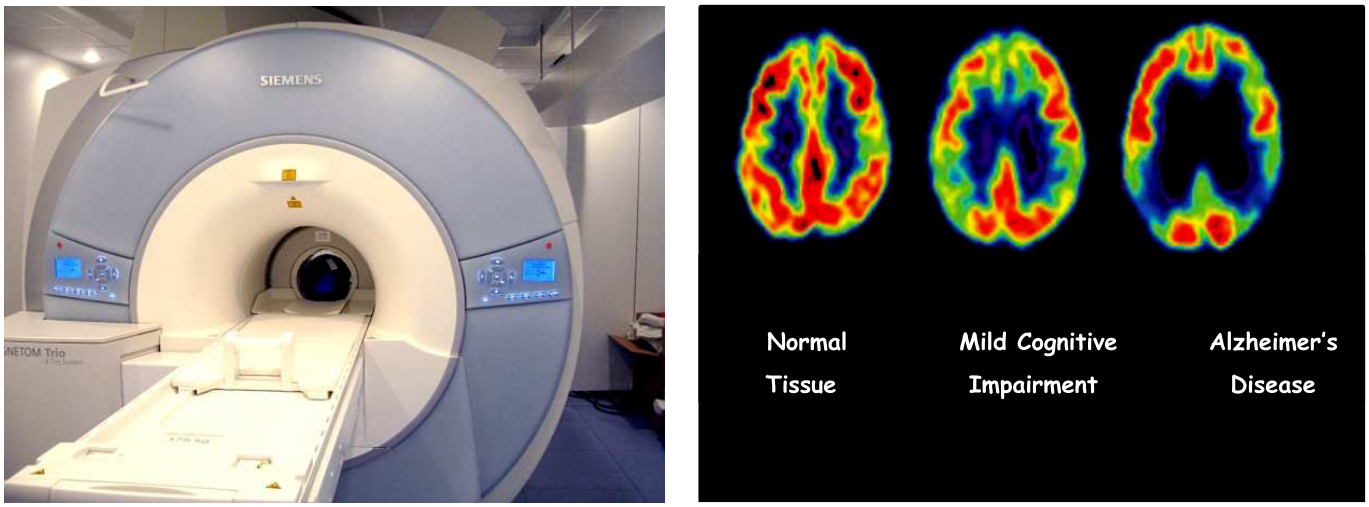

(a) (b)

Figure 1.3: (a) The 3TMR-BrainPET MAGNETOM Tim-Trio hybrid scanner by Siemens [20] and reconstructed brain PET images (b) of normal tissue, with cognitive impairment and with Alzeheimer's disease.

80-90 cm and typical spatial resolution is about of 4-5 mm. In our work we compared the foreseen Cherenkov TOF-PET scanner with conventional PET performance Discovery D-690 by General Electrics (see Fig. 1.4), using publication by Bettinardi et al [21]. This scanner has a multi-ring system design. The Discovery D-690 by General Electrics hybrid tomograph consists of 13 824 LYSO crystals with dimensions of $4.2 \times 6.3 \times 25$ mm^3. The PET detection unit consists blocks of 54 (9×6) individual LYSO crystals coupled to a single squared photomultiplier tube with 4 anodes. The D-690 uses a low energy threshold of 425 keV and a coincidence time window of 4.9 ns. The D-690 consists of 24 rings of detectors for an axial field of view (FOV) of 157 mm. The transaxial FOV is 70 cm. The D-690 operates only in 3-dimensional mode (3D) with an axial coincidence acceptance of 623 planes.

Figure 1.4: The integrated PET/CT system Discovery-D690 by General Electrics is an example of conventional whole-body PET/CT machine.

1.3 Isotopes production

There are three principal methods that are used for production of radioisotopes in nuclear medicine. Radioisotopes can be produced by separation of the by-product produced during fission; they can be produced from neutron irradiation in a reactor; or they can be produced from bombardment of a target material by charged particles from accelerator.

Radioisotope production for PET is generally performed by means of a cyclotron that is used to accelerate charged particles. These accelerated particles then go on to interact with a target to produce radioisotopes suitable for use in PET imaging. A cyclotron is a type of particle accelerator that accelerates charged particles, such as protons and deuterons, to high energies [22].

When a charged particle is in the presence of an electric field, it will feel a force that will accelerate it in the direction of the field. If this acceleration is in the direction that the particle is already traveling in, then it will cause the particle to gain energy. When a charged particle is in the presence of a magnetic field, it feels a force that is perpendicular to its direction of motion. This force will make the particle change its direction, but not its speed. This means that when a charged particle enters a magnetic field, it will start to travel in a circle. The faster the particle is traveling, the bigger the circle it will travel in. A cyclotron takes advantage of these two phenomena and utilizes them to accelerate positively charged particles.

1.3.1 Cyclotron

A cyclotron consists of two semi-circular conducting structures known as dees, with an insulating gap between them (see Fig. 1.5). These dees are placed between two magnets with opposite poles facing each other, so there is a magnetic field traveling from top to bottom. As the charged particles enter the magnetic field, they will travel in a circular motion around the dees [23].

Once the charged particles are traveling in a circular motion, there needs to be a way of accelerating them. An electric field is placed between the surfaces of the two dees, such that when the charged ion exits one dee, it will be repelled by the oppositely charged surface of that dee and attracted to the surface of the second dee. This causes the particle to accelerate and gain energy. As the particle is now traveling at a faster speed, it will move in a larger circle within the second dee. When the particle reaches the surface of the second dee, it needs to be accelerated again, and so the surface of the second dee needs to become oppositely charged while the other surface needs to become charged to attract the particle towards it, creating further acceleration. This means that the direction of the electric field needs to

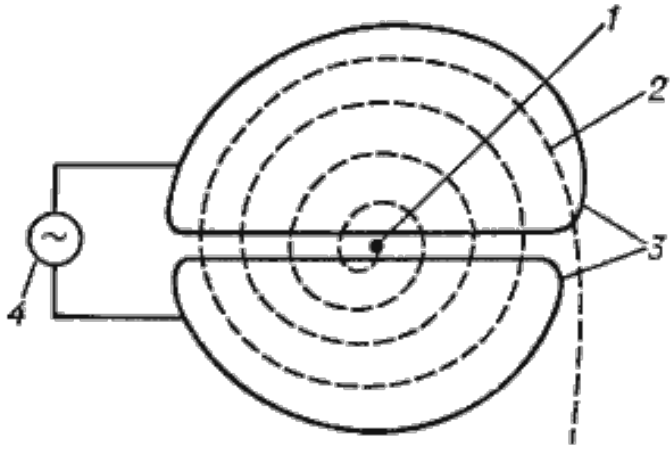

Figure 1.5: Diagram illustrating the operation of a cyclotron: 1 - ion source, 2 - spiral path of accelerated protons, 3 - dees, 4 - frequency oscillator. Magnetic field oriented perpendicular to the dees, not shown.

change just as the particle emerges between the dees. This is achieved by applying a high-frequency alternating voltage across the dee electrodes. The dees themselves are isolated, and so the particles are not affected by the electric field once they are inside. This process is repeated until the particle has accelerated sufficiently, and so is traveling in a large enough circle, to be released from the dees. As this particle is now accelerated, it has gained energy. This energy is then used to interact within a target to create radioisotopes.

Due to the radiation protection issues involved in the production and disposal of radioactive materials, radiotracer production and cyclotron operation are mostly automated. This is normally achieved via a computer-controlled menu that the operator employs to select the isotope for use. Cyclotrons also need a lot of internal shielding to protect staff from high radiation doses, not only from the positron emitters but also from the by-products that are produced [24].

There are two ways of providing this shielding. One is vault shielding, where the cyclotron is housed in a protected room with concrete walls. The second is incorporation of the shielding in the cyclotron, which is referred to as "self-shielded". In this option the steel frame of the cyclotron provides the primary shielding, with concrete blocks that are hydraulically driven providing complete radiation protection. The advantages of self-shielded cyclotrons are they have a smaller footprint and so require less space and there are fewer decommissioning implications.

1.3.2 Ion source

For these events to occur there has to be a source of ions, and the ion source is dependent on the isotope that is being produced, as different isotopes need different

interactions between target and particle. The ion source is a small chamber in the center of the cyclotron that produces either negative or positive ions, depending on the configuration. These particles are attracted into the dees by electrostatic attraction [23]. Negative hydrogen ions (H^-) are produced by using a tungsten filament to ionize hydrogen gas. The electrons are stripped off the H^- particle using a carbon foil, leaving an accelerated proton to interact within the target.

The exiting charged particles are directed to the required target using a deviating electromagnet. This means that different isotopes can be produced using the same cyclotron depending on the target used.

1.3.3 Positron emitter production

Once charged particles exit the cyclotron, they can go on to produce positron emitters by interacting with a target. The isotope that is produced depends on the typed of charged particle that has been accelerated and the material from which the target is made.

While many different radioactive isotopes can be produced in the cyclotron, in order to be suitable for PET imaging they must have the following properties:

- Emit positrons when they decay;
- Have an appropriate half-life time;
- Be capable of being synthesized into a pharmaceutical to produce a useful tracer for studies in humans.

When targets of stable elements are irradiated by placing them in the beam of accelerated particles, the particles interact with the nuclei within the target and nuclear reactions take place. The following nuclear reactions induced by a proton p, on a target ${}^{A}_{Z}X$ can be given by:

$$ {}^{A}_{Z}X + p \rightarrow {}^{A}_{Z+1}Y + n \tag{1.1} $$

$$ {}^{A}_{Z}X + p \rightarrow {}^{A-3}_{Z-1}Y + \alpha \tag{1.2} $$

For example, ${}^{18}F$ is produced by proton bombardment ${}^{18}O$-enriched water:

$$ {}^{18}O + p \rightarrow {}^{18}F + n \tag{1.3} $$

A proton interacts with the ${}^{14}N$ and produces α particle and ${}^{11}C$:

$$ {}^{14}N + p \rightarrow {}^{11}C + \alpha \tag{1.4} $$

^{13}N is produced by proton bombardment of distilled water:

$$^{16}O + p \rightarrow {}^{13}N + \alpha \tag{1.5}$$

A reaction induced by a deuteron d, on a target ${}^{A}_{Z}X$ can be given by:

$${}^{A}_{Z}X + d \rightarrow {}^{A+1}_{Z+1}Y + n \tag{1.6}$$

For instance, ^{15}O radionuclide production:

$$^{14}N + d \rightarrow {}^{15}O + n \tag{1.7}$$

Nuclide	E_{max}, MeV	$T_{1/2}$, min	Range in water, mm	
			Max	Mean
^{11}C	0.959	20.4	4.1	1.1
^{13}N	1.197	9.96	5.1	1.5
^{15}O	1.738	2.03	7.3	2.5
^{18}F	0.633	109.8	2.4	0.6

Table 1.1: Properties of the main positron-emitting nuclides of interest in PET [25].

1.4 Physics in PET

1.4.1 Positron decay

Positron emission from the nucleus is radioactive decay described by:

$${}^{1}_{1}p^{+} \rightarrow {}^{1}_{0}n + {}^{0}_{1}\beta^{+} + \nu_e \tag{1.8}$$

The general equation for positron decay from an atom is:

$${}^{A}_{Z}X \rightarrow {}^{A}_{Z-1}Y + {}^{0}_{1}\beta^{+} + \nu + Q(e^{+}) \tag{1.9}$$

where $Q(e^+)$ is kinetic energy of the emitted positron. The atom X is proton-rich and achieves stability by converting a proton to a neutron. The positive charge is carried away with the positron. As the daughter nucleus has an atomic number one less than the parent, one of the orbital electrons must be ejected from the atom to balance charge. This is often achieved by a process known as *internal conversion*, where the nucleus supplies energy to an orbital electron to overcome the binding energy and leave it with residual kinetic energy to leave the atom.

The emitted positron will have an initial energy and the energy spectrum is a continuum of values up to a maximum. After emission from the nucleus, the positron loses kinetic energy by interactions with the surrounding matter. The positron interacts with other nuclei as it is deflected from its original direction by one of four types of interaction:

- *Inelastic collisions* with atomic electrons, which is the predominant mechanism of loss of kinetic energy,
- *Elastic scattering* with atomic electrons, where the positron is deflected but energy and momentum are conserved,
- *Inelastic scattering* with a nucleus, with deflection of the positron and often with the corresponding emission of Bremsstrahlung radiation,
- *Elastic scattering* with a nucleus where the positron is deflected but does not radiate any energy.

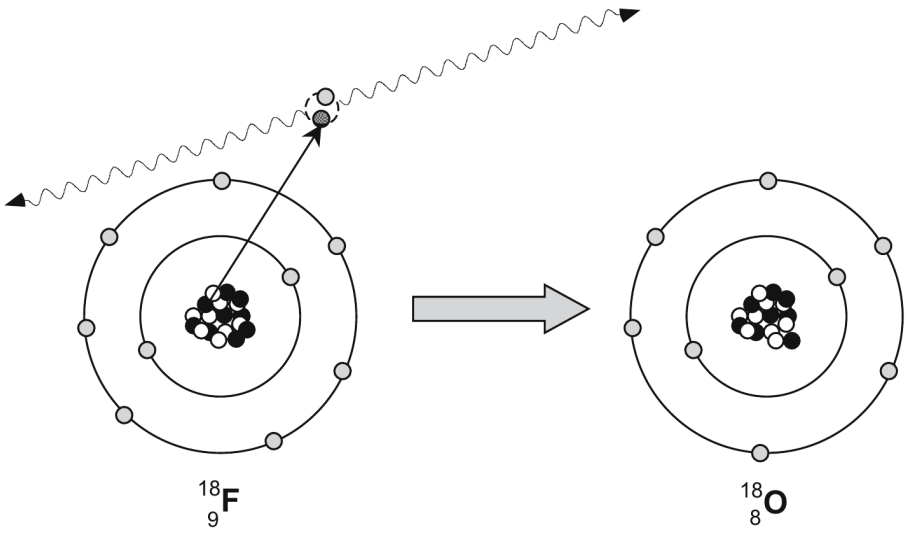

Figure 1.6: Annihilation radiation is produced subsequent to a positron being ejected from the nucleus. The positron travels a finite distance, losing energy by interaction with other electrons and nuclei as it does, until it comes to rest and combines (annihilates) with an electron to give rise to two photons, each equivalent to the restmass energy of the particles. The two photons are approximately anti-collinear and it is this property that is used to localize events in PET.

As the positron passes through matter it loses energy constantly in ionization events with other atoms or by radiation after an inelastic scattering. Both of these situations will induce a deflection in the positron path, and thus the positron takes

an extremely tortuous passage through matter. Due to this, it is difficult to estimate the range of positrons based on their energy alone, and empirical measurements are usually made to determine the mean positron range in a specific material.

The positron eventually combines with an electron when both are essentially at rest. A metastable intermediate species called *positronium* may be formed by the positron and electron combining. *Positronium* is a non-nuclear element composed of the positron and electron. Positronium formation occurs with a high probability in gases and metals, but only in about one-third of cases in water or human tissue where direct annihilation of the electron and the positron is more favorable [25]. Positronium can exist in either of two states, *parapositronium* (spin = +1/2, life-time in vacuum $\tau = 100$ ps) or *orthopositronium* (spin = +3/2, life-time in vacuum $\tau = 125$ ns). Approximately three-quarters of the positronium formed in vacuum is orthopositronium.

Positron emission from the nucleus, with subsequent annihilation, means that the photon-producing event (the annihilation) occurs outside the radioactive nucleus. The finite distance that positrons travel after emission contributes uncertainty to the localization of the decaying nucleus (the nucleus is the species that we wish to determine the location of in positron tomography, not where the positron eventually annihilates). The uncertainty due to positron range is a function that increases with increasing initial energy of the positron. For a high-energy positron such as ^{82}Rb ($E_{max} = 3.4$ MeV), the mean range in water is around 5.9 mm. Table 1.1 shows some commonly used positron emitting nuclides and associated properties. When the positron and electron eventually combine and annihilate electromagnetic radiation is given off. The most probable form that this radiation takes is of two photons of 0.511 MeV (the rest-mass equivalent of each particle) emitted at approximately 180° to each other, however, three photons can be emitted ($< 1\%$ probability). The photons are emitted in opposed directions to conserve momentum, which is close to zero before the annihilation.

Many photon pairs are not emitted strictly at 180°, however, due to non-zero momentum when the positron and electron annihilate. This fraction has been estimated to be as high as 65 % in water. This contributes a further uncertainty to the localization of the nuclear decay event of 0.5° FWHM from strictly 180°, which can degrade resolution by a further 1.5 mm (dependent on the distance between the two coincidence detectors) (see Fig. 1.7). This effect, and the finite distance traveled by the positron before annihilation, places a fundamental lower limit of spatial resolution that can be achieved in positron emission tomography [26].

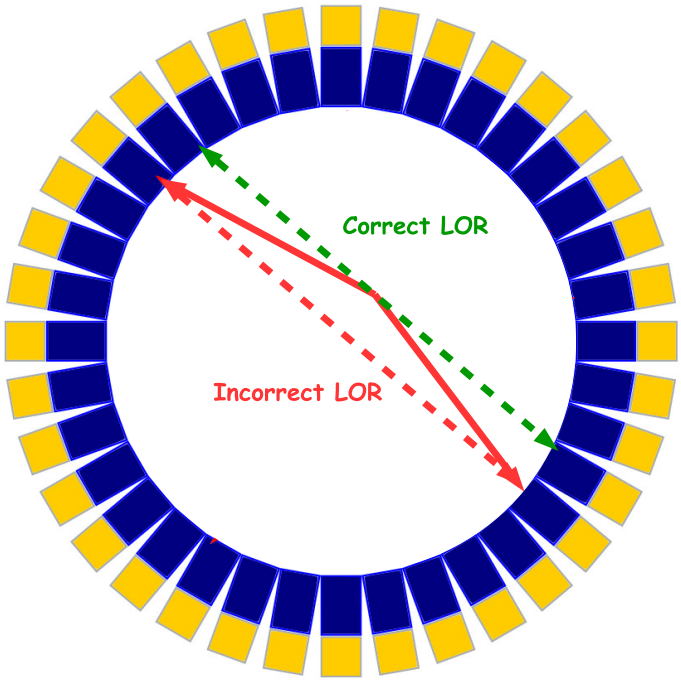

Figure 1.7: Acollinearity introduces a positional error in PET imaging.

1.4.2 Interaction of high energy photons with matter

High-energy photons interact with matter by three main mechanisms, depending on the energy of the electromagnetic radiation. These are the photoelectric effect, the Compton effect, and pair production (the photon must have higher energy than the sum of the rest mass energies of an electron and positron (2×0.511 MeV $=$ 1.022 MeV) for the production to occur). In addition, we have considered the following optical photon processes. For optical photons (250 - 700 nm wavelength) there are other mechanisms such as elastic Rayleigh scattering, absorption and medium boundary interactions. The Geant4 catalog of processes at optical wavelengths includes all of them. The optical properties of the medium which are key to the implementation of these types of processes are stored as entries in a properties table linked to the material in question. They may be expressed as a function of the photon's wavelength.

1.4.2.1 Photoelectric effect

The photoelectric effect is an interaction of photons with orbital electrons in an atom. This is shown in Fig. 1.8 [25]. The photon transfers all of its energy to the electron. Some of the energy is used to overcome the binding energy of the electron, and the remaining energy is transferred to the electron in the form of kinetic energy. The photoelectric effect most probably occurs with an inner shell electron. As the

electron is ejected from the atom (causing ionization of the atom) a more loosely bound outer orbital electron drops down to occupy the vacancy. In doing so it will emit radiation itself due to the differences in the binding energy for the different electron levels. This is a characteristic X-ray. The ejected electron is known as a photoelectron. Alternately, instead of emitting an X-ray, the atom may emit a second electron to remove the energy and this electron is known as an Auger electron. This leaves the atom doubly charged. Characteristic X-rays and Auger electrons are used to identify materials using spectroscopic methods based on the properties of the emitted particles. The photoelectric effect dominates in human tissue at energies less than approximately 100 keV. It is of particular significance for X-ray imaging, and for imaging with low-energy radionuclides. It has little impact at the energy of annihilation radiation (511 keV), but with the development of combined PET/CT systems, where the CT system is used for attenuation correction of the PET data, knowledge of the physics of interaction via the photoelectric effect is extremely important when adjusting the attenuation factors from the X-ray CT to the values appropriate for 511 keV radiation.

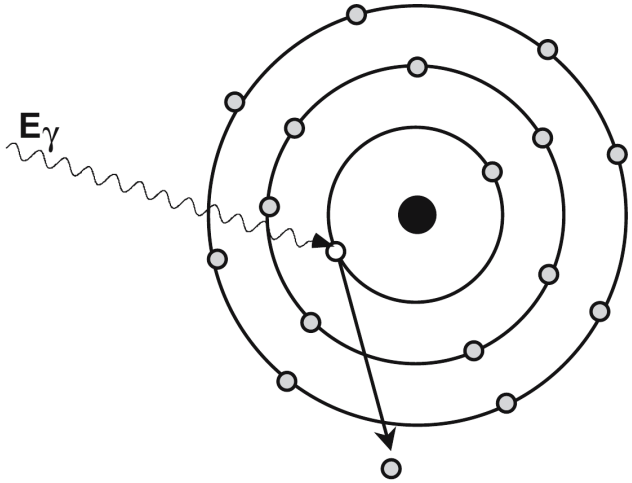

Figure 1.8: The photon is absorbed by photoelectric effect.

1.4.2.2 Compton scattering

Compton scattering is the interaction between a photon and a loosely bound orbital electron. The electron is so loosely connected to the atom that it can be considered to be essentially free. This effect dominates in human tissue at energies above approximately 100 keV and less than ∼2 MeV. The binding potential of the electron to the atom is extremely small compared with the energy of the photon, such that it can be considered to be negligible in the calculation. After the interaction, the photon undergoes a change in direction and the electron is ejected from the atom.

The energy loss by the photon is divided between the small binding energy of the energy level and the kinetic energy imparted to the Compton recoil electron. The energy transferred does not depend on the properties of the material or its electron density (Fig. 1.9). The energy of the photon after the Compton scattering can be calculated from the Compton equation:

$$E'_\gamma = \frac{E_\gamma}{1 + \frac{E_\gamma}{m_0 c^2}(1 - \cos\theta_c)} \tag{1.10}$$

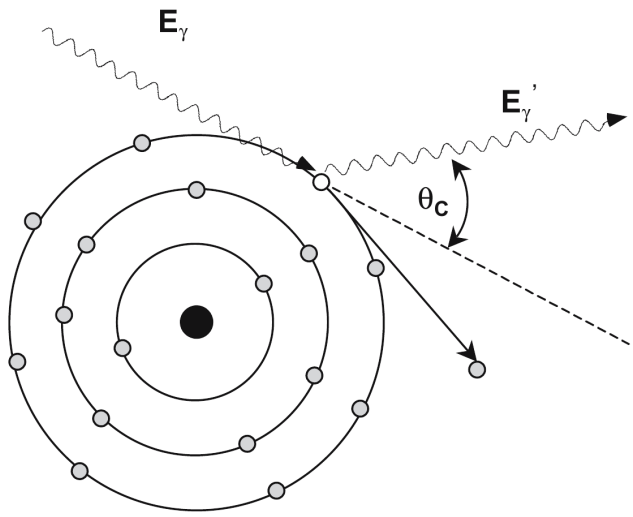

Figure 1.9: In Compton scattering, part of the energy of the incoming photon is transferred to an atomic electron. This electron is known as the recoil electron. The photon is deflected through an angle proportional to the amount of energy lost.

From consideration of the Compton equation it can be seen that the maximum energy loss occurs when the scattering angle is 180° (cos(180°) = - 1), i.e., the photon is back-scattered. A 180° back-scattered annihilation photon will have an energy of 170 keV and emitted electron has an energy of 341 keV, this is the energy of the, so-called, Compton edge. Compton scattering is not equally probable at all energies or scattering angles. The probability of scattering is given by the Klein-Nishina equation [27]:

$$\frac{d\sigma}{d\Omega} = Z r_0^2 \left(\frac{1}{1 + \alpha(1 - \cos\theta_c)}\right)^2 \left(\frac{1 + \cos^2\theta}{2}\right) \left(1 + \frac{\alpha^2(1 - \cos\theta_c)^2}{(1 + \cos^2\theta_c)(1 + \alpha\{1 - \cos\theta_c\})}\right) \tag{1.11}$$

where $d\sigma/d\Omega$ is the differential scattering cross-section, Z is the atomic number of the scattering material, r_0 is the classical electron radius, and $\alpha = E_\gamma/m_0c^2$. For positron annihilation radiation (where $\alpha = 1$) in tissue, this equation can be reduced for first-order scattered events to give the relative probability of scatter as:

$$\frac{d\sigma}{d\Omega} = \left(\frac{1}{2-\cos\theta_c}\right)^2 \left(1 + \frac{(1-\cos\theta_c)^2}{(2-\cos\theta_c)(1+\cos^2\theta_c)}\right) \tag{1.12}$$

The induced shape of the electron energy spectrum, as simulated by the GEANT4 software, will be discussed in the Section 3.2.

1.4.2.3 Pair production

Another mechanism for photons to interact with matter is by pair production. When photons with energy greater than 1.022 MeV (twice the energy equivalent to the rest mass of an electron) pass in the vicinity of a nucleus it is possible that they will spontaneously convert to electron-positron pair. This direct electron pair production in the Coulomb field of a nucleus is the dominant interaction mechanism at high energies (Fig. 1.10). Above the threshold of 1.022 MeV, the probability of pair production increases as energy increases. At 10 MeV, this probability is about 60%. Any energy left over after the production of the electron-positron pair is shared between the particles as kinetic energy and recoil energy nucleus, with the positron having slightly higher kinetic energy than the electron as the interaction of the particles with the nucleus causes an acceleration of the positron and a deceleration of the electron. The process of pair production demonstrates a number of conservation laws.

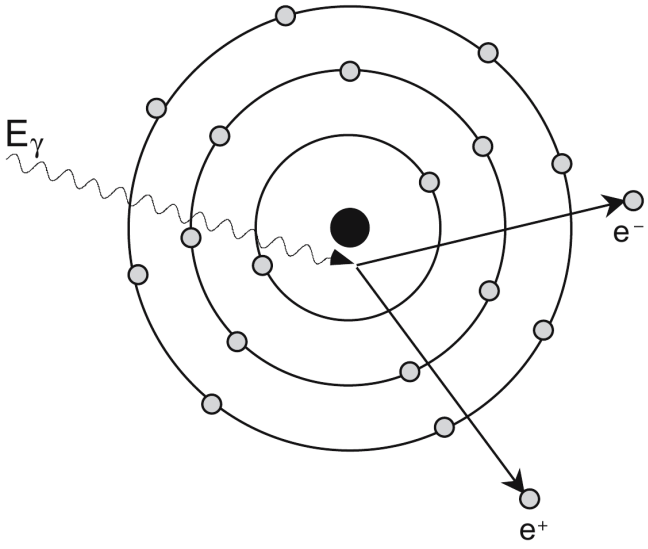

Figure 1.10: The pair production process is illustrated. As a photon passes in the vicinity of a nucleus spontaneous formation of positive and negatively charged electrons can occur. The threshold energy required for this is equal to the sum of the rest masses for the two particles (1.022 MeV).

Since in the PET the photon energy is limited to the 511 keV the pair production is not relevant and could be omitted in the simulation.

1.4.2.4 Attenuation of photons

Calculations of photon interactions are given in terms of atomic cross sections (σ) with units of [cm^2/atom]. An alternative unit, often employed, is to quote the cross section for interaction in [barns/atom], where 1 [barn] = 10^{-24}[cm^2]. The total atomic cross section is given by the sum of process relevant for the photons with energies less than 511 keV:

$$\sigma_{tot} = \sigma_{pe} + \sigma_{incoh} + \sigma_{coh}, \tag{1.13}$$

where the cross sections are for the photoelectric effect (pe), incoherent Compton scattering ($incoh$), coherent (Rayleigh) scattering (coh). Values for attenuation coefficient are often given as mass attenuation coefficients (μ/ρ) with units of [cm^2·g^{-1}]. The reason for this is that this value can be converted into a linear attenuation coefficient (μ_l) for any material simply by multiplying by the density (ρ) of the material:

$$\mu_1[cm^{-1}] = \mu/\rho[\mathrm{cm}^2 \cdot \mathrm{g}^{-1}]\rho[\mathrm{g} \cdot \mathrm{cm}^{-3}]. \tag{1.14}$$

The mass attenuation coefficient is related to the total cross section by:

$$\mu/\rho[\mathrm{cm}^2 \cdot \mathrm{g}^{-1}] = \frac{\sigma_{tot}}{u[\mathrm{g}]A}, \tag{1.15}$$

where $u[\mathrm{g}] = 1.661 \times 10^{-24}[\mathrm{g}]$ is the atomic mass unit ($1/N_A$ where N_A is Avogadro's number) defined as 1/12th of the mass of an atom of ^{12}C, and A is the relative atomic mass of the target element [28].

We have seen that the primary mechanism for photon interaction with matter at energies around 0.5 MeV is by a Compton interaction. The result of this form of interaction is that the primary photon changes direction (i.e., is "scattered") and loses energy. In addition, the atom where the interaction occurred is ionized. For a well-collimated source of photons and detector, attenuation takes the form of a mono-exponential function, i.e.,

$$I_x = I_0 e^{-\mu x} \tag{1.16}$$

where I represents the photon beam intensity, the subscripts "0" and "x" refer respectively to the unattenuated beam intensity and the intensity measured through a thickness of material of thickness x, and μ refers to the attenuation coefficient of the material (units: cm^{-1}). Attenuation is a function of the photon energy and

the electron density (Z number) of the attenuator. The attenuation coefficient is a measure of the probability that a photon will be attenuated by a unit length of the medium. For example, the linear attenuation coefficient for a water is about 0.096 cm^{-1} [12] (see Fig. 1.11).

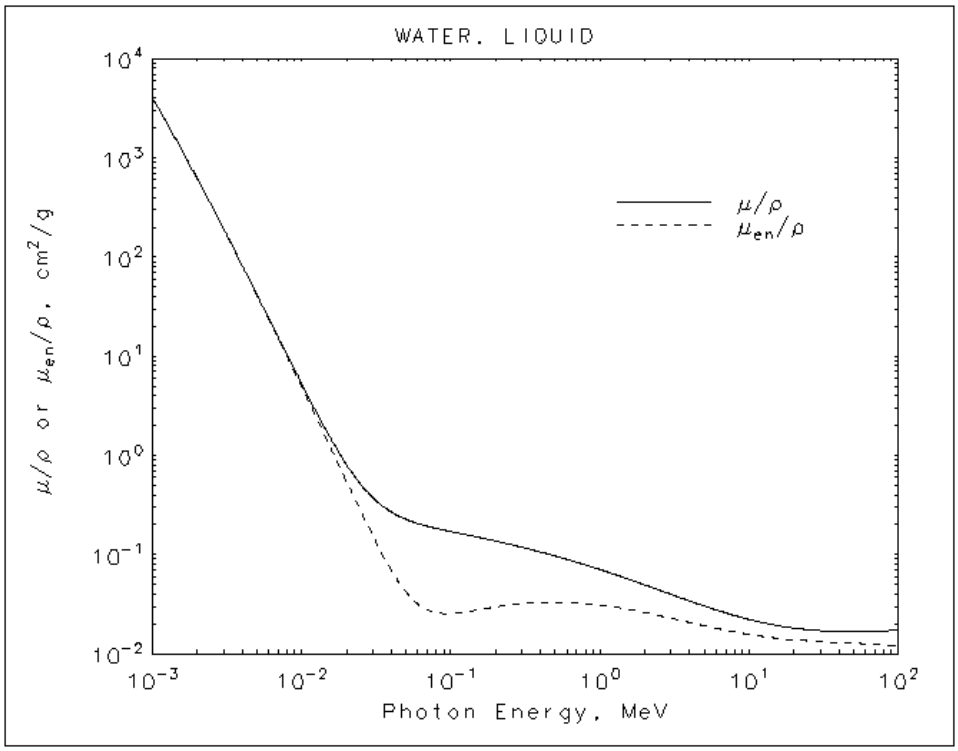

Figure 1.11: Linear attenuation coefficient for a water [12].

Positron emission possesses an important distinction from single-photon measurements in terms of attenuation. Consider the count rate from a single photon emitting point source of radioactivity at a depth, a, in an attenuating medium of total thickness, D (see Fig. 1.12). The count rate C observed by an external detector A would be:

$$C_a = C_0 e^{-\mu a}. \tag{1.17}$$

where C_0 represents the unattenuated count rate from the source, and μ is the attenuation coefficient of the medium (assumed to be a constant here). Clearly the count rate changes with the depth a. If measurements were made of the source from the 180° opposed direction the count rate observed by detector B would be:

$$C_b = C_0 e^{-\mu(D-a)}, \tag{1.18}$$

where the depth b is given by $(D - a)$. The count rate observed by the detectors will be equivalent when $a = b$. Now consider the same case for a positron-emitting

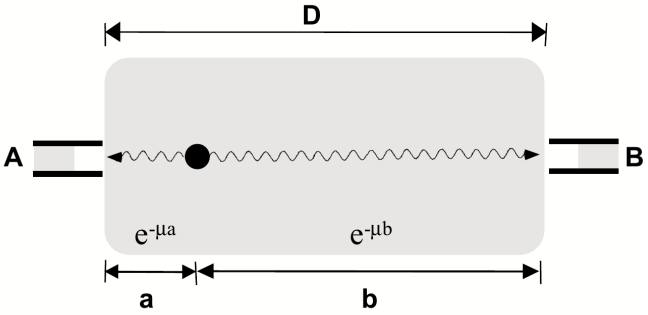

Figure 1.12: Detectors A and B record attenuated count rates arising from the source located a distance a from detector A and b from detector B. For each positron annihilation, the probability of detecting both photons is the product of the individual photon detection probabilities. Therefore, the combined count rate observed is independent of the position of the source emitter along the line of response. The total attenuation id determined by the total thickness (D) alone.

source, where detectors A and B are measuring coincident photons. The count rate is given by the product of the probability of counting both photons and will be:

$$C = (C_0 e^{-\mu a}) \times (C_0 e^{-\mu(D-a)}) = C_0(e^{-\mu a} \times e^{-\mu(D-a)}) = C_0 e^{-\mu(a+(D-a))} = C_0 e^{-\mu D}. \tag{1.19}$$

which shows that the count rate observed in an object only depends on the total thickness of the object, D; i.e., the count rate observed is independent of the position of the source in the object. Therefore, to correct for attenuation of coincidence detection from annihilation radiation one measurement, the total attenuation path length ($-\mu$D), is all that is required.

For example, for a $D = 20$ cm (typical size of phantom used in PET), the flux of the 511 keV photons will be attenuated by a factor of 6.8 in water. As we will see in the Section 2.6.2 the attenuation plays an important role during image reconstruction and need to be taken into account.

1.4.3 Interaction of optical photons with matter

A photon is considered to be optical when its wavelength is much greater than the typical atomic spacing. In GEANT4 optical photons are treated as a class of particle distinct from their higher energy gamma cousins. This implementation allows the wave-like properties of electromagnetic radiation to be incorporated into the optical photon process. Because this theoretical description breaks down at higher energies, there is no smooth transition as a function of energy between the optical photon and gamma particle classes.

1.4.3.1 Rayleigh and Mie scattering

Rayleigh process is defined only for low energy photons because at high energies, the cross-section of the Rayleigh scattering is very small and usually can be neglected. For these process, no energy is transferred to the target, all the electrons of the atom contribute in a coherent way (this process is also called coherent scattering). The direction of the photon is the only modified parameter. Atoms are not excited or ionized. The intensity of the scattered light is proportional to $1/\lambda^4$ [29].

Mie Scattering (or Mie solution) is an analytical solution of Maxwell's equations for scattering of optical photons by spherical particles. It is significant only when the radius of the scattering object is of order of the wave length. The analytical expressions for Mie scattering are very complicated since they are a series sum of Bessel functions. Geant4, thus, GATE follows one common implementation by Henyey-Greenstein approximation [30]:

$$\frac{d\sigma}{d\Omega} = r\frac{d\sigma}{d\Omega}(\sigma_f, g_f) + (1-r)\frac{d\sigma}{d\Omega}(\sigma_b, g_b), \tag{1.20}$$

where $d\Omega = d\cos(\theta)d\theta$, $\theta_b = \pi - \theta_f$ and r is the ratio factor between the forward angle and backward angle.

1.4.3.2 UNIFIED model

Medium boundary interactions in Geant4 and GATE employ the UNIFIED model [31]. It applies to dielectric-dielectric interfaces and tries to provide a realistic simulation, which deals with all aspects of surface finish and reflector coating (see Fig. 1.13). The surface may be assumed as smooth and covered with a metallized coating representing a specular reflector with given reflection coefficient, or painted with a diffuse reflecting material where Lambertian reflection occurs. The surfaces may or may not be in optical contact with another component and most importantly, one may consider a surface to be made up of micro-facets with normal vectors that follow given distributions around the nominal normal for the volume at the impact point. For very rough surfaces, it is possible for the photon to inversely aim at the same surface again after reflection of refraction and so multiple interactions with the boundary are possible within the process itself.

1.4.4 Charged particle interaction with matter

The energetic charged particles such as α particles and β particles, while passing through matter, lose their energy by interacting with the orbital electrons of the atoms in the matter. In these processes, the atoms are ionized in which the electron in the encounter is ejected or the atoms are excited in which the electron is raised to

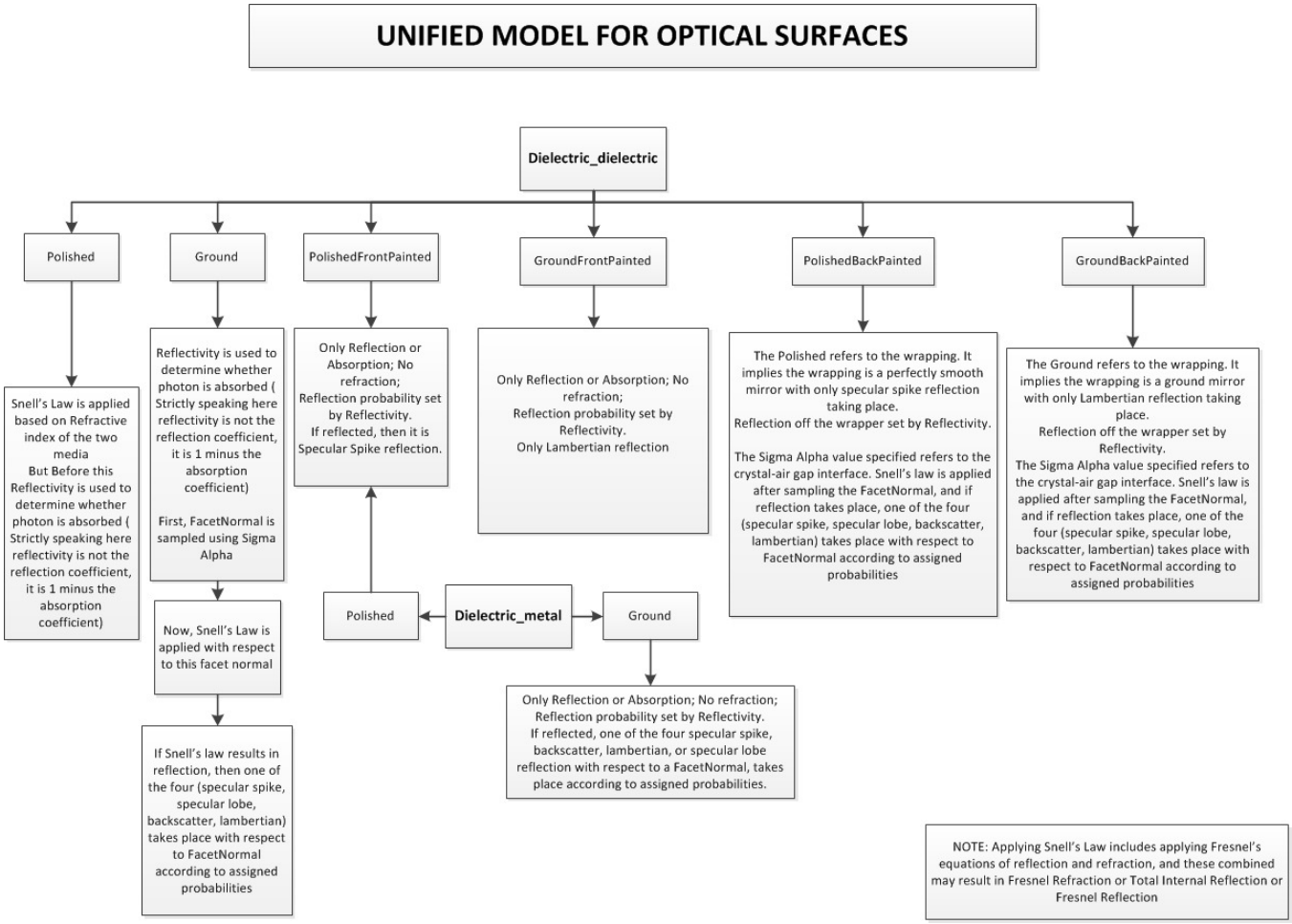

Figure 1.13: The UNIFIED model provides for a range of different reflection mechanisms [30].

a higher energy state. In both excitation and ionization processes, chemical bonds in the molecules of the matter may be ruptured, forming a variety of chemical entities. The range of a charged particle depends on the energy, charge, and mass of the particle as well as the density of the matter it passes through. It increases with increasing of charge and energy.

1.4.4.1 Cherenkov radiation

The phenomenon of the Cherenkov radiation was discovered experimentally by Cherenkov and theoretically by Frank and Tamm in the 1930s in the Union of Soviet Socialist Republics and for this work scientists were awarded the Nobel Prize in 1958.

The famous equation that defines the opening angle θ of the cone for generated Cherenkov photons (see Fig. 1.14) in the medium with refractive index n is [32]:

$$\beta = \frac{1}{\cos\theta \cdot n}, \tag{1.21}$$

where $\beta = v/c$, and v is the velocity of the charged particle, c is the speed of light.

From this equation it is evident that in case $\beta \sim 1$, the threshold value β_{min} below which no radiation can be emitted is inversely proportional to refractive index of the medium:

$$\beta_{min} = \frac{1}{n}. \tag{1.22}$$

Therefore, for our Cherenkov tomograph we consider the lead fluoride crystal, which is one of the best candidate for Cherenkov production with high refractive index of about 1.82 (for more details see Section 3.2).

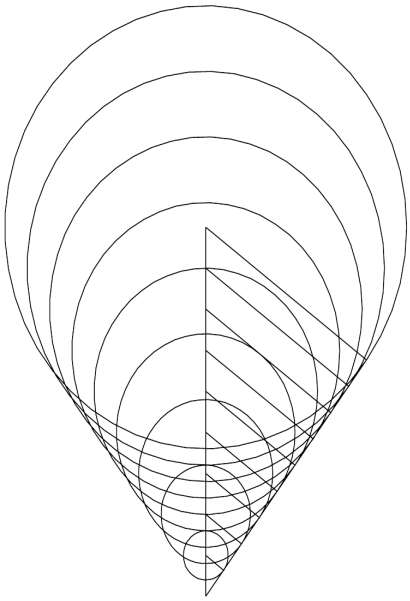

Figure 1.14: The Cherenkov radiation is often described as being analogous to the shock wave emitted in the acoustic range by a projectile or plane moving through air faster than the speed of sound or to the bow wave created by a boat moving across water. Cerenkov photons occur when a charged particle moves through a dispersive medium faster than velocity of the light in that same medium. Cherenkov light is emitted on the surface of a cone with maximum opening angle of $\theta_{max} = \arccos(\frac{1}{n})$. Thus, any charged particle with appropriate speed will produce the Cherenkov radiation. When the particle has slowed below the local speed of light, the radiation ceases and the emission cone has collapsed to zero. The photons produced by this process have an inherent polarization perpendicular to the cone's surface at production.

The number of the emitted optical photons N depends on the photon wavelength

λ as [33]:

$$\frac{\partial^2 N}{\partial x \partial \lambda} = 2\pi\alpha \left(1 - \frac{1}{\beta^2 n^2}\right) 1/\lambda^2, \tag{1.23}$$

where $\alpha = 1/137$ is the fine structure constant. Unlike the fluorescence or emission spectra, the Cherenkov radiation spectrum given by the above formula, is continuous and its density is inversely related to the wavelength squared. Therefore, the number of optical photons increases as the wavelength decreases. That explains why the Cherenkov radiation seems blue and mostly in UV range and at the same time this peculiarity should be take into account when different optical mediums are considering. Significant number of photons can be lost because of the transparency of the materials.

The validity of Cherenkov's observations and of equation 1.21 was strikingly confirmed by Collins and Resling [34]. Cherenkov was the first, who suggested that the radiation might be used for detection of the charged particles. This process is much faster in comparison with scintillation, and with recent developments in electronics and detection becomes more and more interesting for medical physics application.

The GATE allows to simulate Cherenkov process. In this modeling the time and position of Cherenkov photon emission are calculated from quantities known at the beginning of a charged particle's step. The step is assumed to be rectilinear even in the presence of a magnetic field. The step size can be limited by specifying a maximum (average) number of Cherenkov photons created during the step (using the SetMaxNumPhotonsPerStep method). The actual number generated will necessarily be different due to the Poissonian nature of the production. In the present implementation, the production density of photons is distributed evenly along the particle's track segment, even if the particle has slowed significantly during the step. We discuss the simulation result on the number of the produced Cherenkov photons in the detector and the corresponding wavelength spectrum in the Section 3.2.

Chapter 2

Instrumentation in PET

2.1 Main characteristics of the detectors for PET

The physical characteristics of PET tomographs can be specified in terms of parameters such as transverse (in-plane) and axial spatial resolution, sensitivity, count rate capability, scatter fraction and image uniformity. Measurements are made with phantoms such as line sources and 20 cm diameter uniform cylinders according to standards defined by the National Electrical Manufacturers Association (NEMA) [35]. These measurements reflect the performance of the scanner and provide a basis on which to compare different tomographs. However, it is difficult to realistically evaluate overall scanner performance based on comparisons of a single parameter such as spatial resolution or maximum count rate.

2.1.1 Sensitivity

Scanner's sensitivity represents its ability to detect the coincident photons emitted from inside the scanner FOV and defined as number of counts per unit time detected by the device (i.e., [cps/μCi] or [cps/kBq]) [25]. In particular, this characteristic depends on two parameters of the scanner: fraction of the total solid angle covered by it over the imaging field and the stopping efficiency of the detectors for 511 keV photons. Based on the above factors discussed, the sensitivity S of a single ring PET scanner can be expressed as [36]:

$$S = \frac{A \cdot \varepsilon^2 \cdot e^{-\mu d} \cdot 3.7 \times 10^4}{4\pi r^2} [\text{cps}/\mu\text{Ci}], \tag{2.1}$$

where A is detector area seen by a point source to be imaged in the center FOV, ε is detector efficiency, μ is a linear attenuation coefficient of 511 keV photons in the detection material with thickness d, and r is the radius of the ring of the scanner. The proportionality to ε^2 arises from the two detectors with efficiency ε, i.e., $\varepsilon \times \varepsilon$.

Therefore, small-diameter PET scanners (i.e., small-animal PET scanners described in the Section 1.2) have higher sensitivity. Another way to improve sensitivity is to increase the axial FOV (i.e. project EXPLORER for total-body PET scanning with announced axial FOV of 2 m [37]).

The stopping efficiency of the PET detector is related to the type of detector being used. The geometric factor depends on the distance between the source and the detector, the diameter of the ring and the number of detectors per ring. Increasing the distance between the detector and the source reduces the solid angle and thus decreases the geometric efficiency of the scanner and vice versa and in the same time increasing the diameter of the ring decreases the solid angle subtended by the source at the detector, thus, reducing the geometric efficiency and in turn the sensitivity. Also the sensitivity increases with increasing number of rings in the scanner. We study this effect in the Section 4.2 while we increase scanner diameter from 81 cm to 91 cm.

For an extended source at the center of such scanners, the geometric efficiency is approximated as $w/2r$, where w is the axial width of the detector element and r is the radius of the ring. Thus, the sensitivity of the scanner is highest at the center of the axial FOV and gradually decreases toward the periphery.

As it known, for typical PET scanners, there are also multiple rings and each detector is connected in coincidence with as many as half the number of detectors on the opposite side in the same ring as well as with detectors in other rings. Thus, the sensitivity of multi-ring scanners will increase with the number of the detector rings.

In addition, sensitivity of the PET machine increases as the square of the detector efficiency, which depends on the scintillation decay time (for scintillators) and stopping power of the detector.

We estimated the sensitivity of the scanner during image reconstruction and typical distribution is shown in Fig. 2.1.

2.1.2 Energy resolution

Typically, radiation detectors convert the deposited energy into a measurable electrical signal or charge. The integral of this signal is then proportional to the total energy deposited in the detector by the radiation. The ability of the radiation detector to accurately measure the deposited energy is of paramount importance for most of its uses. This accuracy is characterized by the width of the photopeak in the energy spectrum, and is referred to as the energy resolution of the detector.

In PET, the development of the 3D volumetric acquisition and improvements in the detector energy resolution have allowed the implementation of scatter corrections based on the analysis of the photon energy. The scatter correction consist of the

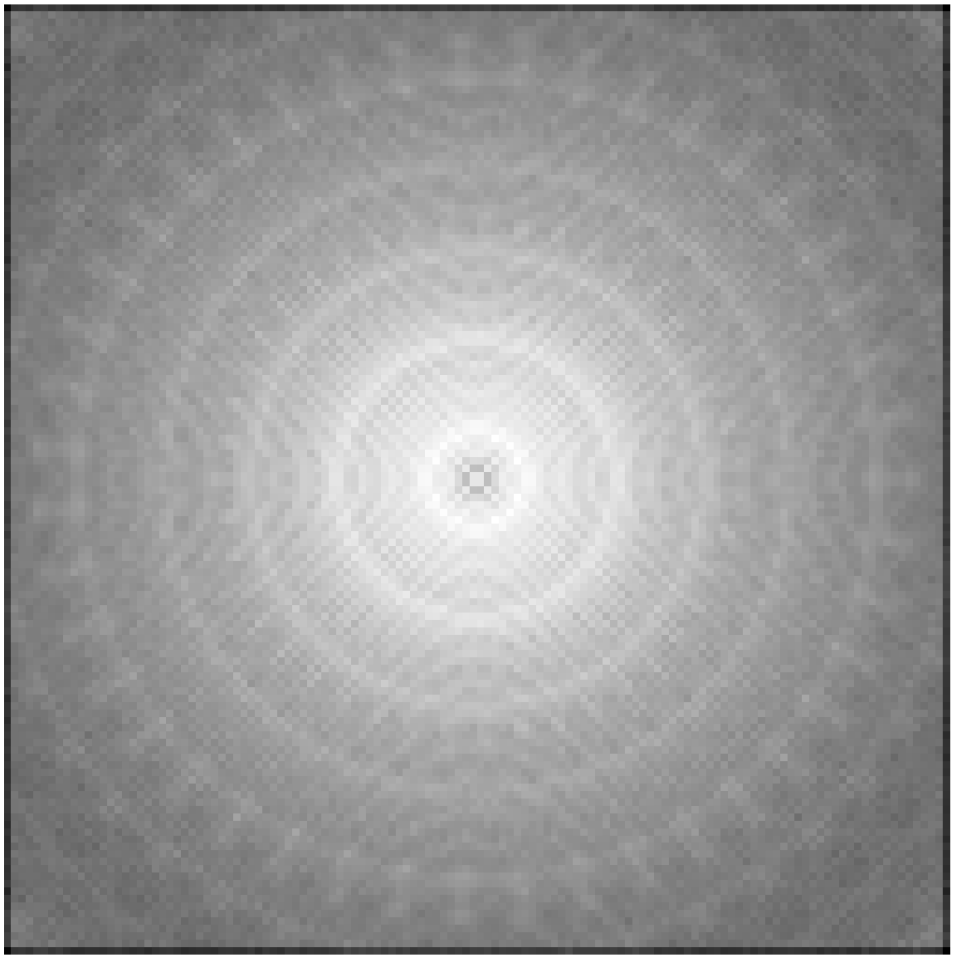

Figure 2.1: Sensitivity of the scanner for image reconstruction calculated using the code CASToR.

subtraction of a fraction of the Compton data from the photopeak data.

The conventional tomographs based on the BGO scintillator crystals have an energy resolution of about 25 %, and are usually operated with an energy threshold in the range 250-350 keV [38]. Many small-angle Compton scatters involve little energy loss and are therefore accepted within the wide energy window of BGO. Another inorganic scintillators such as lutetium oxyorthosilicate (LSO) [39] have improved light output and better energy resolution that may help reduce the scatter fraction. Nevertheless, the energy resolution of LSO will not be as good as that of NaI and even an energy resolution of 10-12 % still results in a scatter fraction in 3D of around 30 %. Decreasing the lower level discriminator (LLD) setting from 380 keV to 150 keV increases unscattered counts (by about 20 %) as well as increasing scattered events. Improved energy resolution from better scintillation materials reaches 8-10 % (FWHM) at 511-keV [26].

Therefore, scatter will be always present and methods dealing with it will be required. The incorporation of non-energy based methods may help in improving of

accuracy of the PET machine.

In the case of the Cherenkov scanner, as it will be explained in the Chapter 3, the number of the detected optical photons is low and does not allow to measure the energy of the incident gamma photon. As will be seen in the Chapter 4, the fraction of Compton coincidences are reasonable, because a Cherenkov detector is "naturally" less sensitive to photons with the energy less than 511 keV. In the same time, it is not possible to use the energy-based method to determine the fraction of the Compton coincidence. To estimate scatter fraction, one needs to develop a MC based estimation, using the detail simulation of the scanner and the measured density map of the subject [40, 41, 42]. Implementation of such correction for the foreseen Cherenkov scanner requires significant efforts and is out of scope of this study.

2.1.3 Spatial resolution

Spatial resolution of the PET scanner represents its ability to distinguish between two points after image reconstruction procedure. The purpose of this measurement is to characterize the widths of the reconstructed image point spread functions (PSF) of the compact radioactive sources. The width of the spread function is measured by its full width at half-maximum amplitude (FWHM) and full width at tenth-maximum amplitude (FWTM) (see Fig. 2.2).

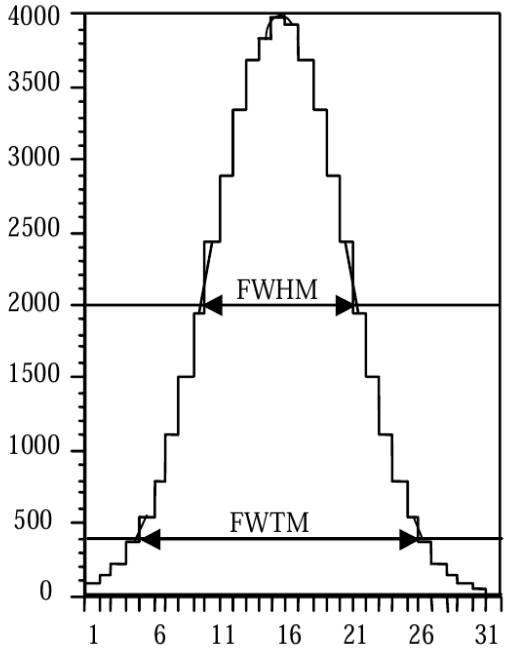

Figure 2.2: A typical response function with FWHM and FWTM determined graphically by interpolation [35].

2.1.4 Timing resolution

The timing resolution of a PET detector describes how precisely could be measured the gamma conversion time in the detector. It has several contribution related to the crystal geometry, electronics performance and characteristic time of the signal generation. The timing resolution of a PET detector is important because it involves the detection of two photons originating from a single coincident event. Since the timing resolution represents the variability in the signal arrival times for different events, it needs to be properly accounted for when detecting coincident events. Fig. 2.3 gives a schematic representation of two detectors set up to measure coincident photons being emitted from a point equidistant from the two detectors.

The coincidence circuitry, however, generates a narrow trigger pulse when the detector signals cross a certain fixed fraction of their individual amplitudes. At time t_1, signal A triggers pulse 1 which also produces a coincidence time window of a predetermined width, 2τ. Signal B, depending upon the timing resolution of the detector, will trigger at a later time, t_2. Depending upon the difference t_2 - t_1, the start of pulse 2 may or may not overlap with the **Coincidence window**. For detectors with poor timing resolution, a large value for 2τ needs to be used in order to detect most of the valid coincidence events [43].

In a PET scanner, the two coincident photons will be emitted from anywhere within the scanner FOV and so the distance traveled by each of them before interaction in the detectors will be different. For a typical whole-body scanner, this distance can be as large as the scanner diameter (about 100 cm). Using the value of speed of light ($c = 3\times 10^8$ m/s), one can calculate an additional maximum timing difference of about 3-4 ns between the two signals (the photons travel 1 m in 3.3 ns). As a result, the coincidence timing window (2τ) of a PET detector needs to be increased even more than the requirements of the timing resolution. The considered Cherenkov detector are design to be very fast. However, the coincidence timing window cannot be reduced to less than 3-4 ns (in a whole-body scanner geometry) due to the difference in arrival times of two photons emitted at the edge of the scanner field of view, as this would restrict the transverse field of view.

For foreseen Cherenkov whole-body TOF-PET scanner with inner diameter of the ring 81 cm we implemented 4.0 ns coincidence window.

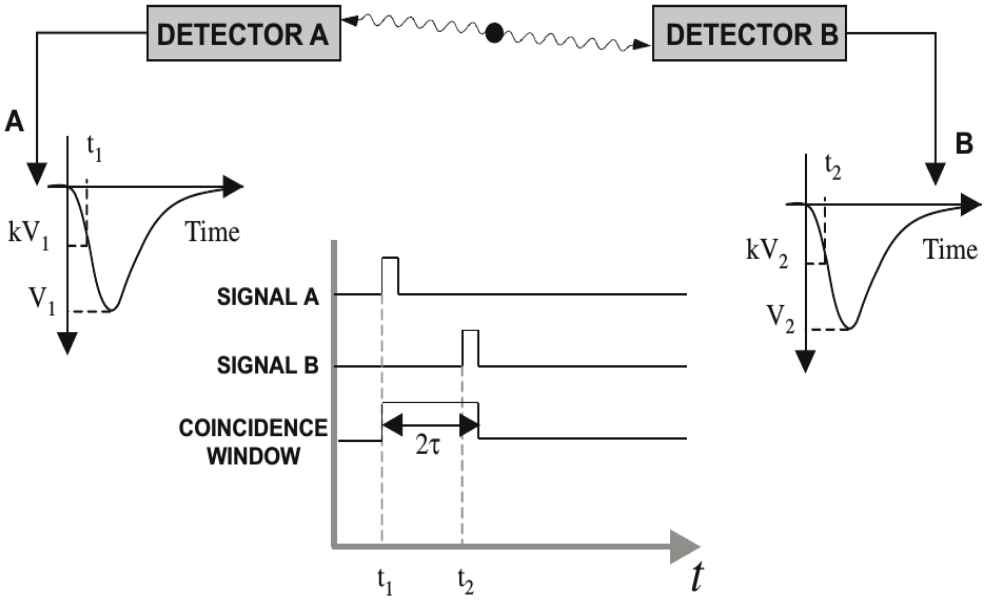

Figure 2.3: Signal A results in a trigger pulse 1. Similarly, signal B results in a trigger pulse 2. A coincidence (AND) circuit then checks for coincidence between the pulse 2 and the coincidence window of width Δt [25].

2.2 Conventional approach: scintillators

Although many scintillation materials have been investigated, only several of them have been commonly used in PET technology [44]. The use of the scintillator detector in PET is based on its properties, such as stopping power of the detector, density, scintillation decay time, light yield and energy resolution at 511 keV, see Tab. 2.1.

Detectors	Effective atomic no Z_{eff}	Density, ρ [g/cm^3]	Scintillation decay time, [ns]	Photon yield [photon/per keV]	Linear attenuation coefficient, μ [cm^{-1}]	re
NaI(Tl)	51	3.67	250	38	0.34	
BGO	75	7.13	300	9	0.96	
BaF_2	54	4.89	0.6	2	0.44	
GSO	59	6.71	50	10	0.67	
LSO	66	7.40	40	29	0.87	
LYSO	65	7.20	50	25	0.87	
$LaBr_3$	49.6	5.3	5 (35)	61	0.47	

Table 2.1: Main properties of the solid scintillators have application in PET [44, 45]

.

The mean distance the photon travels through detector material until complete energy deposition depends on the density and effective atomic number (Z_{eff}) of the detector.

The scintillation decay time arises when a gamma ray interacts with an atom of the detector material, and the atom is excited to a higher energy level, which later decays to the ground state, emitting visible light [46]. The scintillation efficiency of any scintillator is defined as the fraction of all incident particle energy which is converted into visible light.

The scintillation decay time is the time required for scintillation emission to decrease to e^{-1} of its maximum and consist of fast and slow components. In most organic scintillators the decay time is a few nanoseconds, for inorganic materials it is 40 ns and more.

Photon yield or light output is the ability of conversion of ionizing radiation into light energy, and it can be defined as the number of visible photons produced in the bulk of scintillator per energy unit keV. A high-light-output detectors generate well-defined light pulse, and as a result better energy resolution. The intrinsic energy resolution is affected by inhomogeneities in the crystal structure of the detector

and random variations in the production of light in it. The energy resolutions at 511 keV in different detectors vary from 2.9 to 20%, using routine integration time for pulse formation, which runs around a few microseconds. However, in PET imaging, the integration time is a few hundred nanoseconds in order to exclude random coincidences, and the number of photoelectrons collected for a pulse is small, thus degrading the energy resolution. Consequently, the detectors in PET scanners have relatively poorer energy resolution [44].

2.3 Non-conventional approaches

Besides scintillation crystals, another detection materials such as liquids and gases can be apply for non-conventional approach in PET. For example, project of the CaLIPSO group at IRFU is development of the brain-scanning PET device with TOF capability using an innovative liquid TriMethylBismuth (TMBi), the chemical formula is $Bi(CH_3)_3$, as the detection medium [47]. The TMBi's coincidence photoelectric efficiency is twice the value of the LSO/LYSO crystals. Thus, the measured detection efficiency of 85 % for the 511 keV gamma that undergo a photoelectric conversion in TMBi, a promising feature for a potential high resolution PET-scanner.

The proportional chamber works on the principle of detecting the ionization produced by radiation as it passes through a gas chamber. A high electric field is applied within this chamber that results in an acceleration of the ionization electrons produced by the radiation. Subsequently, these highly energetic electrons collide with the neutral gas atoms resulting in secondary ionizations. Hence, a cascade of electrons is eventually collected at the cathode after some energy deposition by the incident radiation. Typically, inert gases such as xenon are used for detecting photons. The cathode normally consists of a single thin wire, but a fine grid of wires can be utilized to measure energy deposition as a function of position within the detector. Such position-sensitive Multi-wire Proportional Chambers (MWPC) have been used in high-energy physics for a long time, and PET scanners have been developed based upon such a detector [48, 49, 50]. However, the disadvantage of these detectors for use in PET is the low density of the gas, leading to a reduced stopping efficiency for 511 keV photons, as well as poor energy resolution.

Several groups work with Cherenkov light detection for PET [51, 52, 15, 53] but still the main limitation factor is low detection efficiency.

2.4 Data Acquisition. Types of coincidences

An event in PET is regarded as valid (or good) if:

1. two photons are detected within a predefined electronic time window known as the coincidence window,

2. the subsequent LOR formed between them is within a valid acceptance angle of the tomograph,

3. the energy deposited in the crystal by both photons is within the selected energy window (for conventional scanners).

The various coincidence events that can be recorded in PET are divided by three categories and shown diagrammatically in Fig. 2.4.

The **prompt** count rate is given by the sum of the true plus random plus scattered event rates.

A **true** coincidence is an event that derives from a single positron-electron annihilation labeled with yellow star on the scheme, Fig. 2.4a. The two annihilation photons both reach detectors on opposing sides of the tomograph without any significant scattering in the subject and are recorded within the coincidence timing window.

Scattered events arise when one or both of the photons from a single positron annihilation detected within the coincidence timing window have undergone a Compton interaction, labelled by blue star in the Fig. 2.4b. Compton scattering causes a loss in energy of the photon and change in direction of the photon. The fraction of scattered events is not a function of count rate, but is constant for a particular object and radioactivity distribution.

A **random (or accidental)** coincidence occurs when two different nuclei decay at approximately the same time. After annihilation of both positrons, four photons are emitted. Two of these photons from different annihilations are counted within the timing window and are considered to have come from the same positron, while the other two are lost, i.e. black arrows in the Fig. 2.4c and Fig. 2.4d.

Multiple events are similar to random events, except that several events from two annihilations are detected within the coincidence timing window. Due to the ambiguity in deciding which pair of events arises from the same annihilation, the event can be disregarded or saved. GATE allows to simulate nine coincidence policies (see Tab. 4.2).

The GATE software propose to chose one of the predefined coincidence policies for the coincidence sorter from the single detection. The following policies are available [54]:

- takeAllGoods: all possible pairs of the "good" singles inside a specified time window and for each pair register a coincidence are considered;

- takeWinnerOfGoods: only the good pair with the highest energy is considered;

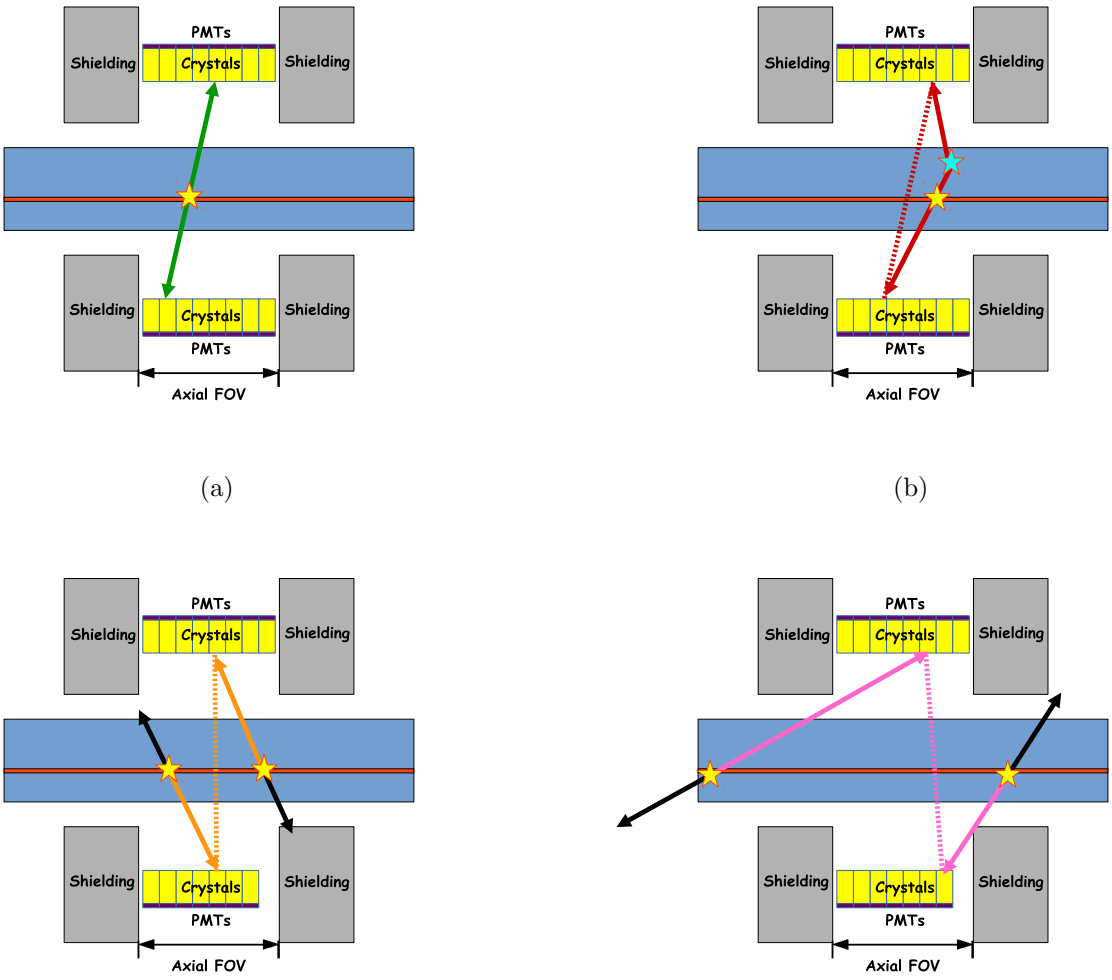

Figure 2.4: The yellow star indicates a positron annihilation vertex. The green arrow is a true coincidence (a), only one useful signal for PET imaging. A scatter event (b) is another type of possible coincidences, where one or both of photons undergo a Compton interaction (a vertex of the Compton scattering is indicated by blue star). A random coincidence (c) corresponds two independent annihilations but only two photons from four are detected within coincidence window, partially this effect can be reduced by adding shielding around the scanner, thus, the number of random coincidences from out axial field-of-view (FOV) will be decreased (d). In case of scattered events and random events, mis-assigned lines of response are indicated by dashed lines. Non-detected photons are shown by black arrows.

- takeWinnerIfIsGood: if the pair with the highest energy is good, take it, otherwise, kill the event;

- takeWinnerIfAllAreGoods: if all pairs are goods, take the one with the highest energy;
- keepIfOnlyOneGood: if exactly one pair is good, keep all the multi-coincidence;
- keepIfAnyIsGood: if at least one pair is good, keep all the multi-coincidence
- keepIfAllAreGoods: if all pairs are goods, keep all the multi-coincidence;
- killAllIfMultipleGoods: If more than one pairs is good, the event is seen as a real "multiple" and thus, all events are killed;
- killAll: no multiple coincidences are accepted, no matter how many good pairs are presented.

"Good" means that a pair of singles are in coincidence and that the 2 singles are separated by a number of blocks greater than or equal to the minSectorDifference parameter of the coincidence sorter.

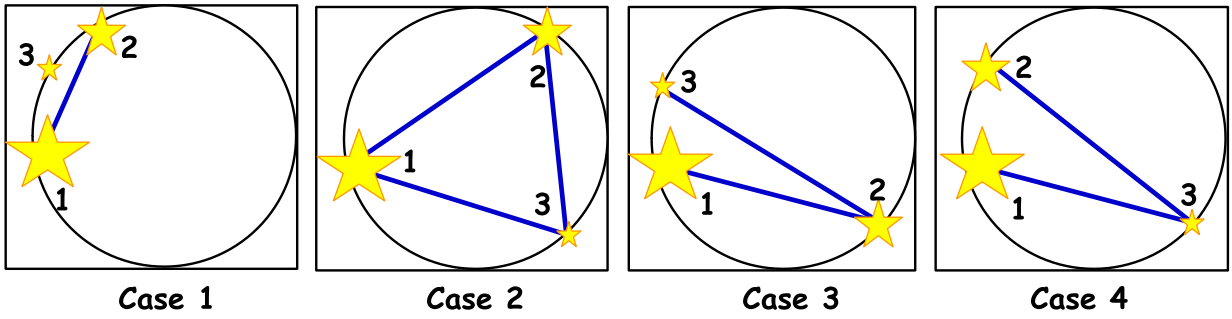

Figure 2.5: Comparison of the behavior of the available multiple processing policies, for various multiple coincidences. The size of the star, as well as the number next to it, indicates the energy level of the single event, i.e. event # 1 has more energy than single # 2. Image reproduced from [54]

2.5 Image reconstruction algorithms in PET

Tomographic image reconstruction techniques are commonly used to obtain 3D images according to distribution of the radiotracer in a phantom or patient's body. These images are obtained from sets of projection data that are recorded at different angles around the object. The quality of the image and the accuracy of the resulting data strongly depend on the reconstruction method. Although analytical reconstruction methods (such as, for example, filtered back projection) are fast, they do not allow the reconstruction technique to model the SPECT or PET imaging

processes. This can be done when iterative methods are used, where an accurate reconstruction may include realistic modeling of the patient, the data acquisition process, and the statistical nature of radioactive decay and photon interactions.

2.5.1 Analytical

Historically, for first image reconstructions was applied analytical approach. It is fast and simple in usage and is much less demanding than more complicated iterative algorithms. However, there are many problems associated with its use. Because the method does not account for the statistical noise in the data and the high-frequency noise is enhanced by the ramp filter, smoothing filter must be included in the reconstruction, which, in turn, degrades image spatial resolution.

For example, filtered back projection (FBP) is an analytical technique that is still the most commonly used method for image reconstruction in the clinical environment. It employs a very simple model of the imaging process which assumes that the number of photons recorded in any given detector bin represents the sum of contributions from the activity located along a line perpendicular to the detector surface. Back-projection procedure redistributes all these photons (counts) back along a line drawn through the images space. The points of intersection for the back-projected lines are assumed to correspond to potential source locations. The projection and back-projection processes are shown schematically in Fig. 2.6. The back-projection process results in a well-known star artifact around every source location unless the projections are convolved with a sinc filter (ramp filter in Fourier domain) prior to back projection. FBP uses a simplistic model of the imaging process which does not allow for incorporation of any realistic data compensation techniques; therefore its images lack quantitative accuracy and often contain significant artifacts [55].

2.5.2 Iterative

Iterative reconstruction algorithms are more popular nowadays because of their better image quality they could propose compared to traditional analytical methods. A scheme in Fig. 2.7 represents the basic principle of this method.

At the first step we have to provide the scanning of the object and saving data. Then we start with uniform image of activity distribution, see Iteration # 1 in the Fig. 2.8. Data are forward projected according to the scanner geometry, the resulting projections are compared to the measured projections and the error-projection is used for correcting the estimate. The new estimate is then forward projected and the comparison between estimated and measured projections yields the next correction. This loop is iterated until estimated and measured projections agree within their statistics, see Iteration # 2–10 in the Fig. 2.8.

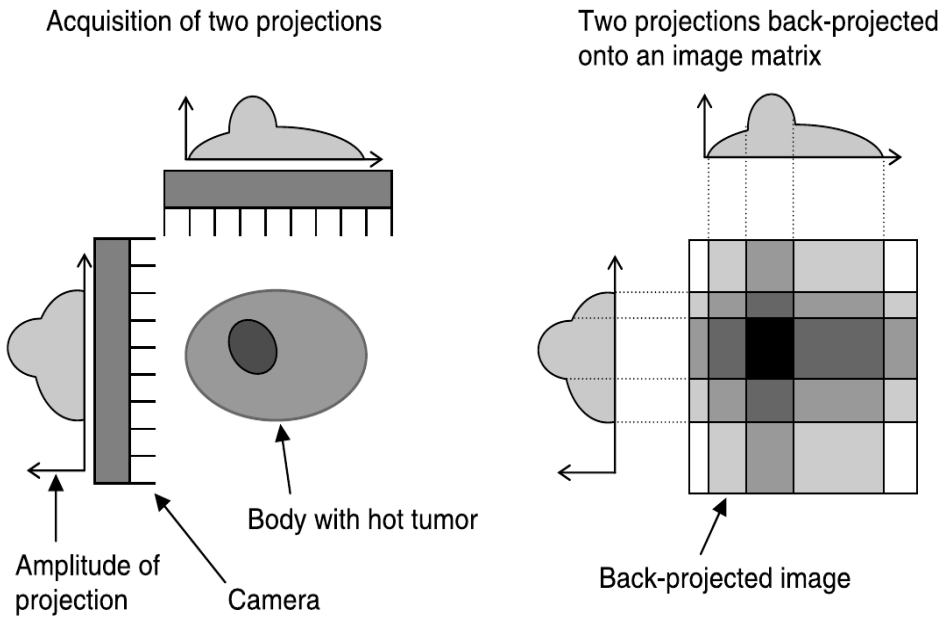

Figure 2.6: Schematic view of analytical algorithm for image reconstruction in PET [55].

Improved availability of computing power and the introduction of fast algorithms have introduced these methods in routine use. Spatial resolution which can be achieved in a PET image is principally limited by positron range and gamma ray non-collinearity. In addition, the width of the detection elements in the tomograph determines the width of the coincidence response function and thus the image resolution.

2.5.3 CASToR platform for image reconstruction

For this study we use the CASToR reconstruction open-source platform for the tomographic 3D iterative reconstruction with TOF capability [56, 57]. This platform includes several optimization algorithms, such as MLEM [58], OSEM, NEGML [59], AML (AB-EMML) [60] and Lanwdeber [61].

For image reconstruction we use MLEM (Maximum Likelihood Expectation Maximization) optimization of list-mode data with continuous TOF information.

$$y_i(t_l) = \sum_j A_{ij}(t_l)\lambda_j + r_i(t_l) + s_i(t_l), \tag{2.2}$$

where $y_i(t_l)$ is a number of counts detected in LOR i with TOF measurement, $\Delta t = t_1 - t_2$ converted into delta length l along the LOR (shift from the LOR center);

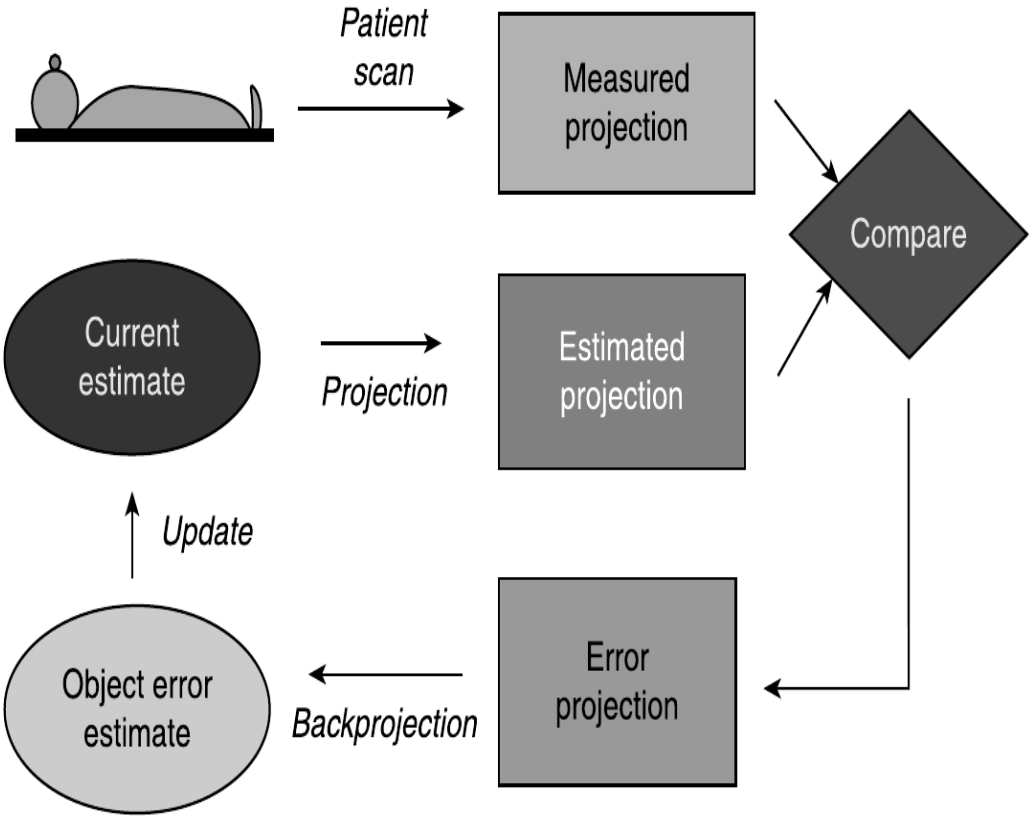

Figure 2.7: Schematic view of iterative algorithm for image reconstruction in PET [55].

A_{ij} is an element of the system matrix for voxel j and LOR i; λ is unknown activity to be reconstructed; r_i and s_i is the number of random and scattered counts for each LOR i.

$$\int_{t_{l_{min}}}^{t_{l_{max}}} y_i(t_l)dt_l = y_i \tag{2.3}$$

$$A_{ij}(t_l) = \int_{l_{vox}} Gaussian_{\sigma,t_l}(l)dl \tag{2.4}$$

An important moment is we can use the OSEM (Ordered Subset Expectation Maximization).

2.6 Corrections

For obtaining a high quality final reconstructed emission images we have to apply several data corrections: normalization, correction for the attenuation, random and scatter events.

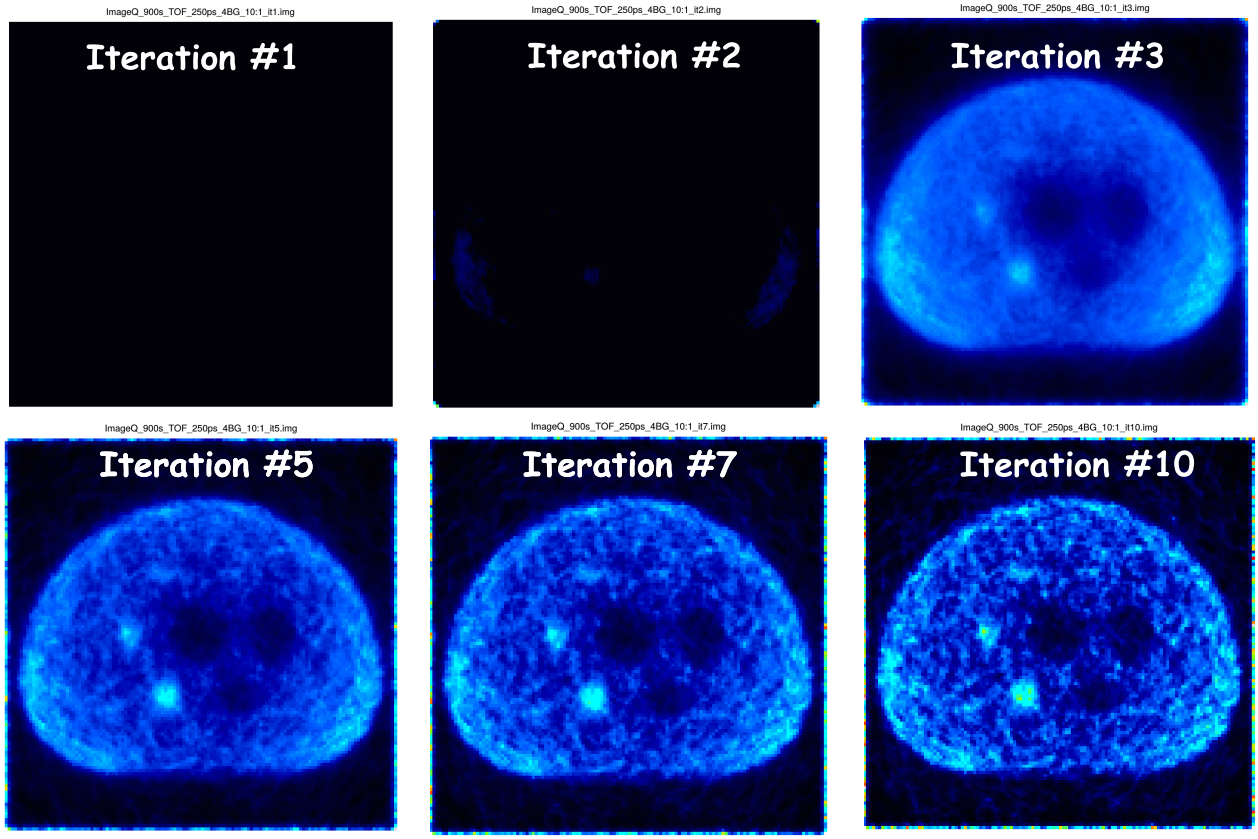

Figure 2.8: Evolution of the image with iterations.

2.6.1 Normalization

Nowadays typical PET scanner consists of thousands of detection crystals arranged in blocks and attached to several hundred PMTs. Because of the variations in the gain of PM tubes, location of the detector in the block, and the physical variation of the detector, the detection efficiency of a detector pair varies from pair to pair, resulting in non-uniformity of the raw data. The method of correction for this effect is called the normalization [44].

Normalization of the acquired data is accomplished by exposing uniformly all detector pairs to a 511 keV photon source, without a subject in the FOV. Data are collected for all detector pairs in both 2D and 3D modes, and normalization factors are calculated for each pair by dividing the average of counts of all detector pairs (LORs) by the individual detector pair count A problem with this method is the long hours ($\sim$ 6 hours) of counting required for meaningful statistical accuracy of the counts, and hence overnight counting is carried out. These normalization factors are

generated weekly or monthly. Most vendors offer software for routine determination of normalization factors for PET scanners.

Normalization factors are calculated as a result of intrinsic crystal efficiencies and geometric factors that account for the variation in crystal efficiency with the position of the crystal in the block and photon incidence angle. Intrinsic efficiencies of individual detectors are determined from the average sum of the coincidence efficiencies between a given detector and all opposite detectors connected in coincidence.

In the case of simulation, the situation is more simple, because, all detectors modules are similar. One can either simulate the normalization data acquisition run and use it to calculate the sensitivity image, or, calculate the sensitivity image directly, from the geometrical position of the detector modules. The latter is the method used in this study. It has an advantage to be fast, but, potentially, it is not take into account the second order effects, related to the detection efficiency variation, because of the different module position.

2.6.2 Attenuation correction

The 511-keV annihilation photons originating from different locations in the body or phantom are attenuated by the media, as they traverse different thicknesses to reach the detector pair in coincidence. This process was described in the Section 1.4.2.4.

To measure the attenuation correction maps one can use either the transmission scan in PET or CT, MRI scan in the case of the multimodal system [62].

In this study, we calculate analytically the attenuation coefficients for the image quality phantom (see Section 4.4) using the linear attenuation coefficient of water. The X-Y Distribution of gamma-emission points in the Body Phantom for all detected coincidences is shown in the Fig. 2.9. The reconstructed images of this phantom are presented in the Fig. 2.10. As we can see, the qual TOF and attenuation correction procedure. For more details see Section 4.4.

2.6.3 Scatter correction

The scatter corrections are discussed in the Section 2.1.2.

2.6.4 Random correction

Random coincidences are a direct consequence of having a large coincidence timing window. They arise when two unrelated photons enter the opposing detectors and are temporally close enough to be recorded within the coincidence timing window. For such events, the system produces a false coincident event. Due to the random

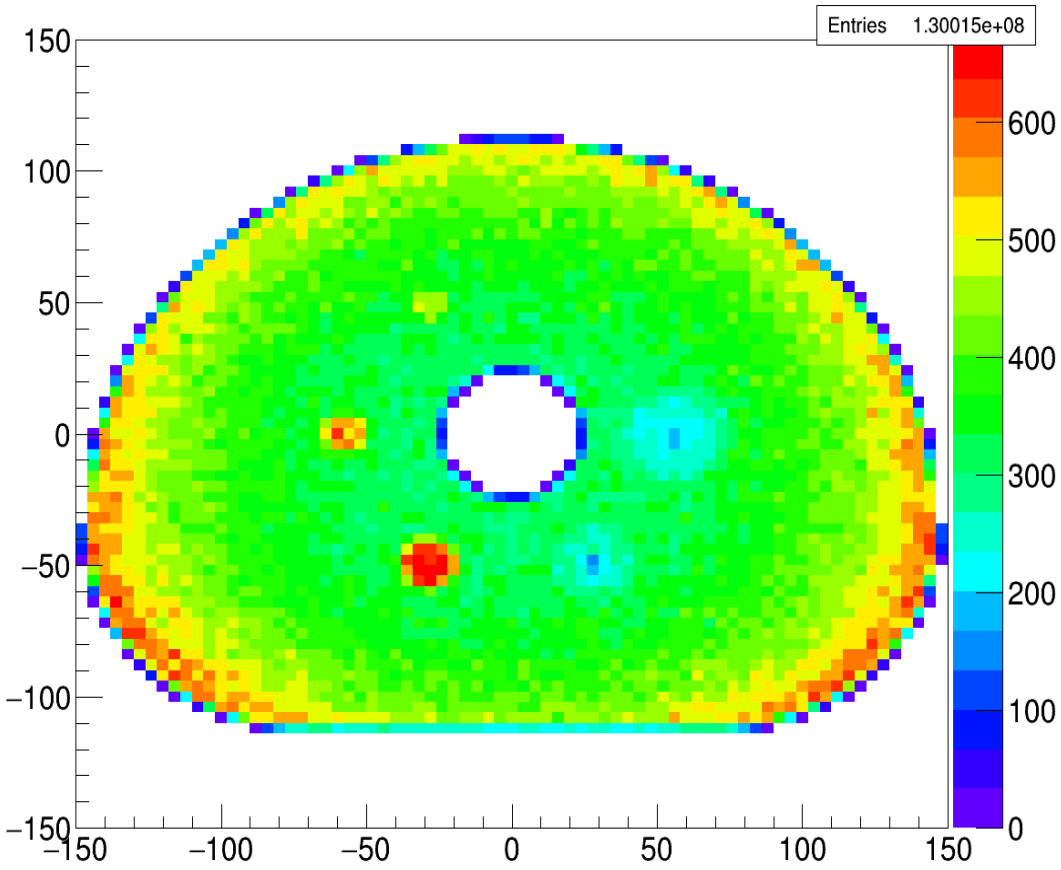

Figure 2.9: Transaxial view of the gamma-emission points in image quality phantom simulation (see Section 4.4) for all detected coincidences.

nature of such events, they are labelled as random or accidental coincidences. Random coincidences add uncorrelated background counts to an acquired PET image and hence decrease image contrast if no corrections are applied to the acquired data.

A standard method of the random correction is to employ two coincidence circuits - one with the standard time window and another with a delayed time window of the same energy window. The counts in the standard time window include both the randoms plus trues, whereas the delayed time window contains only the randoms. For a given source, the random events in both time windows are the same within statistical variations. Delayed window counts are subtracted from the standard window counts to obtain the true coincidence counts, which are essentially free of any systematic errors associated with the PET scanner because they cancel by subtraction [44].

2.7 Main directions of improvement in PET

New developments in the area of PET detectors are aimed at improving spatial resolution, timing resolution and sensitivity. Use of the fastest and luminous scintillators (for example $LaBr_3$), combination with silicon photomultipliers (SiPM) or with avalanche photodiode arrays (APDs), reconstruction of the depth-of-interaction (DOI) in the crystal etc lead to better PET image quality.

2.7.1 Reconstruction DOI

A high stopping power for the crystal is also desirable for the reduction of parallax error in the acquired images (see Fig. 2.11). After a photon enters a detector, it travels a short distance (determined by the mean attenuation length of the crystal) before depositing all its energy. Typically, PET detectors do not measure this point, known as the depth of interaction (DOI) within the crystal. As a result, the measured position of energy deposition is projected to the entrance surface of the detector. For photons that enter the detector at oblique angles, this projected position can produce significant deviations from the real position, leading to a blurring of the reconstructed image. Typically, annihilation points located at large radial distances from the scanner's central axis suffer from this parallax blurring. A thin crystal with high stopping power will help reduce the distance traveled by the photon in the detector and so reduce parallax effects. However, a thin crystal reduces the scanner sensitivity. Thus, to separate this inter-dependence of sensitivity and parallax error, an accurate measurement of the photon depth-of-interaction within the crystal is required [43].

Development of PET detectors with DOI measurement capabilities is one of the an ongoing research interest.

2.7.2 Transition from 2D-PET to 3D-PET imaging

The overall sensitivity of the PET scanners in 2D acquisition is 2-3 % at best [44]. To increase the sensitivity of a scanner, the 3D acquisition has been introduced in which the septa are retracted or they are not present in the scanner (see Fig. 2.12). This mode includes all coincidence events from all detector pairs, thus increasing the sensitivity by a factor of almost 4-8 over 2D acquisitions. If there are n rings in the PET scanner, all ring combinations are accepted and so n^2 sinograms are obtained. However, scattered and random coincidences are increasingly added to the 3D data, thus degrading the spatial resolution as well as requiring more computer memory. As a trade-off, one can limit the angle of acceptance to cut off the random and scattered radiations at the cost of sensitivity. This can be achieved by connecting

in coincidence each detector to a fewer number of opposite detectors than N/2 detectors. The sensitivity in 3D mode is highest at the axial center of the field of view and gradually falls off toward the periphery. Three-dimensional data require more storage as they are approximately 10^3 times more than 2D data and so result in time-consuming computation. However, current fast computers have significantly overcome this problem.

The total-body approach extends the idea of a 3D scanner to the maximum and propose to extend the Z-dimention of the scanner and to cover the human body completely. In particular, the Explorer projects [63] recently finish a construction of the 2m long scanner with goal to achieve a 40-fold reduction in the patient dose required to make a PET image.

2.7.3 Use of combined modalities: PET/CT, PET/MRI

The fusion of functional data gathered from PET system with anatomic information obtained using computed tomography (CT) has led to rapid growth in the use of PET/CT since its implementation in medical routine (see Fig. 2.13). PET/CT is widely available medical imaging technique with established imaging protocols and evidence proven indications. The disadvantages of this method include the limited soft tissue contrast and additional absorbed dose for a patient from CT scanning. Combination of PET and MRI increases the inherent advantages of MRI, such as increased soft tissue contrast, better motion correction and lack of additional ionizing radiation exposure (see Fig. 2.14). The first integrated whole body PET/MRI systems were installed in 2010. PET/MRI systems are more costly than PET/CT systems due to the inherent costs of MRI versus CT technology. PET/CT systems are currently much more widely available than PET/MRI systems, although this may change with time as adoption increase. MRI cannot directly assess tissue density and in particular has difficulty imaging the lung and bones. Therefore, creating an accurate attenuation correction map and standardize protocols for detailed quantification of the radiotracer uptake in the setting of PET/MRI, similar to what has been performed in PET/CT, is necessary [64]. PET/CT systems are also much quieter than a PET/MRI. It creates supplementary comfort for a patient.

In publication [65] performance studies use the time of flight for PET/MRI detector technology were considered.

2.7.4 TOF PET

One of the possible ways to improve the image quality in PET is to apply the TOF technique. The principle of the TOF is based on the time difference measurement between two arriving annihilation photons at the detectors and illustrated in Fig. 2.15.

The first developments of the PET prototypes with TOF potential were proposed during the 1980s-1990s [4, 5, 6, 7, 8, 9, 10]. Theoretically, if it would be possible to collect the precise TOF information for each LOR, the image reconstruction would not needed at all. PET image could be created by adding events into an image matrix with perfect location of each annihilation event based only on TOF information and crystal identification. Unfortunately, this is not the case. In PET line pair data at many angles and create tomographic images through traditional filtered back-projection or through an iterative series of back- and forward-projection steps.

The main idea consist of: 1) suppose two corresponding detectors are equidistant; 2) x is the distance from the center FOV to each detector and a positron is annihilated in the patient at position labelled by ★ at a distance Δx from the center FOV; 3) one of the 511-keV photons will travel distance $x + \Delta x$ and the opposite photon will surmount $x - \Delta x$ respectively; 4) this photons have speed of light c, thus, the difference in arriving time for this pair of photons at the detectors is $\Delta t = 2 \cdot \Delta x/c$; and 5) the photons from the center FOV arrive at the detectors contemporaneously inasmuch as $\Delta x = 0$ [44].

The benefit of applying TOF technique can be defined by [66]:

$$G = \frac{S/N_{TOF}}{S/N_{noTOF}} \sim \sqrt{\frac{D}{\Delta x}} \sim \sqrt{\frac{2D}{c\Delta t}}, \tag{2.5}$$

where G is the gain of the reconstructed PET image, S/N is the signal-to-noise ratio for tomographs with time-of-flight potential (TOF) and conventional ($noTOF$) scanners respectively, D is the radial dimension of the object to be imaged, Δx is spatial uncertainty, associated with the time resolution of the scanner. Therefore, the TOF capability provides information about the localization of the annihilation vertex within the LOR and improves the signal-to-noise ratio.

For example, in case scanning the object with diameter is $D = 20$ cm, using tomograph with coincidence resolving time CRT about 180 ps, the gain increases by a factor of 2.7 and it leads to 8-times lower dose.

The recent developments in time-of-flight in PET were presented in work Vandenberghe et al [67].

In 2017, Lecoq in his work [68] shown that the possibility to reach 10 ps, although extremely challenging, is not limited by physical barriers and that a number of disruptive technologies are presently being investigated at the level of all the components of the detection chain to gain at least a factor of 10 as compared to the present state-of-the-art.

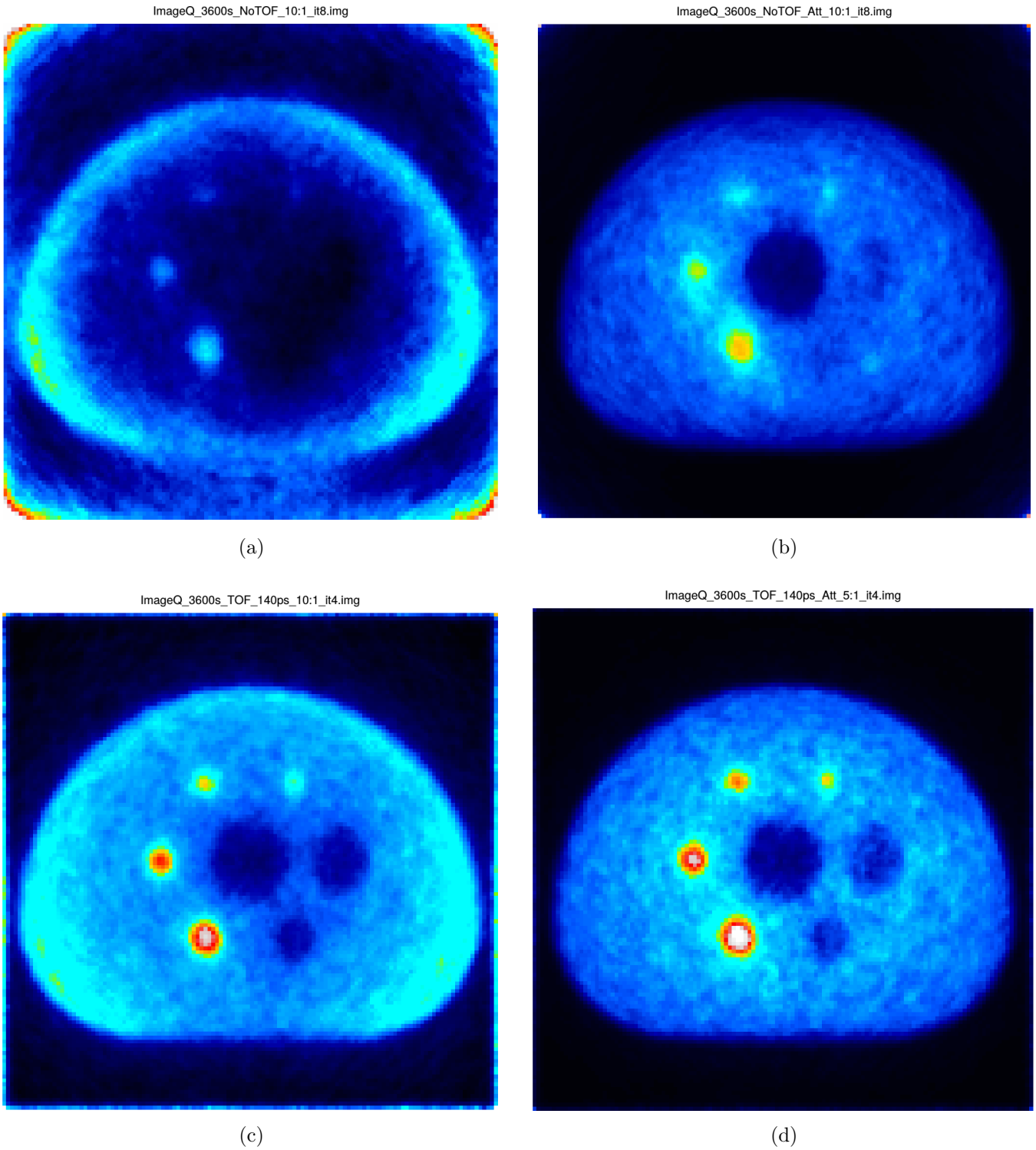

Figure 2.10: Reconstructed images of the Body Phantom NEMA, time of the scanning is 1 hour, 10 iterations with 1 subset. In case (a) reconstructed image without TOF and any attenuation correction; (b) without TOF but after attenuation correction; (c) resolving time TOF 140 ps without attenuation correction; (d) resolving time TOF 140 ps after attenuation correction.

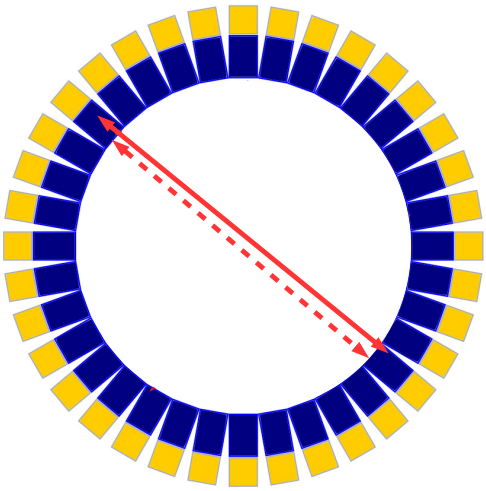

Figure 2.11: The information with DOI of the photons in the crystal decreases the parallax error of the localization of annihilation vertex. The continuous line is the flight path of the photons and dashed line is an assigned LOR.

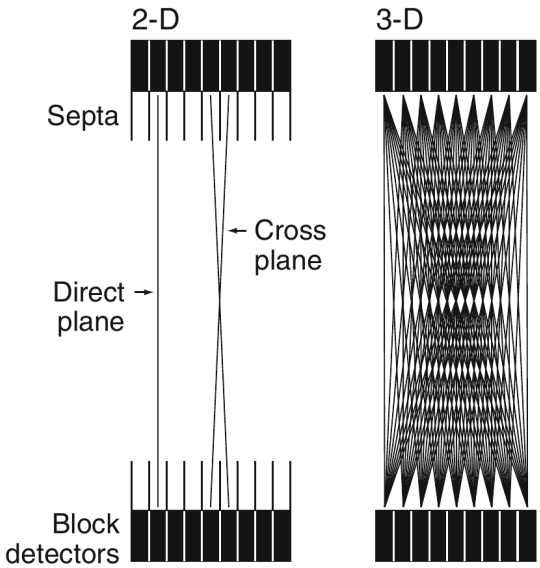

Figure 2.12: Comparison of 2D and 3D PET systems.

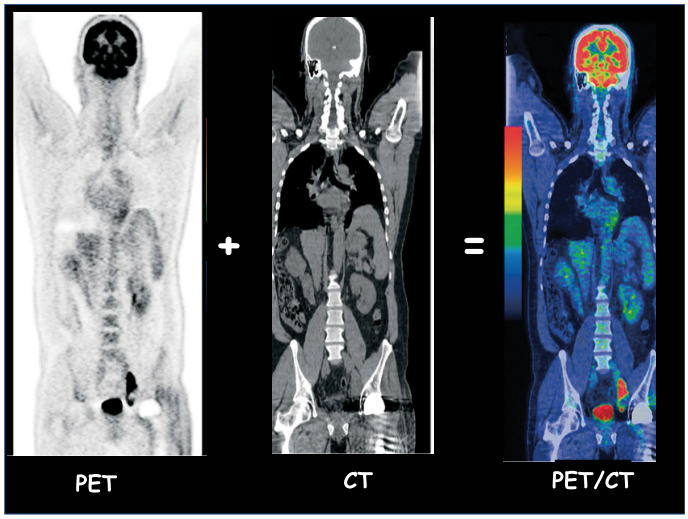

Figure 2.13: PET/CT.

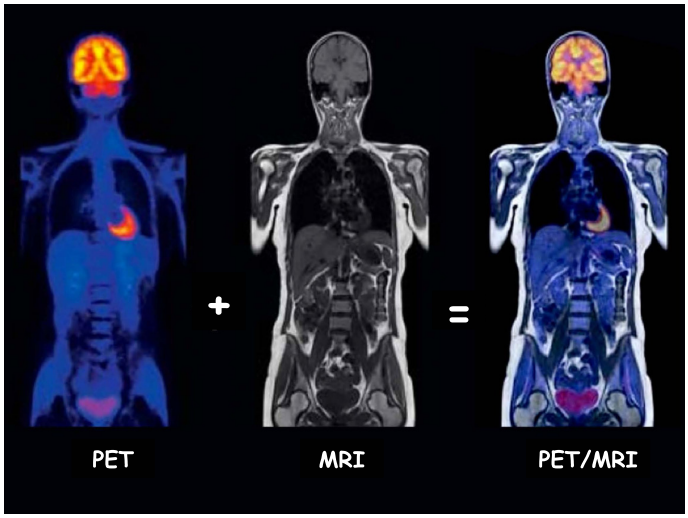

Figure 2.14: PET/MRI.

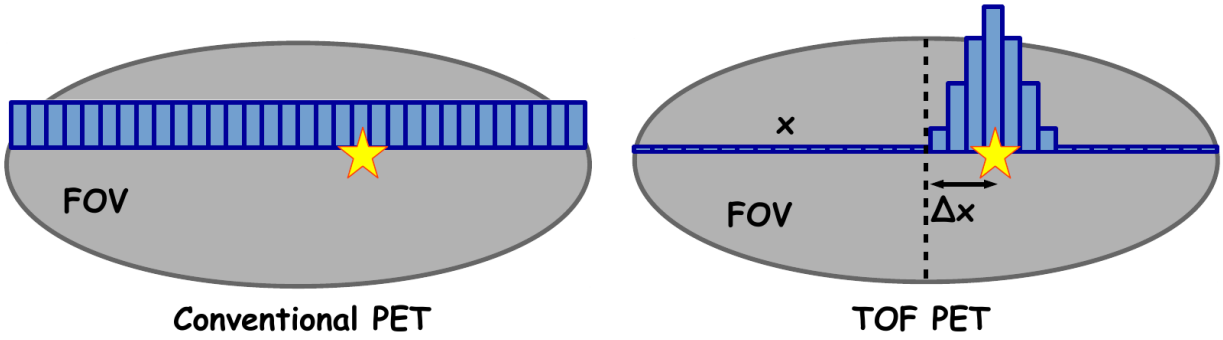

Figure 2.15: Comparison conventional PET technology to time-of-flight PET technology, which allows better localization (with a certain probability) of the point of annihilation on the line of response.

Chapter 3

Modeling

3.1 GATE simulation software

For the following simulation we are using GATE software. GATE (Geant4 application for emission tomography, transmission tomography, radiotherapy and optical imaging) is a Monte Carlo simulation platform developed by the OpenGATE collaboration, thus, it is a community-driven initiative, where every user can access the source code and propose new features [69, 70]. First release of GATE was in May 2004 [71]. In publications [72, 73, 74] the evolution of the GATE project is presented. Main additions and improvements implemented in GATE are: modeling Carbon therapy [75], bioluminescence and fluorescence imagin [76], DNA physics [77], synchrotron medical imaging and radiation therapy [78].

GATE is open-source simulation software which use the Geant4 kernel to simulate the interactions between particles and matter. GATE provides additional high-level features, specialized for medical application and written in C++ programming language with user-friendly interface. The simulations can be designed and controlled using macros, without any C++ writing.

This is a power tool dedicated to numerical simulations in medical imaging and radiotherapy such as SPECT (single photon emission computed tomography), PET, CT and optical scans and radiotherapy treatments. This code is flexible enough to model almost any detector design, including modeling detector motion, patient motion, radioactive decay, optical photon tracking, hadronic processes, dead-time, time of flight, tracer kinetics. In addition it can handle analytical or voxelized phantoms with running on a cluster architecture or/and on a grid. GATE can be run on many platforms (Linux, MAC OS, Windows).

Many commercial or prototype systems have already been modeled using GATE and most models have been thoroughly validated, for example, Philips Gemini/Allegro [79], GE Advance/Discovery LS [80], Siemens PET/CT Biograph 6 scanner [81].

The number of publications related to GATE is increasing each year and this

fact indicates high public interest in GATE [82, 83].

In each simulation, the user has to define the scanner geometry, phantom geometry, set up the physics processes, initialize the simulation, set up the detector model, define the source(s), specify the data output format and start the acquisition. Different data formats can be used such as .root .ascii etc.

3.2 Choice of the Cherenkov radiator

In this work we are using the crystalline lead fluoride (PbF_2) as a Cherenkov radiator.

First step for studying this crystal was made in 1954, Kantz and Hofstadter [84] discussed the use of total-absorption spectrometers for high-energy electrons and photons. They outlined the advantage of such devices, and estimated the performance of different absorbing materials. The operation depends on trapping a large fraction of the incident energy within the absorber, which is made large enough to permit soft-shower development. (To keep the dimensions reasonable, absorbers of high atomic number are essential.) This trapped energy is dissipated by ionization along relativistic electron tracks in the absorber. As the absorber is to be transparent, visible light will be emitted by fluorescence and Cherenkov processes: this light pulse is measured by photomultiplier techniques.

In 1968, Dally and Hofstadter [85] first considered this material for electromagnetic calorimetry. They have tested the quite clear 13.3 cm $\times$ 12.7 cm lead fluoride crystal which transmits at least 60 % of visible incident light on one passage through the crystal. The response and resolution of the crystal have been measured with electrons or positrons at energies between 100 MeV and 14 GeV. Two different mountings of the crystal and the photomultipliers for verification the better light collection have been tried. They have concluded, for experiments in high energy physics crystals of still larger diameter are preferred in order to have a large entrance solid angle.

In 1989, Anderson et al have tested two PbF_2 crystals [86], one tested in Brookhaven National Laboratory (BNL) and the other at KEK in Japan. They discovered its properties such as transmission of this crystal, refractive index, melting point, a resolution of 7.2 % (1σ) at 1 GeV. The test-beam results show the estimated number of photoelectrons was 970 for 1 GeV electrons with an estimated shower containment of 90 %, this yields about 1100 photoelectrons/GeV of deposited energy.

Recently, a huge amount of work for investigation of the application of this crystal in PET was done by Korpar et al [13, 14, 15, 87].

In this study we consider the PbF_2 crystal as a Cherenkov radiator, attached to the MCP-PMT, Fig. 3.1. The main parameters of the lead fluoride crystals are summarized in the Table 3.1. A gamma quanta with the energy 511 keV or

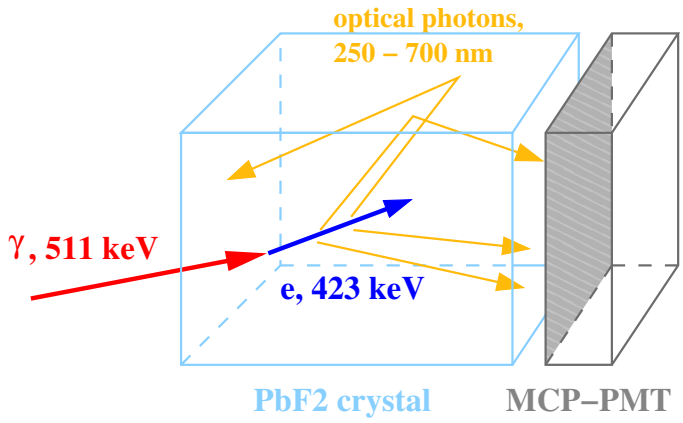

Figure 3.1: Schematic view of the 511 keV gamma detector with PbF_2 crystal using Cherenkov radiation.

Properties	Value
Density [g/cm^3]	7.77
Pb [% by weight]	85
Transparency, wavelength [nm]	> 250
photo-electric fraction at 511 keV [%]	46
Radiation length [cm]	0.93
Moliere radius [cm]	2.22
Index of refraction	1.82
Coefficient of thermal expansion [°C^{-1}]	20×10^{-6}
Melting point [°C]	855

Table 3.1: Main properties of the PbF_2 crystal [86]

less will be converted in the crystal and produce the relativistic electron via the photo-ionization or Compton processes. Such electron usually has sufficient speed to radiate optical photons via the Cherenkov effect. These photons are detected by the micro-channel-plate photomultuplier (MCP-PMT), attached to one of the crystal surfaces. In this simulation we consider the direct contact of the PMT window with crystal without any optical gel. In practice, such configuration could be realized with the molecular bonding procedure [88]. To realize the molecular bonding one requires to reach the surfaces roughness of about 1 nm or better, planarity less than 1 μm and provide extremely clean surfaces, free from any dust particles and hydrocarbon contamination [89].

As the first step of the study we realized a simulation using two back-to-back crystals. The PbF_2 crystals with dimensions 6.5 mm $\times$ 6.6 mm $\times$ 10 mm are molec-

ularly bounded to the sapphire 1.3 mm-thick window. We simulated a radioactive point-source generating two back-to-back 511 keV gamma photons.

Figures 3.2a – 3.2e show the main distributions related to the interaction of the gamma quanta in the crystal. In particular, Fig. 3.2a represents the number of electrons generated in the crystal. Bin with 0 electrons corresponds to the cases when 511 keV photons was not converted in the crystal. Bin with 1 electrons corresponds to the sum of the events with one photoionization conversion or one Compton conversion. The fraction of events with two or more conversion points, e.g. one Compton conversion following by the photoionization or another Compton conversion, is about 30 % of the total number of converted gamma quanta. The corresponding spectrum in electron energy is shown in Fig 3.2b. One can easily distinguish three photopeaks at 423 keV, 498 keV and 507 keV corresponding to K, L and M electron shells (Livermore model is used in the simulation) and the Compton edge from the 511 keV photons at the energy near 340 keV. The number of Cherenkov photons generated per electron for all events is shown in Fig. 3.2c and for events with electron energy more than 420 keV produced by the photoionization is shown in Fig 3.2d. As one can see, in the best case scenario, when electron is generated by the photoionization process, the number of the Cherenkov photons is about 25 which is extremely low compare to the scintillation process, with a number of optical photons of about ten-twenty thousands. The photons wavelength distribution is shown on the Fig. 3.2e. The small number of photons allows us to simulate the propagation of each individual photon in the crystal (contrary to the case of the scintillation crystal) and obtain more reliable result. Such approach is retained for all simulation results presented in this manuscript.

3.3 Photodetection

The widespread use of photon counting in radiation detection would be impossible without availability of devices to convert the extremely weak light output of a light pulse into corresponding electrical signal. A photomultiplier tube (PMT) converts the light signals that typically consist of no more than few hundred of photons into a usable current pulse without adding a huge amount of random noise to the signal [46].

3.3.1 MCP-PMT

The conventional PMT, invented in the 1930s, employs a photocathode to convert the detected photon to a photoelectron, and a discrete dynode electron multiplier to amplify the charge of the single photoelectron to the level that can be recorded

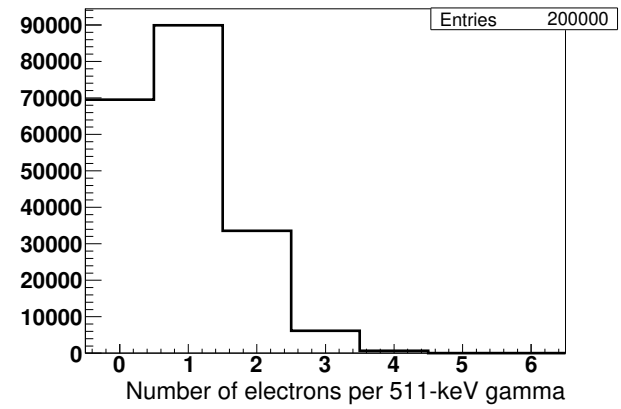

(a)

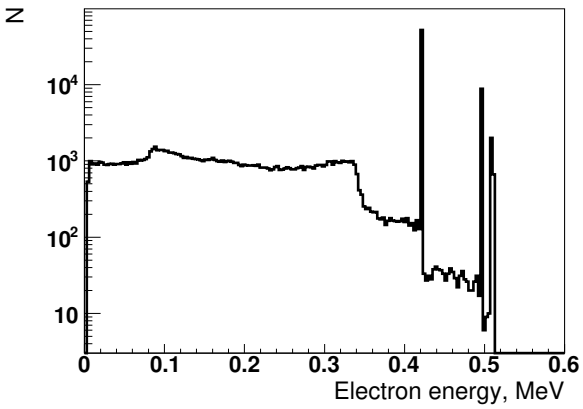

(b)

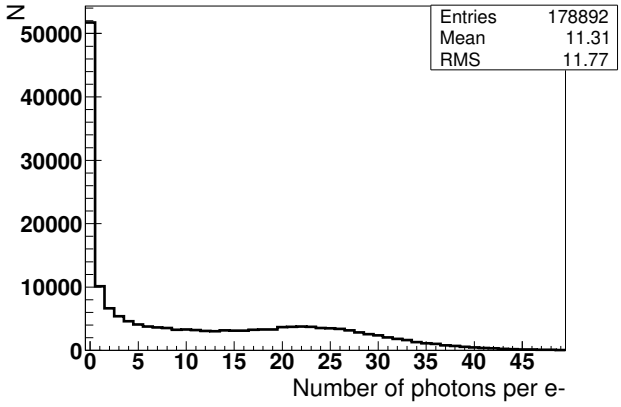

(c)

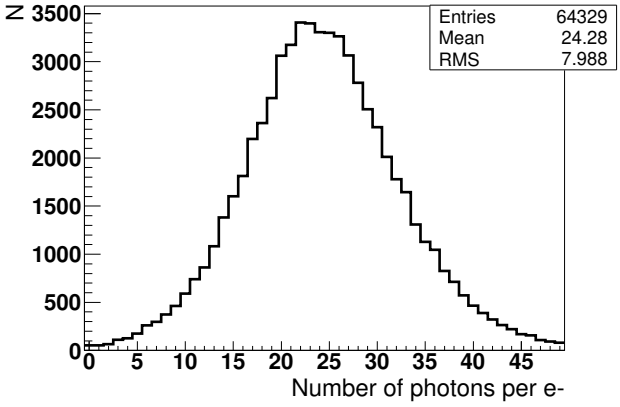

(d)

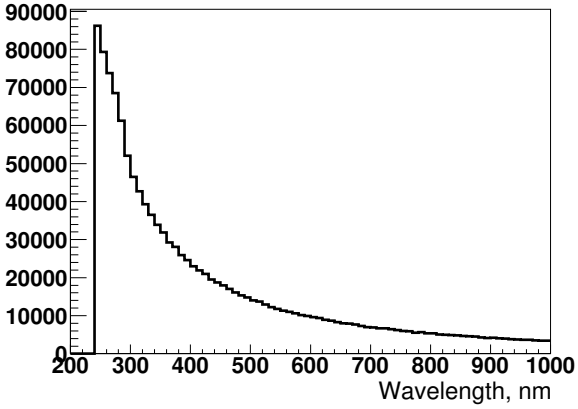

(e)

Figure 3.2: Analysis of interactions inside PbF_2 crystal: (a) distribution of numbers of electrons per 511 keV gamma; (b) energy spectrum of electrons; (c) distribution of numbers of generated photons per electron; (d) distribution of generated photons per electron in case photoionization ($E_e > 423$ keV); (e) spectrum of the optical photons by wavelength generated into lead fluoride crystal.

by electronic circuits [90]. Various dynode configurations, for instance, linear, cage, venetian blind, box-and-grid, fine mesh, etc, have been developed for PMTs.

First important steps for development of continuous-dynode electron (CEM) multipliers were done in the 1960s with production of lead glasses with high-resistance surfaces on through the process of high-temperature and reduction in a hydrogen atmosphere [91]. This led to the independent development of the continuous channel electron multiplier by Oschepkov et al [92] in the Soviet Union, by Goodrich and Wiley [93] at the Bendix Research Laboratories in the USA, and by Adams and Manley [94] at the Mullard Laboratories in the United Kingdom and at the Laboratoires d'Electronique et de Physique Appliquée (LEP) in France.

The mode-of-operation of the channel electron multiplier (CEM) is shown in Fig.3.3. The multiplier is operated under vacuum with a high voltage established along the channel. A high-energy photon or charged particle (primary radiation) striking the wall of the channel releases an electron with some initial energy that is accelerated along the channel axis, drifting across to strike the wall with sufficient energy to release secondary electrons. This process is repeated many times with a final output pulse containing up to 10^8 electrons. As the voltage along the channel is increased, the energy of the electrons striking the wall will increase, but the total number of impacts will decrease. The amplification gain on the applied voltage can be defined as [94]:

$$G = \frac{KV_0^2}{4V\alpha^2}^{4V\alpha^2/V_0}, \tag{3.1}$$

where G is the gain, V_0 is the energy gained by an electron traversing the applied potential difference, V is the initial energy of the secondary electron, α is the length-to-diameter ratio of the channel, K is a constant from the relation $\delta \approx KV_c$, with δ the secondary emission coefficient and V_c the collision energy.

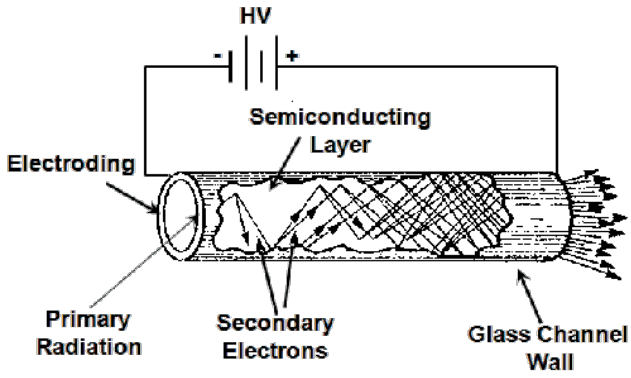

Figure 3.3: Working principle of a channel electron multiplier (CEM).

As we can see from equation 3.1 that the fundamental electrical characteristics of the CEM depend on the length-to-diameter ratio α of the channel and not on the

absolute physical dimensions and the size of the channel can thus be diminished to the current technological limits. Hence, the idea to combine many channels together to produce a detector with an image recording capability was in base of creation a micro-channel plate (MCP) and realized in the first time at the Bendix Research Laboratories in 1962 [95]. The compact channel structure has high spatial and time resolutions in addition with hardness to magnetic fields (see Fig. 3.4).

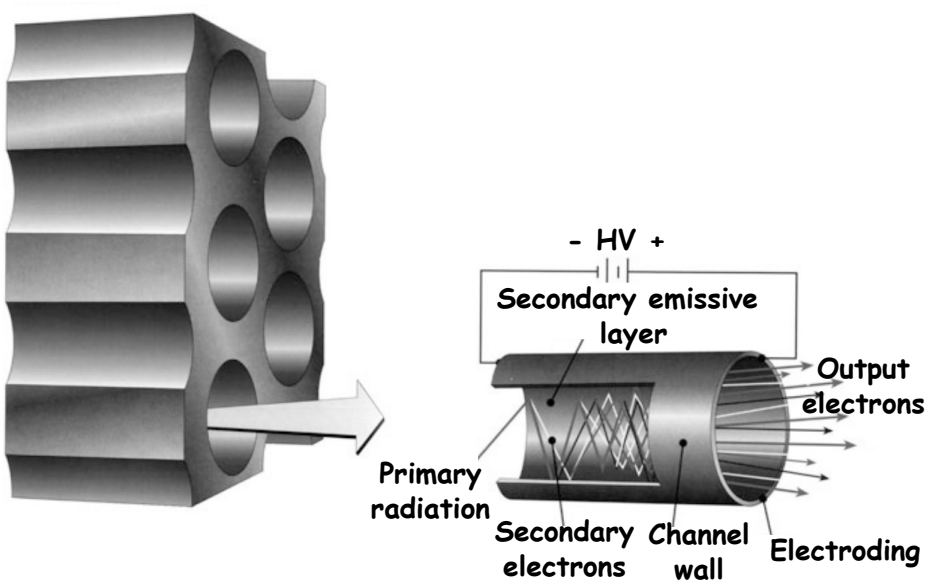

Figure 3.4: A micro-channel plate (MCP) is an array of miniature electron multipliers that are each acting as a continuous dynode chain.

The experimental gain curve does not show a maximum, as predicted by the model, but continues to much higher gain levels and then starts to saturate. This is because, first, the secondary electrons are not all emitted orthogonally, and, second and more important, the gain is enhanced by ion feedback. As shown in the schematic in Fig. 3.3, the voltage that accelerates the electrons down the channel can also accelerate a positive ion, caused by the impact of an electron with a residual gas molecule, back to the input where it can impact the wall and restart the gain process. The level of ion feedback depends both on the ambient pressure and the level of the applied voltage [90]. The feedback of positive ions can be prevented by curving the channel, forcing the ions to impact the wall in a short distance compared with the total channel length.

Typical operating voltages are between 1000 V and 1200 V but at this values the MCP produces a negative exponential output pulse height distribution, with most of the pulses at low amplitudes. This is clearly not optimum for a stable photometric response as a slight reduction in the gain will cause a number of pulses to be lost below the threshold of the electronics, significantly reducing the detective quantum efficiency (QE). Recently MCP-PMT have number of vendors with channel

diameters ranging from 25 μm down to 2 μm. Typically the open-area ratio of the channels is of the order of 60 % of the area of the plate and diameters of circular-format MCPs range from $\approx$ 18 mm to $\approx$ 150 mm.

The maximum gain that can be realized without significant ion feedback in a straight-channel MCP is of the order 10^3 to 10^4. There is several ways to improve this parameter. For instance, three alternative configurations of MCP-PMT without ion feedback called the "chevron", Z-plate and C-plate (see Fig. 3.5). In the chevron MCP stack two straight-channel MCPs with channel bias angles typically in the range from 8° to 10° are mounted in sequence with the bias angles set so that positive ions are trapped at the interface between the two MCPs. The next improvement on the chevron MCP stack is the "Z-plate" MCP stack. In the Z-stack three MCPs with matched resistances are mounted in a butt-faced configuration with the positive ions trapped at the two MCP interfaces [96]. The Z-stack provides a significantly better reduction of ion feedback than the chevron MCP stack and is the most-used high-gain MCP configuration at this time. The third type of high-gain MCP configuration is the curved-channel MCP or "C-plate" MCP. The channels in this MCP are curved in a manner analogous to that of the curved-channel CEM. In 1971 Washington [97] stated that for a curvature sufficient to mask the output 30 % of the channel would be required to effectively suppress ion feedback to the channel input. Nowadays typical relative resolutions for chevron MCP stacks range from $\approx$ 120 % to $\approx$ 60 % at gains around 10^7 and for Z-plate MCP stacks from $\approx$ 60 % to $\approx$ 35 % at gains around 10^8. A single C-plate MCP produces resolutions ranging from $\approx$ 50 % to $\approx$ 35 % at gains around 10^6 [90].

The optimum length-to-diameter ratio W can be definded by [90]:

$$W = \frac{V}{\alpha} \approx 22.5, \tag{3.2}$$

where V is applied voltage, α is length-to-diameter ratio L/D.

Another important characteristic of the detector is resolving time. The transit time spread (TTS) of electrons in a CEM or MCP depends linearly on the channel length, and the transit-time jitter is proportional to the transit time for a given applied voltage and length-to-diameter ratio. CEMs and conventional PMTs typically produce pulses having a FWHM in the range from 5 ns to 30 ns. By comparison MCPs with channel diameters less than 12 μm produce pulses having less than 1 ns (FWHM). For example, a chevron MCP with 5 μm diameter channels produces a pulse width of order 0.5 ns [90]. Due to this MCP-PMT has unique capabilities for fast timing applications, such as time-of-flight technique in PET. This type of detectors in combination with fast electronic readout systems allows to record both the coordinates and the time of arrival of each detected photon to an accuracy set by the pulse-pair resolution of the electronics. Current manufacturing processes,

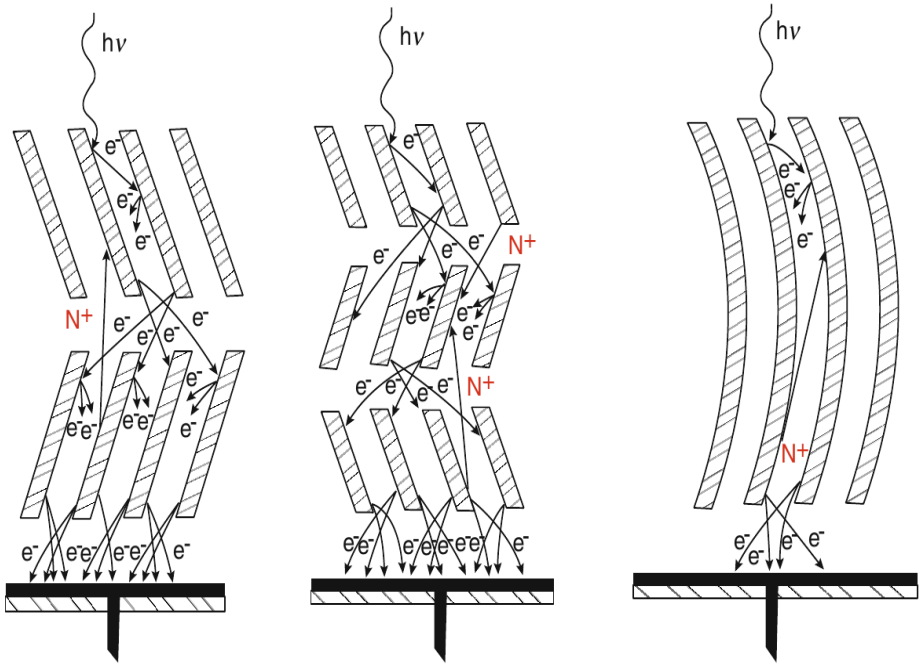

Figure 3.5: High-gain MCP-PMT configurations: chevron MCP stack (left), Z-plate MCP stack (middle) and curved-channel C-plate MCP (right) [90].

that have been developed over the last few years, lead to significant improvement in terms of efficiency, noise, and lifetime performance [98].

The MCP concept is old but the technology is still evolving and improving. For summarizing, MCP-PMT has the following properties and geometrical parameters [98]:

- Good overall area coverage;
- High single-photon detection efficiency optimized for Cherenkov light;
- High gain of typically 10^6;
- Spatial anode segmentation with typically mm pad size;
- Very high speed with typically single-photon TTS of order 50-100 ps;
- Robustness to magnetic field up to 2 T;
- Low noise;
- High photon rate capability for typical illumination levels 200 kHz/cm^2 up to $\geq$ 1 MHz/cm^2;
- Extended lifetime with marginal performance drop over 5-10 years of operation

- Radiation hardness;
- Pore diameter D: 6-25 μm;
- Channel length L: 400-1000 μm;
- Diameter-to-length ratio α: 40-100;
- Open-area-ratio: 55-65 %

Photonis [99] and Hamamatsu [100] are two largest MCP-PMT's developers. Therefore, as a photomultiplier for foreseen Cherenkov TOF-PT scanner was chosen the photodetector model XP85112 by the Photonis Planacon^{TM} (see Fig. 3.6b, 3.6c). It is fast (transit time spread (TTS) is about of 80 ps FWHM) pixelized detector with large active area of 53 mm $\times$ 53 mm [101]. We used a modified version of this detector with 1.3 mm thick sapphire window.

(a)

(b)

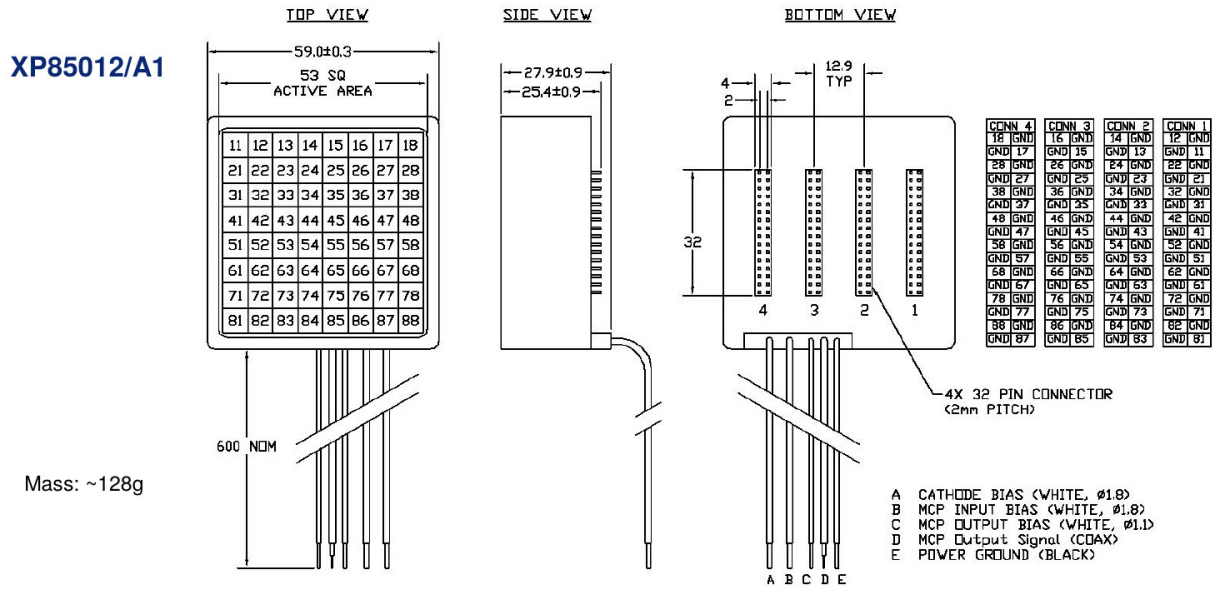

(c)

Figure 3.6: (a)Quantum efficiency of the MCP-PMT from datasheet PLANACON XP 85012 [101]; (b) MCP-PMT XP85112 by Photonis Planacon^{TM}; (c) Top, side and bottom view of MCP-PMT XP85112 by Photonis Planacon^{TM}.

3.3.2 Optical interfaces

The crucial part of the simulation is the description of the optical interface between lead fluoride crystal and the surface of the photocathode. We considered two possible options of the optical interface:

1) molecular bonding, which is simulated as an absence of any media between PbF_2 crystal and PMT window and the null distance between them;

2) interface with the optical gel OCF452 (density 2.33 g/cm^3, transparent for photons with wavelength $\lambda > 300$ nm, refractive index 1.572 @ 400 nm) [102]. The molecular bonding provides the highest efficiency of the photocollection and could be considered as an "ideal interface", but it is rather challenging to realized it in practice. That is why for the experimental tests [103] we are using of the optical gel OCF452 and compared both configurations in our simulation.

We chose to use the sapphire as a material for the optical window because it has the similar refractive index compare to PbF_2 crystal (see Fig. 3.8a). This allows to minimize losses of the optical photons at the optical interface in the case of the molecular bonding. We included in the simulations the following elements of the optical interface: sapphire window with the thickness of 1.3 mm, the Bialkali photocathode with the thickness of 0.1 mm and 100 % absorption efficiency of optical photons. We simulate the production of the signal (photo-electrons) by the absorbed photons with a realistic quantum efficiency calculated from [101] (see Fig. 3.6a).

For configuration with molecular bonding the spectrum of detected photons in the case of the ideal, 100 % photocathode quantum efficiency and the realistic quantum efficiency is shown in Fig. 3.7a. We observe that we detect a significant number of photons below wavelength of 300 nm, which is not possible if the optical gel is in use. The corresponding number of photoelectrons, generated at the photocathode is presented in Fig. 3.7b. As follow from the spectrum, we need to provide a detection threshold below one photoelectron in order to have a reasonable detection efficiency above 30 %. This is the main reason, why in this project we could not consider the use of the SiPM. Indeed, those detectors has an extremely high dark count rate (DQR), about of 100 kHz/mm^2 [104], when detection threshold is below one photoelectron. This leads to the huge number of the random coincidences and make unrealistic the use of SiPM in Cherenkov scanner, without reducing the DQR either by the new SiPM design or by cooling it down.

3.3.3 Crystal coating and detection surfaces

Various properties of the surfaces can be simulated on the Gate platform [54, 105] (see Fig. 1.13). When a perfectly smooth surface is modeling (Fresnel refraction and reflection), the user does not have to provide any special parameters besides

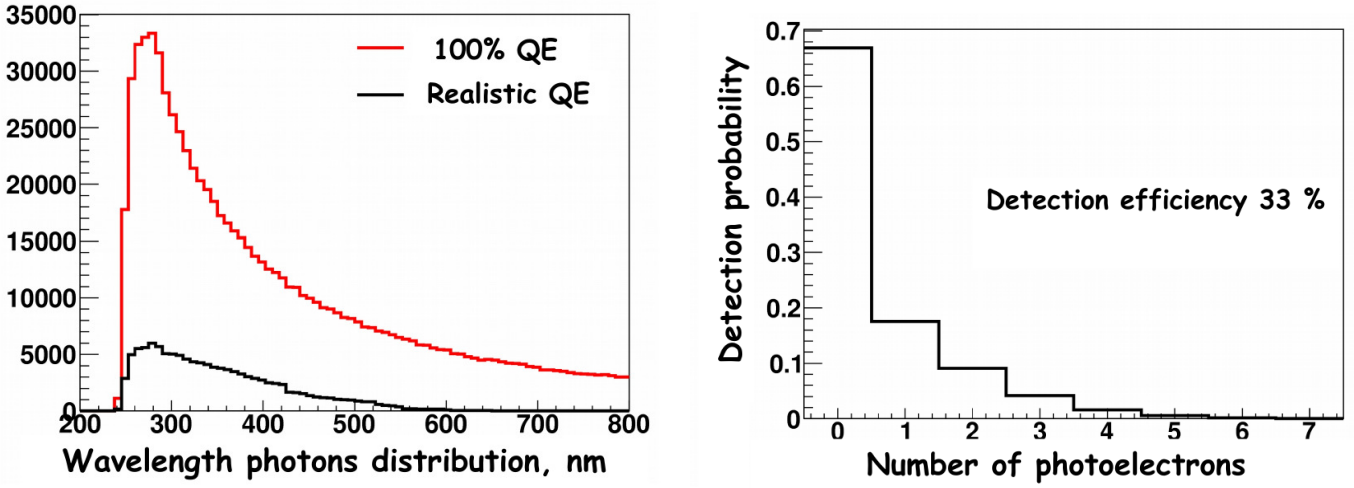

(a) (b)

Figure 3.7: (a) Spectrum of detected optical photons with 100 % quantum efficiency (red curve) and with realistic quantum efficiency (black curve); (b) number of photoelectrons generated at the photocathode in case molecular bonding. Detection efficiency includes gamma conversion efficiency, photocollection efficiency and quantum efficiency of the photocathode.

the refractive index of the two materials on either side of the interface. Thus, the GATE will calculate the probabilities of refraction and reflections from Snell's Law using the Geant4 UNIFIED model, described in the Section 1.4.3.2.

As it known, the ability of the optical photon collection directly depends on the crystal coating. For investigation the influence of the crystal coating on the total efficiency and timing resolution of the scanner, we provided probability options for various reflection types, including possible irregularities of the surface, e.g. surface roughness (see Fig. 3.9).

We considered three different types of the PbF_2 crystal processing: diffuse white, black and polished (see Fig. 3.10). The parameters of each surface we specified in our simulation are shown in Tab. 3.2. The diffuse white coating reflects the light uniformely and independently of the incidence angle with probability of about 95 % (see Fig. 3.10a). The black surface absorbs 100 % of incident light and only optical photons which go directly to the photocathode from the interaction point can be detected (see Fig. 3.10b). Thereby, the photon dispersion is the minimal and the best timing resolution can be achieved but with low efficiency, because only small number of the generated photons has no reflection. The polished coating obeys the Fresnel's laws for transmission and reflection, the angle of reflection is equal to the angle of incidence (see Fig. 3.10c). In this case we simulated a polished-back-painted optical surface with 95 %-reflectivity.

In the same manner we simulated a detection surface of the photocathode MCP-

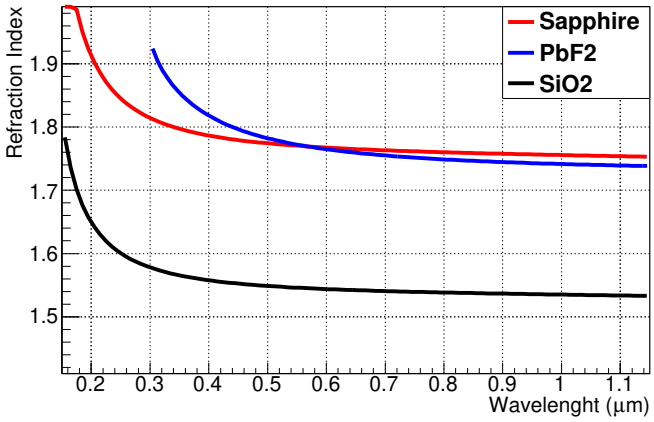

(a)

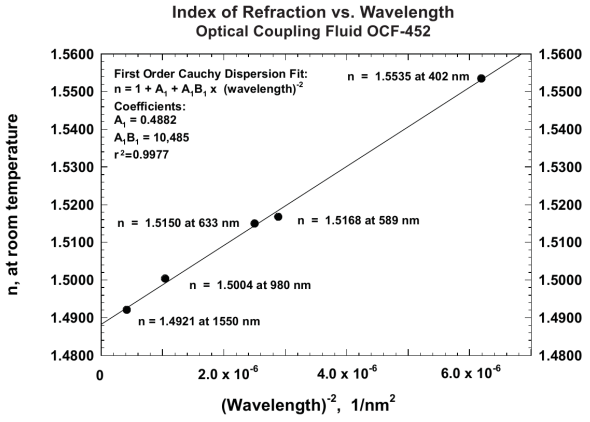

(b)

Figure 3.8: Refractive index of the PbF_2, sapphire and SiO_2 (glass) (a) and of optical gel OCF-452 (b) as a function of the photon wavelength.

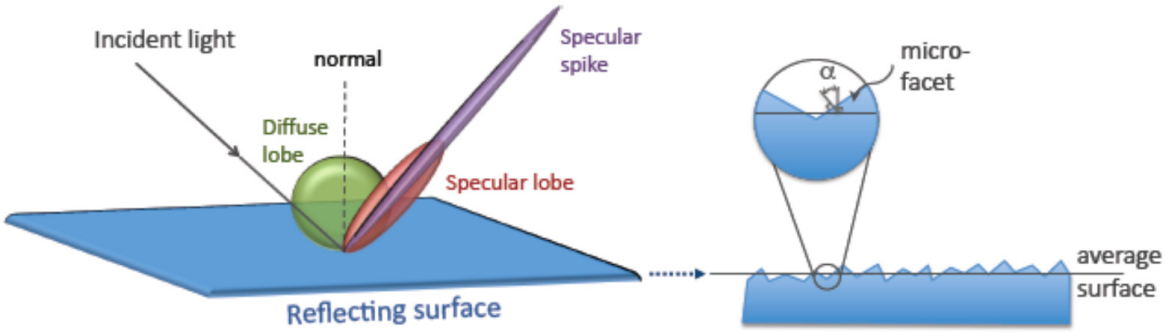

Figure 3.9: In Geant4 UNIFIED model, the probability of micro-facet normals that populates the annulus of solid angle $\sin(\alpha)d\alpha$ is proportional to a Gaussian of sigmaalpha ($\sigma\alpha$) given in degrees. This parameter defines the standard deviation of the Gaussian distribution of micro-facets around the average surface normal. The sum of the four constants (Specular lobe, Specular spike, Backscatter spike and Reflectivity) is constrained to unity [54].

Surface	$\sigma\alpha$	Finish	Efficiency [%]	Reflectivity [%]
Diffuse white	0.0	ground-front-painted	5	95
Black	0.0	ground	100	0
Polished	0.1	polished-back-painted	0	95

Table 3.2: Parameters of the crystal coating.

PMT. The type is dielectric-metal, $\sigma\alpha = 0.0$, the finish attribute is polished. Therefore, the resolving time for different coatings is shown in Fig. 3.11. We simulated

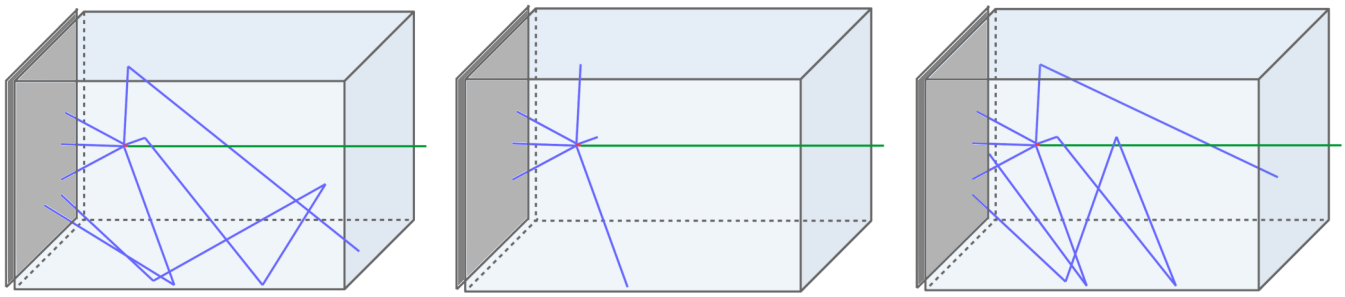

(a) (b) (c)

Figure 3.10: Three PbF_2 crystal coatings were considered: diffuse white (a), black (b) and polished (c). Annihilation 511-keV gamma (green) enters to the PbF_2 crystal and converts to electron (red) which produces Cherenkov photons (blue) uniformly. The signal will be formed by the optical photons which passed through the sapphire window (gray) and absorbed by the photocathode with quantum detection efficiency (see Fig. 3.6a).

two crystal thicknesses 10 mm and 20 mm. Bigger size of the crystal leads to better detection efficiency, because more photons can interact with detector's material but at the same time it gives worse timing resolution due to dispersion of the optical photons in the crystal.

We observe that black coating allows to reach extremely high CRT performance, but current PMT technologies do not allow us to use it fully, and final CRT will be limited by the TTS of the PMT. Additionally, this configuration, has almost 3 times lower efficiency, that will degrade the scanner performance. We also observe that increasing the thickness by a factor of two degrades significantly the CRT performance, but improve the detection efficiency only marginally.

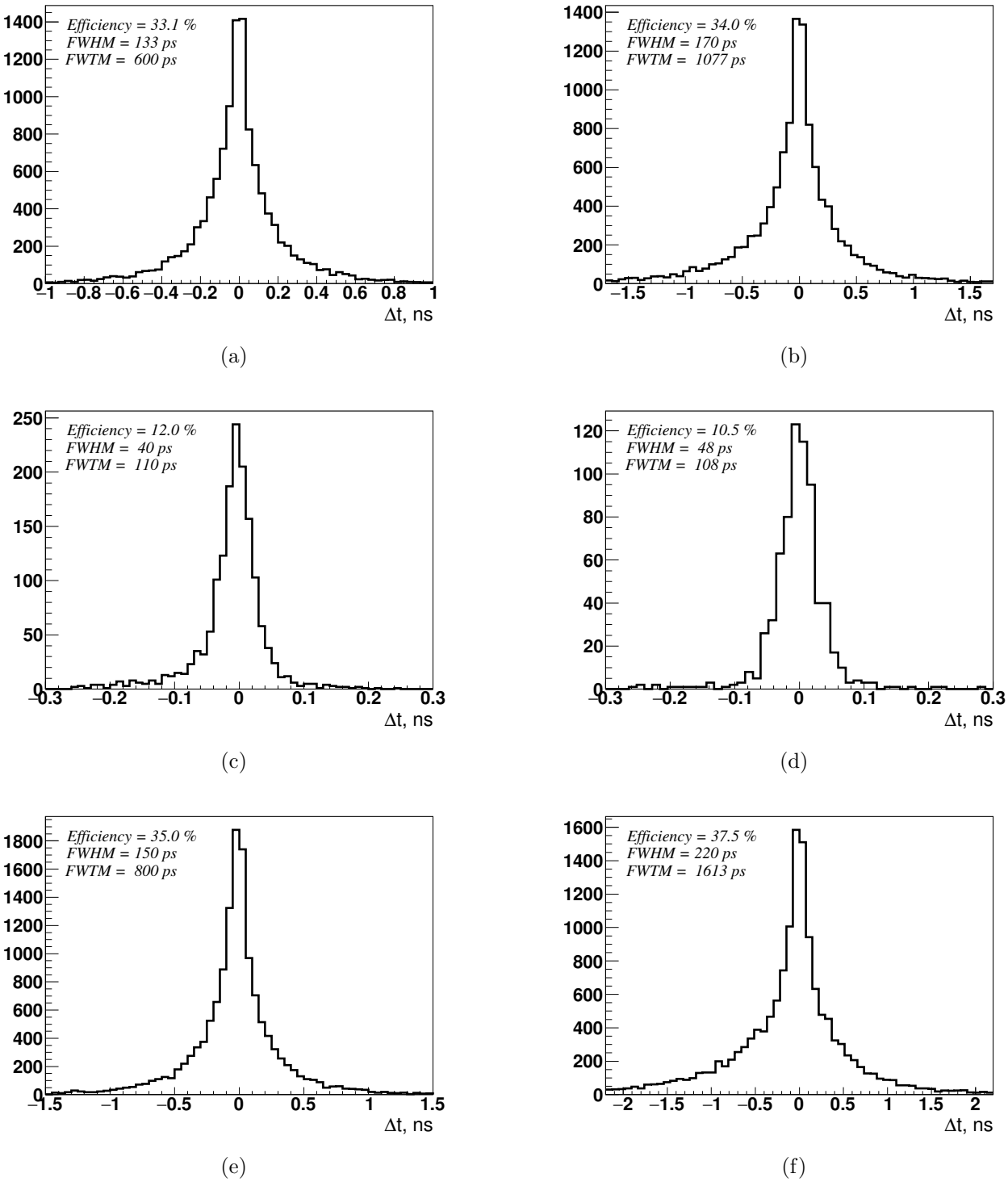

Figure 3.11: Simulating results of the CRT estimation with point-like radioactive source at the center FOV and without TTS of the MCP-PMT for three different crystal coatings and two crystal thicknesses: (a) 10-mm thick and (b) 20-mm thick diffuse white crystal, (c) 10-mm thick and (d) 20-mm thick black crystal, (e) 10-mm thick and (f) 20-mm thick polished lead fluoride crystal.

3.4 Simulated scanner geometry

In order to estimate the potential of the Cherenkov technology for the whole-body PET, we developed the simulation of the complete scanner (see Fig. 3.12a). In the following section we will study different scanner configurations following the NEMA standard [35], and will conclude on the potential of different configurations.

We choose to associated a single PbF_2 crystal to each anode of the MCP-PMT. It results in the detection modules made with one PMT and 64 crystals with the size 6.5 $\times$ 6.5 $\times$ 10 (20) mm^3, glued together. We assume, that each individual crystal is optically isolated from the neighbors and has the diffuse white surface as described above.

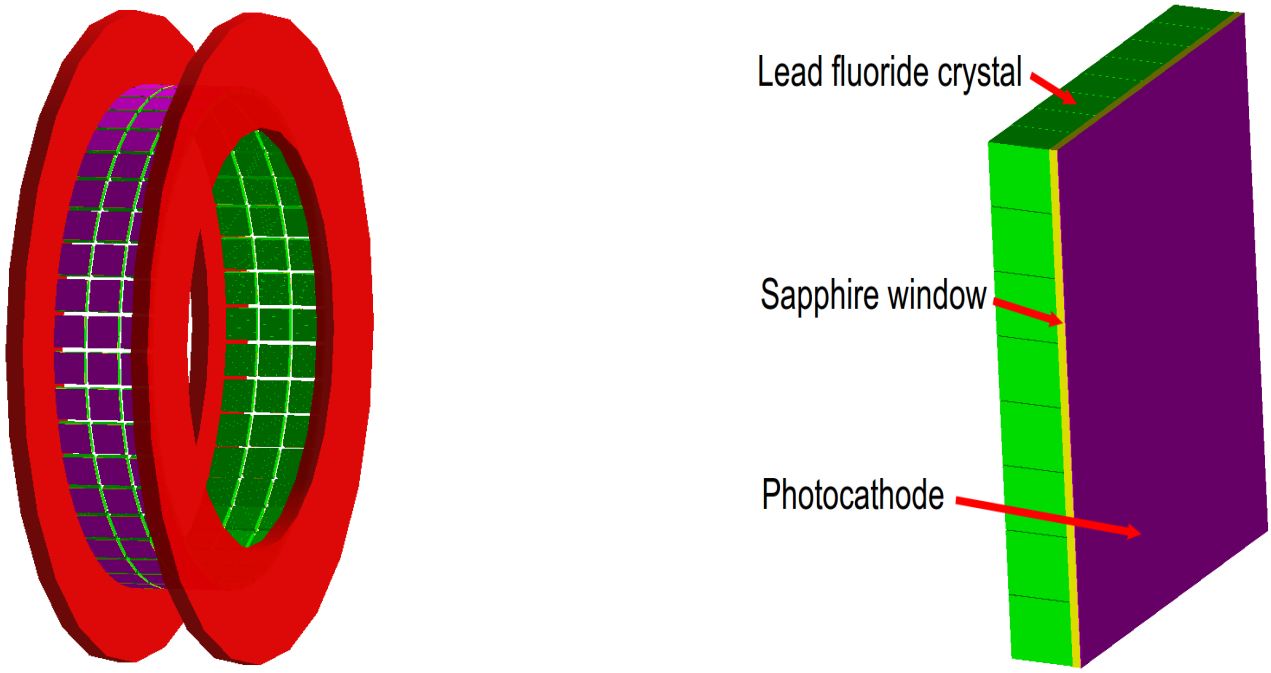

(a) (b)

Figure 3.12: (a) Layout of the three rings whole-body Cherenkov TOF-PET scanner with lead shielding (colored in red) has been used in the GATE simulation; (b) scheme of the PET detection unit, which consists of a block of 64, 8 $\times$ 8 $\times$ 1, individual PbF_2 crystals attached to a single photomultiplier with the same anode structure, 8 $\times$ 8.

We will compare the current simulation with the measurement of the non-TOF commercially available scanner Discovery d-690 [21]. This is a three rings scanner with the axial FOV of 157 mm. To have an equivalent solid angle we chose to simulate the three rings scanner. It results in a axial FOV of 180 mm. We tested the two ring diameters 81 cm and 91 cm. We found that the optimal NECR characteristics

(described in the Section 4.2) are for the diameter 81 cm. Each ring consist of 43 or 48 detection blocks 3.12b and for 81 cm and 91 cm diameters the total number of PMT is 129 or 144 correspondingly. The total number of crystals is 8256 or 9216. We also study the lead shielding option for protecting the scanner from the out-of-FOV gamma (see Fig. 2.4d). We found that a annulus-shape shielding with the internal diameter of 70 cm, external diameter of 108 cm and thickness of 3 cm reduce the out-of-FOV contribution by a factor of 0.2.

Chapter 4

PET performance estimation according to the NEMA NU 2-2007 Standard

4.1 CRT

Coincidence resolving time (CRT) is one of the main characteristics of the scanner. In the Section 3.3.3 we estimated CRT for three different crystal coatings with point-like radioactive source placed in the center of FOV. In this chapter we will discuss only about diffuse white crystal coating because it was chosen as an optimal.

For realistic CRT estimation we take into account the TTS of PMT of 80 ps. We used the polyethylene test phantom, the same as for the NECR calculation (see Section 4.2.1). The linear radioactive source inserted in the phantom at the 45 mm distance from the center FOV. We considered two crystal thicknesses 10 mm (see Fig. 4.1a) and 20 mm (see Fig. 4.1b) with molecular bonding optical interface or optical gel (see Fig. 4.1c). As expected, the best CRTperformance is obtained for the 10 mm crystal with molecular interface bonding.

Compare to our previous results (see Section 3.3.3) we observe a significant degradation, more than expected, for the configuration with the crystal thickness 20 mm. Most probably, this degradation could be explained by the fact that the phantom has rather large diameter of 20 mm. Such configuration will generate a lot of gamma with the large impact parameter (i.e. passing far from the center). In the case of the thick crystal such, non-central, gamma are converted far from the PMT window, and the generated optical photons have trajectories with many reflection, due-to the directional character of the Cherenkov radiation. As it will be explained later in the Section 4.2, the obtained value of CRT will be used to account for the time-of-flight potential in noise equivalent count rates calculation.

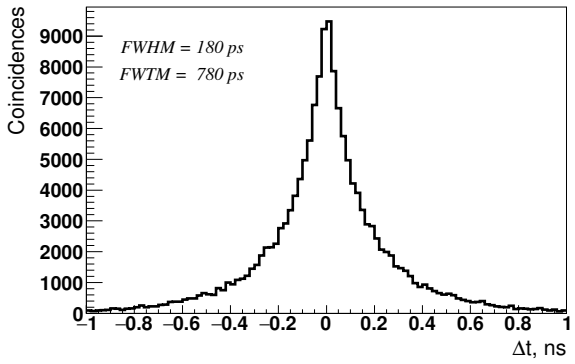

(a)

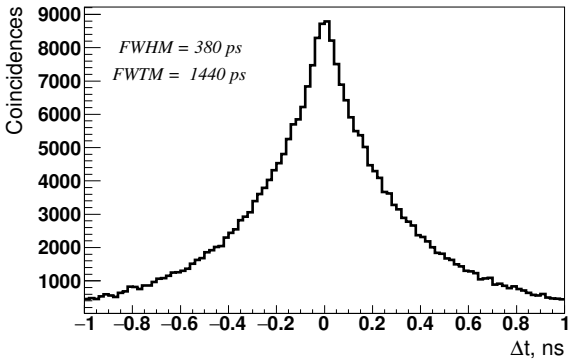

(b)

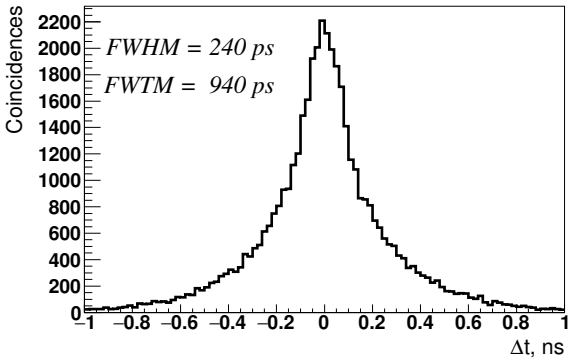

(c)

Figure 4.1: Realistic CRT estimation for configuration with molecular bonding and 10-mm thick crystal (a) and 20-mm thick crystal (b) in comparison with CRT for configuration with optical gel and 10-mm thick crystal (c).

4.2 NECR

Noise equivalent count rates (NECR) is an "effective" count rate, which allows to compare the theoretical signal-to-noise ratios, achievable in images from different scanner without image reconstruction. This parameter is a major arguing point for some vendors determined partly by detector type, detector and scanner geometry, acquisition mode, and front-end electronics. Higher NECR value leads to better image quality. The procedure of the NECR measurement recommended in the standard NEMA [35] is based on the work Strother et al [106] and can be defined by:

$$NECR = \frac{T^2}{T + S + 2R}, \tag{4.1}$$

or

$$NECR = \frac{T^2}{T + S + R}, \tag{4.2}$$

where T, S and R are the number of true, scatter and random coincidences respectively (see definition in section 2.4).

The choice of the 2R or 1R parameter depends on the method used for the estimation of random coincidence number. In our work we choose to compare the simulated results with the measurement of the NECR for conventional PET scanner Discovery-D690 described in the publication Bettinardi et al [21]. They emphasized the importance of presence of a 2R random coincidence term because it is assumed that the randoms estimate is not smoothed. In order to compare equivalent numbers in the following estimations we used 2R definition for all calculations.

4.2.1 Phantom NEMA for NECR

The test phantom is shown in Fig. 4.2 is a circular cylinder composed of the polyethylene with density of 0.96 g/cm^3, with an outside diameter of about 200 mm and with an overall length of about 700 mm [35]. We implemented a 700 mm long, linear radioactive source at the distance of 45 mm from the center of the polyethylene cylinder with inside diameter of 3.2 mm and an outside diameter 4.8 mm. We simulated phantom activities from 10 to 55 kBq/cm^3 (see Tab. 4.1).

In order to speed-up the simulation, we generated directly two back-to-back 511 keV photons in each event, without simulating the radioactive decay and positron thermalization. The distribution of the two-photon vertex (corresponding to the electron-positron annihilation) are chosen to be uniform inside a source and both, ϕ and θ, angular distributions are isotropic.

Activity kBq/cm^3	Total Activity MBq
10	219.8
15	329.7
20	439.6
25	549.5
30	659.4
40	879.2
50	1099.0
55	1208.9

Table 4.1: Activity of the linear radioactive source used for NECR estimation.

Algorithm of the NECR estimation proposed in the standard NEMA [35] imposes to use the sinogram-based procedure. In this procedure each prompt and random sinogram i of each acquisition j is masked with a 12 cm region from the center of the phantom. All the pixels outside the masked region are set to zero. Each projection of the prompt sinogram is shifted to align the pixel with the maximum value in the

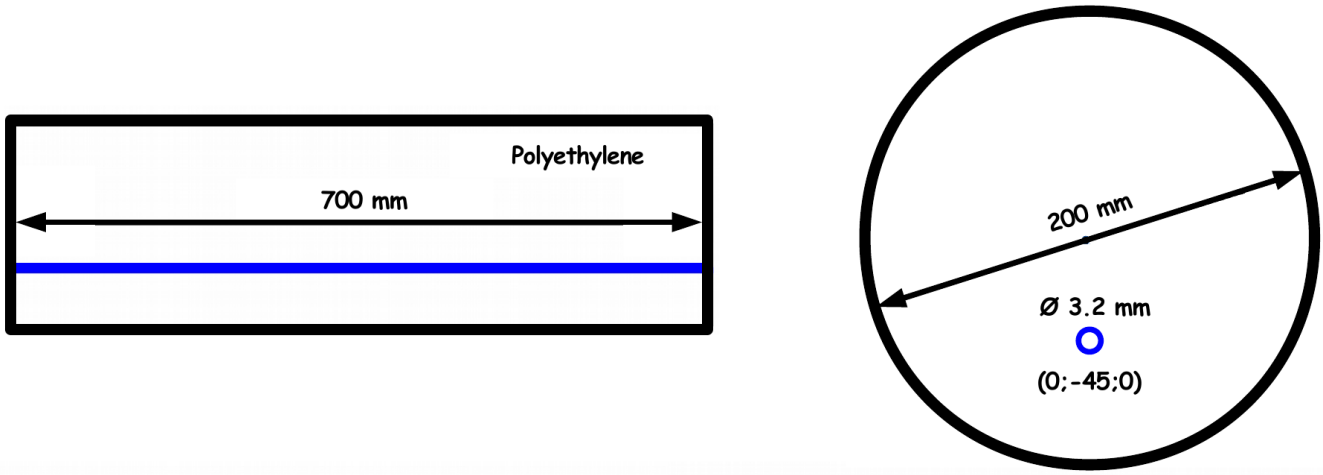

Figure 4.2: The polyethylene test phantom for NECR estimation with linear source insert (blue).

center of the sinogram. The total events number and random events number are calculated as the sum of counts within the masked region. Random plus scatter events were computed by estimating the events under a 40-mm-wide strip centered on the peak and adding these events to counts outside this strip.

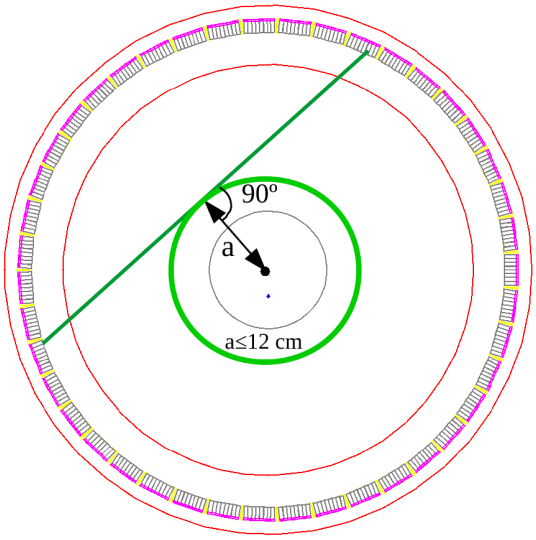

Figure 4.3: LORs selection for NECR estimation.

In this work we used the list-mode output from GATE, which include information about the origin of both detected photon and scattering history for them. In order to simplify the estimation we used the following approach based on the simulation information stored in each coincidence. In this procedure we define the true coincidence as a coincidence where both photons are generated by the same annihilation vertex. Scatter coincidence is a coincidence in which two photons are generated by the same vertex, but at least one photon undergo the Compton scat-

tering in the phantom. The random coincidence is defined as a coincidence where two photons are generated by two different vertexes. To make this procedure closer to the recomended one, we used an additional selection that each LOR should pass close to the phantom center, i.e. at the distance a from the centre of the FOV to LOR smaller than 12 cm (see Fig. 4.3).

We estimated the NECR curves as a function of the activity concentration in the phantom for different scanner configurations. We analyzed the NECR curves for two optical interfaces, for two crystal thicknesses 10 mm (one interaction length) and 20 mm (two interaction lengths) for two sizes of the scanner diameter 81 cm and 91 cm to evaluate the impact of the solid angle and sensitivity of the scanner and considered the influence of the shielding (see Fig. 4.6, 4.7) in comparison with conventional performance Discovery-D690 scanner by General Electrics [21].

To estimate TOF gain in NECR we used an approximation (2.5) proposed in [66]. In our case we used the test phantom with diameter D of 20 cm and the CRT resolution Δt of 180 ps, which give a gain in NECR count about of 7.4 for the 10 mm thick crystal and for 20 mm thick crystal Δt is about of 380 ps, the TOF gain is of about 3.5.

In this estimation we did not account for the dead-time effect, since it is expected to be negligible, at least to the activities of about 50 kBq/cm^3. Indeed the dead-time in the proposed scanner configuration depends mainly on the read-out electronics. In the tests currently undergoing at IRFU [103] a waveform digitizer SAMPIC is used to read-out the photon time. The current version of this module could operate up to rates of 100 kHz, while expected count rate per channel at activity 50 kBq/cm^3 is of about 11 kcps, see Fig. 4.4.

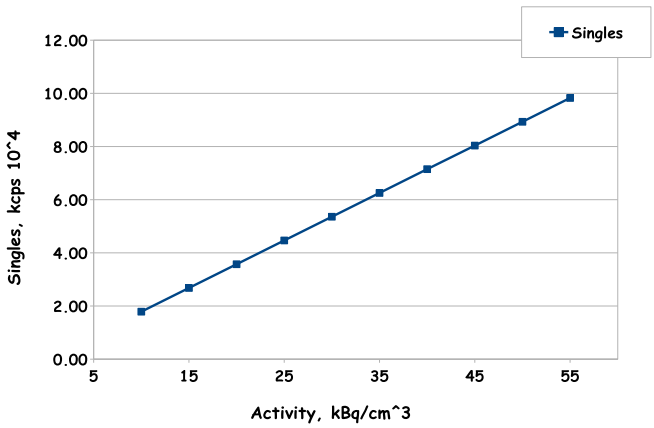

Figure 4.4: Singles as a function of activity for configuration 10 mm thick crystal with 81 cm diameter of the ring for diffuse white crystal coating with molecular bonding without shielding.

Configuration with molecular bonding allows better photon collection at the pho-

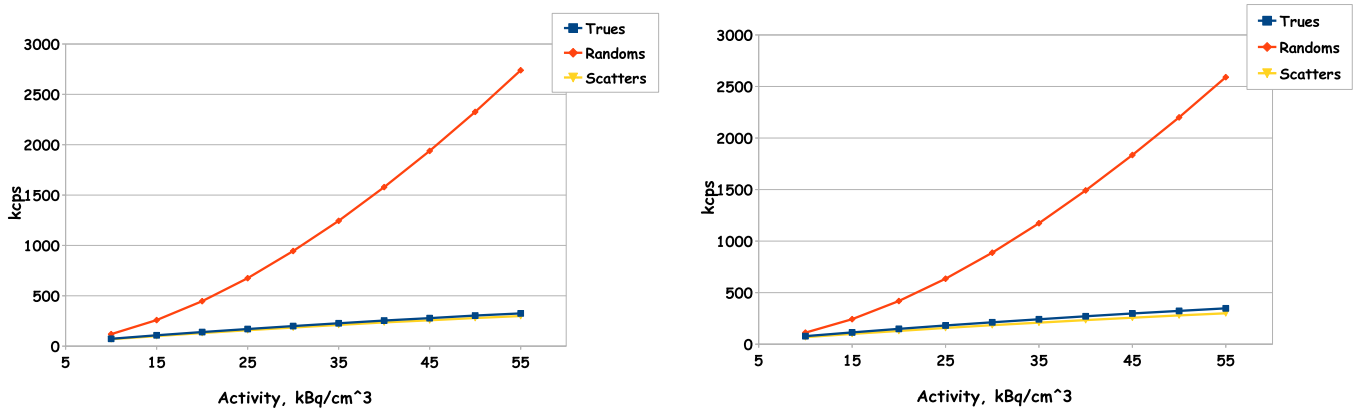

(a) (b)

Figure 4.5: Trues, scatters and randoms coincidence rates as a function of activity for configuration 10 mm thick crystal with 81 cm diameter of the ring for diffuse white crystal coating with molecular bonding (a) and with optical gel (b).

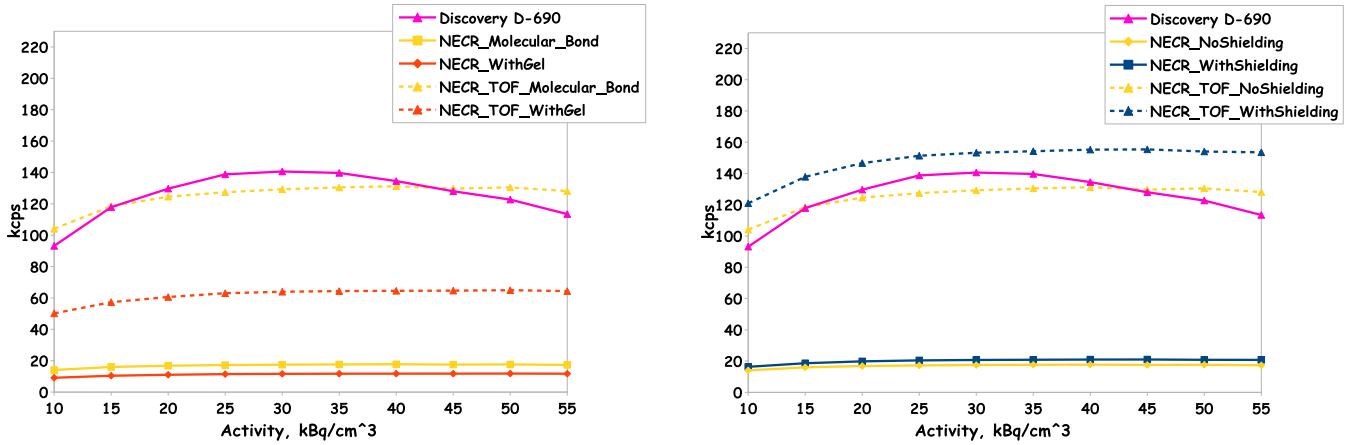

(a) (b)

Figure 4.6: NECR curves of the foreseen Cherenkov TOF-PET whole-body three-rings scanner based on 10-mm thick crystal with diffuse white crystal coating, 81 cm detector's ring diameter in comparison with conventional Discovery-D690 (magenta curve). (a) Comparison of two optical interfaces: molecular bonding (yellow curve) and with optical gel OCF452 (red curve) without TOF (continuous) and with TOF (dashed curves) with the same color of the lines respectively; (b) Influence of the shielding on NECR curves: continuous dark blue curve is NECR curve after implementation the lead shielding in case without TOF and dashed curve is with TOF.

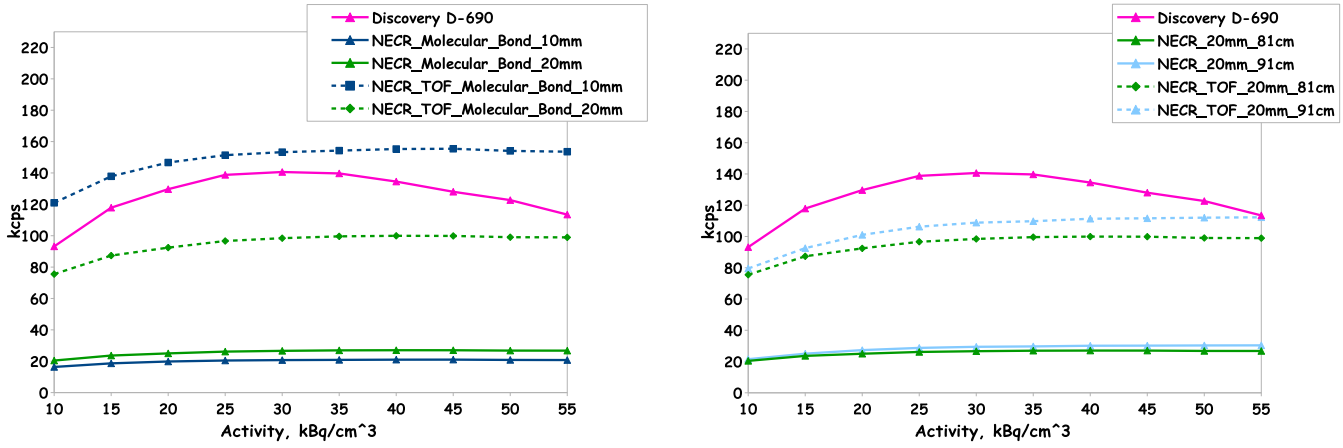

(a) (b)

Figure 4.7: NECR curves of the foreseen Cherenkov TOF-PET whole-body three-rings scanner based on 20 mm thick crystal with diffuse white coating in comparison with conventional Discovery-D690 (magenta curve). (a) Comparison of NECR curves for crystal thicknesses: 10 mm and 20 mm without TOF (dark blue and green curves) and with TOF the same color of lines but dashed respectively; (b) Influence of the scanner size on NECR curves: diameters 81 cm and 91 cm, crystal thickness 20 mm.

tocathode. In case of the optical gel interface, optical photons with large impinging angle are lost due to the reflection at the border between MCP-PMT and gel. The photons with the wavelength smaller than 300 nm are absorbed by the optical gel. This two effects leads to smaller number of the collected photons and large CRT. We see that without TOF, the crystal with 20 mm thickness is slightly more optimal due to the higher efficiency. When we take into account a TOF performance, the crystal with 10 mm thickness became more optimal, because of the better CRT. As shown at the Fig. 4.6b adding a lead shielding improve the NECR by about 20 % due to the better removal of the random coincidences.

The scanner diameter is also an important parameter to optimize. Larger diameter allows to reduce the parallax error and hence improve the spatial precision. It is also improve the NECR values, for example for the scanner with diameter 91 cm increase NECR by about 10 % compare to the diameter 81 cm, Fig. 4.7b. The drawback of the higher diameter is a larger number of the detection module and hence a higher price. For example, increasing the diameter from 81 to 90 cm increases the required number of the photo-detectors from 43 to 48, i.e increase by 11 %. For the following tests we retain a diameter of 81 cm as an optimal configuration for the scanner, with the NECR curves shown at Fig. 4.7a.

The coincidence polices available in GATE are described in the Section 2.4. The preliminary study of the coincidence policies with non-optimized scanner leads to the

#	GATE Policy Name	Coincidences	Trues		Randoms		Scatters		NECR
		kcps	kcps	%	kcps	%	kcps	%	kcps
1	takeAllGoods	1791.630	417.304	23	1036.230	58	338.095	19	61.58
2	takeWinnerOfGoods	985.768	213.284	22	582.339	59	190.145	19	29.01
3	takeWinnerIfIsGood	826.185	175.845	21	491.480	59	158.860	19	23.47
4	takeWinnerIfAllAreGoods	516.313	101.071	20	314.535	61	100.707	20	12.30
5	keepIfOnlyOneGood	513.620	99.821	19	313.055	61	100.744	20	12.05
6	keepIfAnyIsGood	513.966	100.326	20	312.884	61	217.172	20	12.17
7	keepIfAllAreGoods	513.544	100.185	20	312.682	61	100.677	20	12.15
8	killAllIfMultipleGoods	515.014	100.453	20	313.841	61	100.720	20	12.17
9	killAll	514.238	100.155	19	313.633	61	100.450	20	12.12

Table 4.2: Comparison GATE coincidences policies for NECR estimation.

decision to use policy #2 takeWinnerOfGoods. We should note that the Cherenkov detector in the current configuration does not allow to measure the energy, but the signal charge measured by PMT represents the number of the detected optical photons. We redone the study of the coincidence policy using the optimized scanner configuration. The results of this test are shown in the Table 4.2 calculated for the activity of 30 kBq/cm3. It was found that the most optimal policy is a policy #1 takeAllGoods. Unfortunately, the time constrains and significant CPU necessary for the NECR calculation, does not allow us to recalculate the new NECR in time to be included to this manuscript, but this recalculation are foreseen to be done for publication.

4.3 Spatial Resolution

To estimate the spatial resolution of the scanner we follow the NEMA standard [35] recommendation and simulate six small point-like sources which are localized as following:

In the axial direction, along planes (1) at the center of the axial FOV and (2) one-fourth of the axial FOV from the center of the FOV.

In the transverse direction the source was positioned (1) 1 cm vertically from the center (to represent the center of the FOV, but positioned to avoid any possible inconsistent results at the very center of the FOV), (2) at x = 0 and y = 10 cm, and (3) at x = 10 cm and y = 0 (see Fig. 4.8).

The transverse FOV and image matrix size determine the pixel size in the transverse slice. In order to measure the width of the point spread function as accurately as can practically be achieved, its FWHM should span at least three pixels. We expected FWHM is about of 5 mm. We chose to use the pixel size of 1 mm (it should be no bigger than one-third of the expected FWHM in all three dimensions during

At 1 cm radius	
Transverse	$RES = \big(RESx(0;1;center) + RESy(0;1;center) + RESx(0;1;1/4FOV) + RESy(0;1;1/4FOV)\big)/4$
Axial	$RES = \big(RESz(0;1;center) + RESz(0;1;1/4FOV)\big)/2$
At 10 cm radius	
Transverse radial	$RES = \big(RESx(10;0;center) + RESy(0;10;center) + RESx(10;0;1/4FOV) + RESy(0;10;1/4FOV)\big)/4,$
Transverse tangential	$RES = \big(RESy(10;0;center) + RESx(0;10;center) + RESy(10;0;1/4FOV) + RESx(0;10;1/4FOV)\big)/4,$
Axial resolution	$RES = \big(RESz(10;0;center) + RESz(0;10;center) + RESz(10;0;1/4FOV) + RESz(0;10;1/4FOV)\big)/4,$

Table 4.3: According to NEMA 2-2007 standard [35], this is formulas for spatial resolution estimation, where $RESi$ is a measurement of the size of the reconstructed image FWHM of a point source i, center is a point with z coordinate equals 0 and $1/4FOV$ for foreseen Cherenkov PET scanner is 4.5 cm.

reconstruction). Each FWHM was determined by linear interpolation between adjacent pixels at half the maximum value of the response function. The maximum value was determined by a parabolic fit using the peak point and its two nearest neighboring points respectively (see Fig. 4.9-Fig. 4.14).

We used following formulas to evaluate our results (see Tab. 4.3) of the axial, radial and tangential resolutions (FWHM) for each radius (center FOV and 10 cm), averaged over both axial positions. The acollinearity of 0.5° of two photon was taken into account.

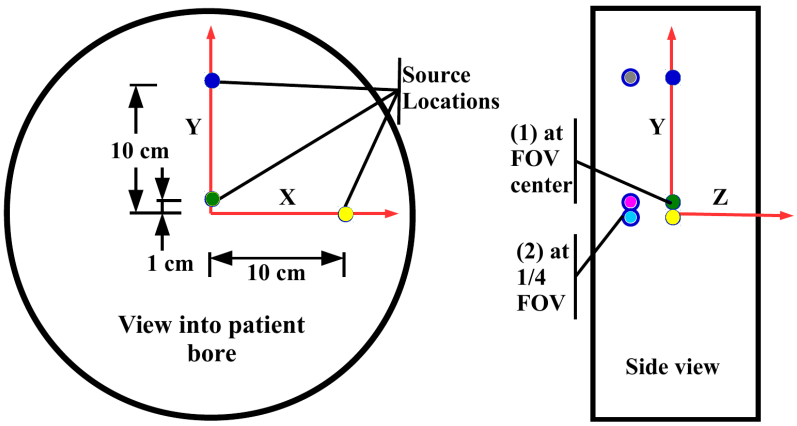

Figure 4.8: Positioning of the radioactive sources for spatial resolution estimation of the foreseen Cherenkov PET scanner with axial FOV 18 cm. The sources were fixed parallel to the long axis of the tomograph and located at 6 points as follows: 1: (0; 1; 0) is green; 2:(0; 10; 0) is blue; 3: (10; 0; 0) is yellow; 4: (0; 1; -4.5) is magenta; 5: (0; 10; -4.5) is gray; 6: (10; 0; -4.5) is cyan. All coordinates of the radioactive sources are given in cm.

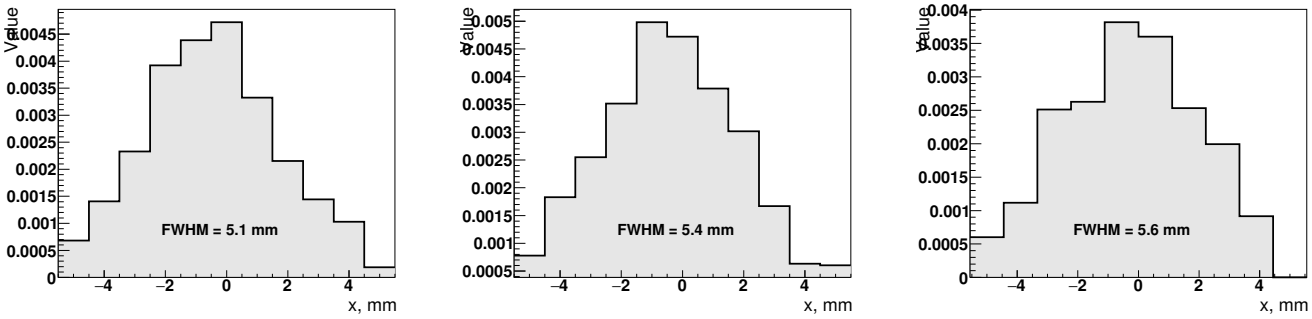

(a) (b) (c)

Figure 4.9: (a) X-profile, (b) Y-profile and (c) Z-ptofile for point-like source at position (0;1;0).

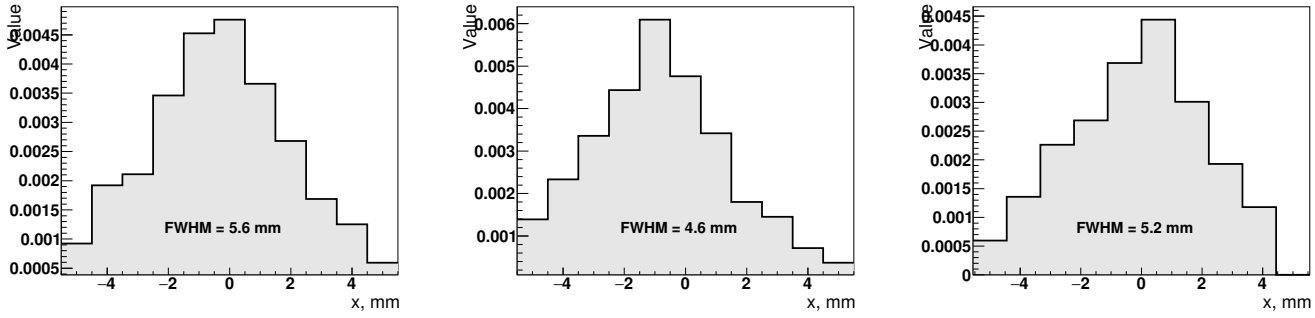

(a) (b) (c)

Figure 4.10: (a) X-profile, (b) Y-profile and (c) Z-ptofile for point-like source at position (0;10;0).

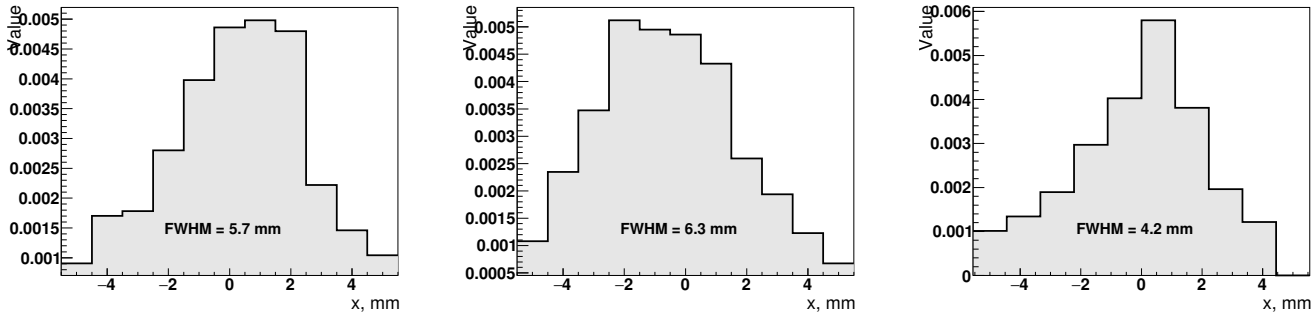

(a) (b) (c)

Figure 4.11: (a) X-profile, (b) Y-profile and (c) Z-ptofile for point-like source at position (10;0;0).

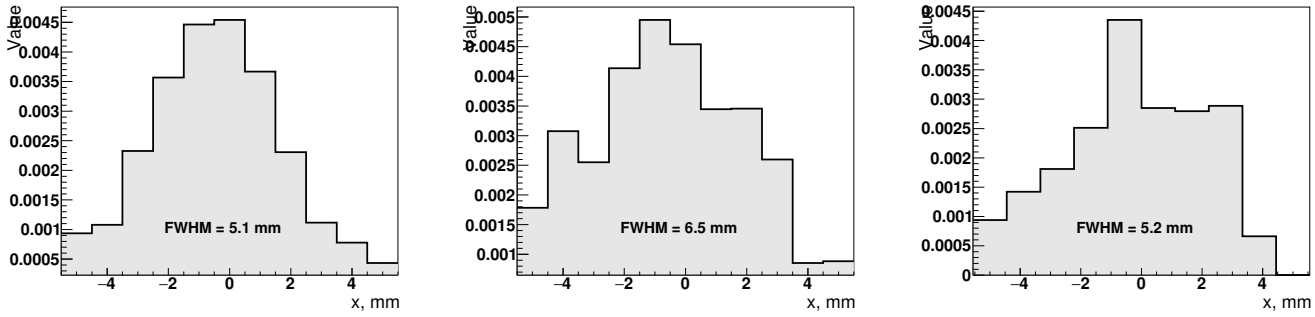

(a) (b) (c)

Figure 4.12: (a) X-profile, (b) Y-profile and (c) Z-ptofile for point-like source at position (0;1;-4.5).

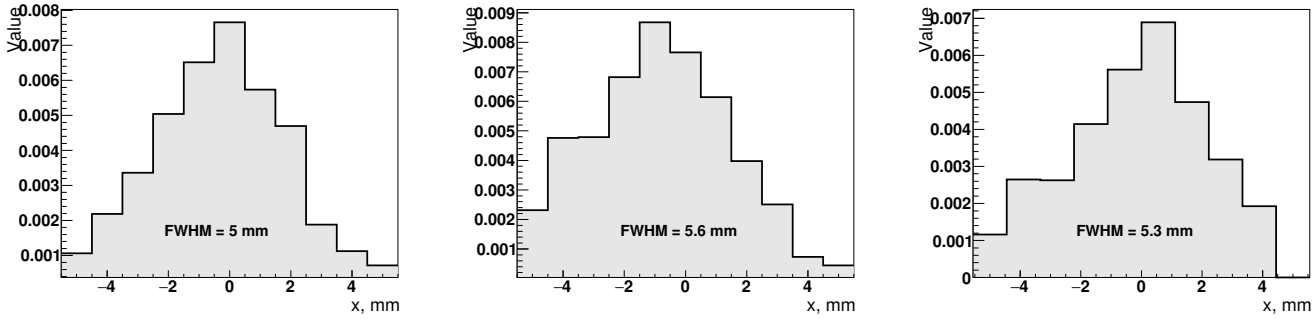

(a) (b) (c)

Figure 4.13: (a) X-profile, (b) Y-profile and (c) Z-ptofile for point-like source at position (0;10;-4.5).

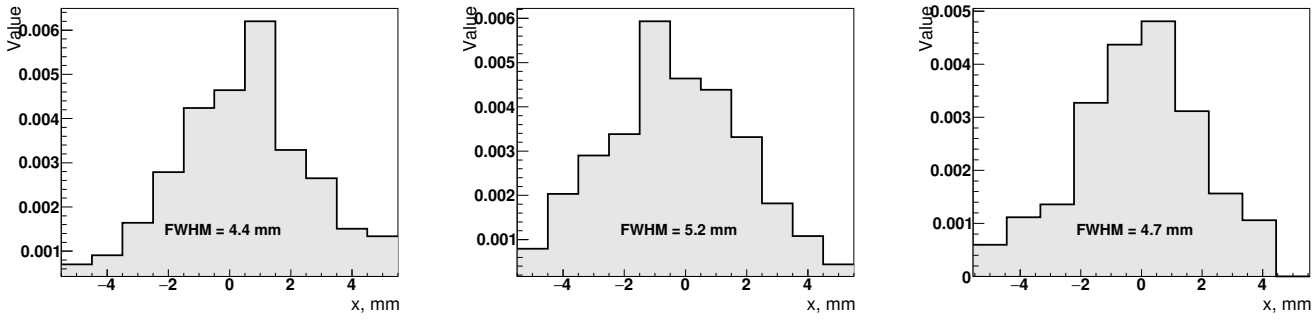

(a) (b) (c)

Figure 4.14: (a) X-profile, (b) Y-profile and (c) Z-ptofile for point-like source at position (10;0;-4.5).

As was expected, spatial resolution degrades from the center FOV to a periphery from 4.5 to 6.5 mm on each axis respectively and comparable with spatial resolution of the conventional scanner Discovery D-690 [21]. The estimated uncertainty is about half of the voxel size, i.e.± 0.25 mm. The configuration with molecular bonding has spatial resolution comparable with optical gel configuration and slightly better than spatial resolution of the conventional scanners. This explains by the fact that in our configuration the crystal size and FOV are similar to the conventional scanner,but we study the PbF_2 crystal with small thickness, 10 mm, and hence smaller parallax error due to the uncertainty on DOI. In addition, PbF_2 crystal has a two times higher photo-electric fraction than LYSO crystals and, consequently, the number of events with two conversion points (one Compton scattering and one photo-ionization) is smaller. Such events with two conversion points will have worse spatial resolution, when these conversions happen in the different crystals.

4.4 Image quality and Contrast Recovery Coefficients (CRC)

The prediction of the image quality of the foreseen Cherenkov PET scanner is non-trivial procedure due to the complex interplay of many different aspects of the system performance.

Standard NEMA proposes to compare the image quality of different systems using a standardized image quality phantom that simulates a clinical imaging condition. The proposed phantom with non-uniform attenuation (see Fig. 4.15) is filled with background activity. It contains four "hot" spheres, e.g. spheres with activity significantly higher than the background one, and two "cold" spheres, e.g. spheres with no activity. Six spheres have different diameters and are used to estimate the contrast recovery after the image reconstruction, while background region is used to estimate the background variability.

The concentration of the background activity in the phantom is 5.3 kBq/cm^3, which corresponds to typical injected dose for whole-body studies. The total volume of the body phantom was divided on 4 parts (I, II, III and IV). For each part the partial volume was calculated with subtraction of the volumes of all inserts: $V_I = 6809.44[cm^3], V_{II} = V_{III} = 996[cm^3], V_{IV} = 2289.84[cm^3]$.

Voxel size is 2.5 mm and reconstructed image is 128 × 128 pixels. We did not reconstruct whole length of the phantom in order to reduce the CPU time needed for the reconstruction, but only region with hot and cold spheres were reconstructed plus ± 4.25 cm from the central slice (#18), 35 slices in total.

A transverse image centered on the cold and hot spheres is used in the analysis, which was provided in the FIJI (the latest version of ImageJ) analysis software [107].

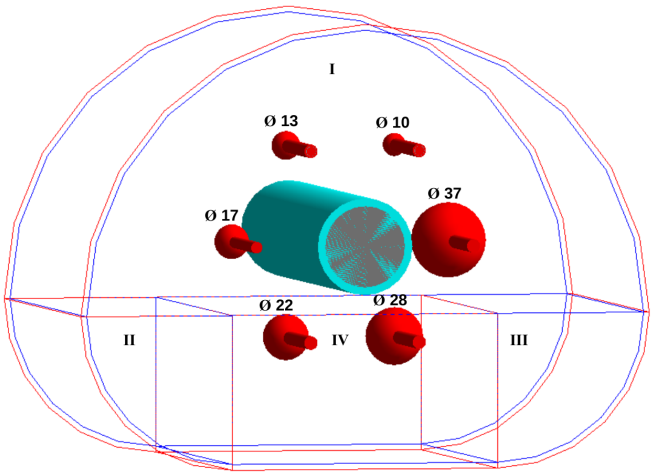

Figure 4.15: Image quality phantom as it implemented in the GATE simulation. Four smallest spheres with diameters 10 mm, 13 mm, 17 mm and 22 mm are filled with water and and activity with a concentration of 4 or 8 times of the background (the session is called "hot") and two biggest spheres with diameters of 28 mm and 37 mm are filled with no-radioactivity water (the session is called "cold").

The same slice is used for all spheres. Regions of interest (ROIs) is drawn on each hot and cold sphere. A circular ROI is used with a diameter equal to the inner diameter of the sphere being measured. The ROI analysis tool takes into account partial pixels and also permit movement of the ROI in increments of 1 mm or smaller. ROIs of the same sizes as the ROIs drawn on the hot and cold spheres is drawn in the background of the phantom on the slice centered on the spheres. Twelve 37 mm diameter ROIs is drawn throughout the background at a distance of 15 mm from the edge of the phantom but no closer than 15 mm to any sphere (see Fig. 4.17).

The coordinates of these twelve ROIs in XY plane are (58;28), (32;36), (21;47),

Sphere	**R, cm**	**V, cm^3**	**A$_{4xBG}$, kBq**	**A$_{8xBG}$, kBq**	**Global position, cm**
sphere10in	0.50	0.52	11.024	22.048	(2.86; 4.95; 3.70)
sphere13in	0.65	1.15	24.380	48.760	(-2.86; 4.95; 3.70)
sphere17in	0.85	2.57	54.484	105.897	(-5.72; 0.00; 3.70)
sphere22in	1.1	5.58	118.296	236.592	(-2.86; -4.95; 3.70)
sphere28in	1.4	11.50	–	–	(2.86; -4.95; 3.70)
sphere37in	1.85	26.53	–	–	(5.72; 0.00; 3.70)
Σ			208.184	416.368	

Table 4.4: Hot and cold spheres for image quality estimation test.

(12;60), (14;75), (25;86), (39;91), (57;91), (83;89), (97;84), (105;70) and (84;35) in image coordinate (see Fig. 4.16).

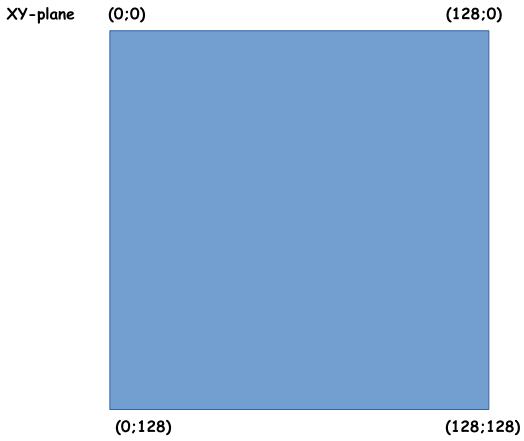

Figure 4.16: Image coordinates in pixels.

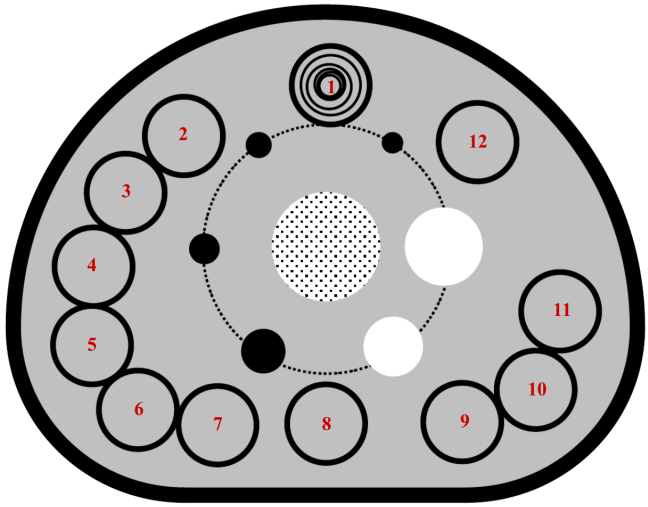

Figure 4.17: For background variability estimation twelve regions of interest (ROIs) were chosen to +/-1 cm and +/-2 cm on either side of the central slice with diameters are close as possible to the physical inner diameters of the spheres from 10 mm to 37 mm. ROIs of the smaller sizes (10, 13, 17, 22, and 28 mm) are drawn concentric to the 37-mm background ROIs.

In total of 60 background ROIs of each size, 12 ROIs on each of 5 slices were considered (slices 10th, 14th, 18th, 22nd and 26th). The locations of all ROIs were fixed between successive measurements (e.g., replicate scans). The average number of counts in each background ROI was recorded. The percent contrast $Q_{H,j}$ for each

hot sphere j is calculated by:

$$Q_{H,j} = \frac{\frac{C_{H,j}}{C_{B,j}} - 1}{\frac{a_H}{a_B} - 1} \cdot 100\ \%, \tag{4.3}$$

where $C_{H,j}$ is the average number of counts in the ROI for sphere j; $C_{B,j}$ is the average number of the background ROI counts for sphere j; a_H is the activity concentration in the hot spheres, and a_B is the activity concentration in the background.

The percent contrast $Q_{C,j}$ for each cold sphere j is calculated by:

$$Q_{C,j} = \left(1 - \frac{C_{C,j}}{C_{B,j}}\right) \cdot 100\ \%, \tag{4.4}$$

where $C_{C,j}$ is the average number of counts in the ROI for sphere j; $C_{B,j}$ is the average number of the 60 background ROI counts for sphere j.

The percent background variability N_j for sphere j is calculated as:

$$N_j = \frac{\sigma_j}{C_{B,j}} \cdot 100\ \%, \tag{4.5}$$

where σ_j is the standard deviation of the background ROI counts for sphere j, calculated as:

$$\sigma_j = \sqrt{\frac{\sum_{k=1}^{k} \left(C_{B,j,k} - C_{B,j}\right)^2}{(k-1)}}, k = 60. \tag{4.6}$$

The wall thickness of the spheres is of 1 mm. Phantom material described in NEMA is polymethylmethacrylate, for modeling we used material plastic with density 1.18 g/cm^3, molecular formula $C_5H_8O_2$.

Estimated contrast recovery coefficients Q_j [%] and background variability N_j [%] are shown in Tab. 4.5 – Tab. 4.8.

In particular, Tab. 4.5 represents CRC in case any attenuation corrections (NoCorr) and with attenuation correction procedure (WithCorr) for configurations without TOF (NoTOF) and with TOF capability (TOF) for 1 hour scanning, (see Fig. 2.10). Attenuation correction in the phantom improves the ratio signal-to-noise at least of 2.5 times.

For more realistic estimation of the CRC we decreased the scanning time to 15 min and investigated the impact of the number of iterations and subsets on the quality of the PET image, Tab 4.6.

Sphere, mm	Parameter, %	NoTOF		TOF 140 ps	
		NoCorr	WithCorr	NoCorr	WithCorr
10	$Q_{H,j}$	-0.9	7.3	3.7	11.5
	N_j	15.2	6.2	7.8	5.2
13	$Q_{H,j}$	0.9	8.8	6.9	16.3
	N_j	13.2	5.2	7.4	4.5
17	$Q_{H,j}$	3.3	17.1	12.7	25.3
	N_j	13.1	4.6	7.3	4.1
22	$Q_{H,j}$	6.2	21.4	18.0	31.0
	N_j	13.2	4.2	7.3	3.8
28	$Q_{C,j}$	52.3	4.2	41.1	25.1
	N_j	13.2	4.1	7.3	3.7
37	$Q_{C,j}$	53.8	5.5	44.1	28.6
	N_j	17.3	4.7	8.6	4.2

Table 4.5: Contrast recovery factor Q_j [%] and background variability N_j [%] without attenuation correction (NoCorr) and with attenuation correction (WithCorr) for cases without TOF (NoTOF) and with TOF capability (TOF <CRT> [ps]), time of scanning is 1 hour (see Fig. 2.10).

Sphere	5 subsets, 1st iteration				no subsets, 5th iteration				no subsets, 10th iteration	
	NoTOF (0.0022)		TOF 250 ps		NoTOF (0.0016)		TOF 250 ps		TOF 250 ps	
	Q_j	N_j	Q_j	N_j	Q_j	N_j	Q_j	N_j	Q_j	N_j
10	2.9	5.7	4.1	9.2	2.9	5.8	4.3	9.3	5.6 (+23%)	14.2 (+35%)
13	3.1	5.3	6.8	8.5	3.1	5.3	6.7	8.5	12.6 (+47%)	9.5 (+11%)
17	5.2	5.2	11.2	7.9	5.1	5.2	11.1	7.9	12.7 (+13%)	11.4 (+31%)
22	8.1	4.9	14.7	6.7	8.0	4.9	14.6	6.7	16.7 (+13%)	9.1 (+26%)
28	3.1	4.6	34.6	6.0	3.4	4.6	34.6	6.0	43.4 (+20%)	8.0 (+25%)
37	-1.4	5.5	35.6	5.0	-1.4	5.5	35.7	5.1	40.0 (+11%)	6.0 (+15%)
									+21%	+24%

Table 4.6: The contrast recovery factor Q_j [%] and background variability N_j [%] with attenuation correction in the phantom for scanning time 15 min and lower initial contrast (4xBG) in case of variable number of iterations and subsets for MLEM image reconstruction algorithm (see Fig. 4.18)

.

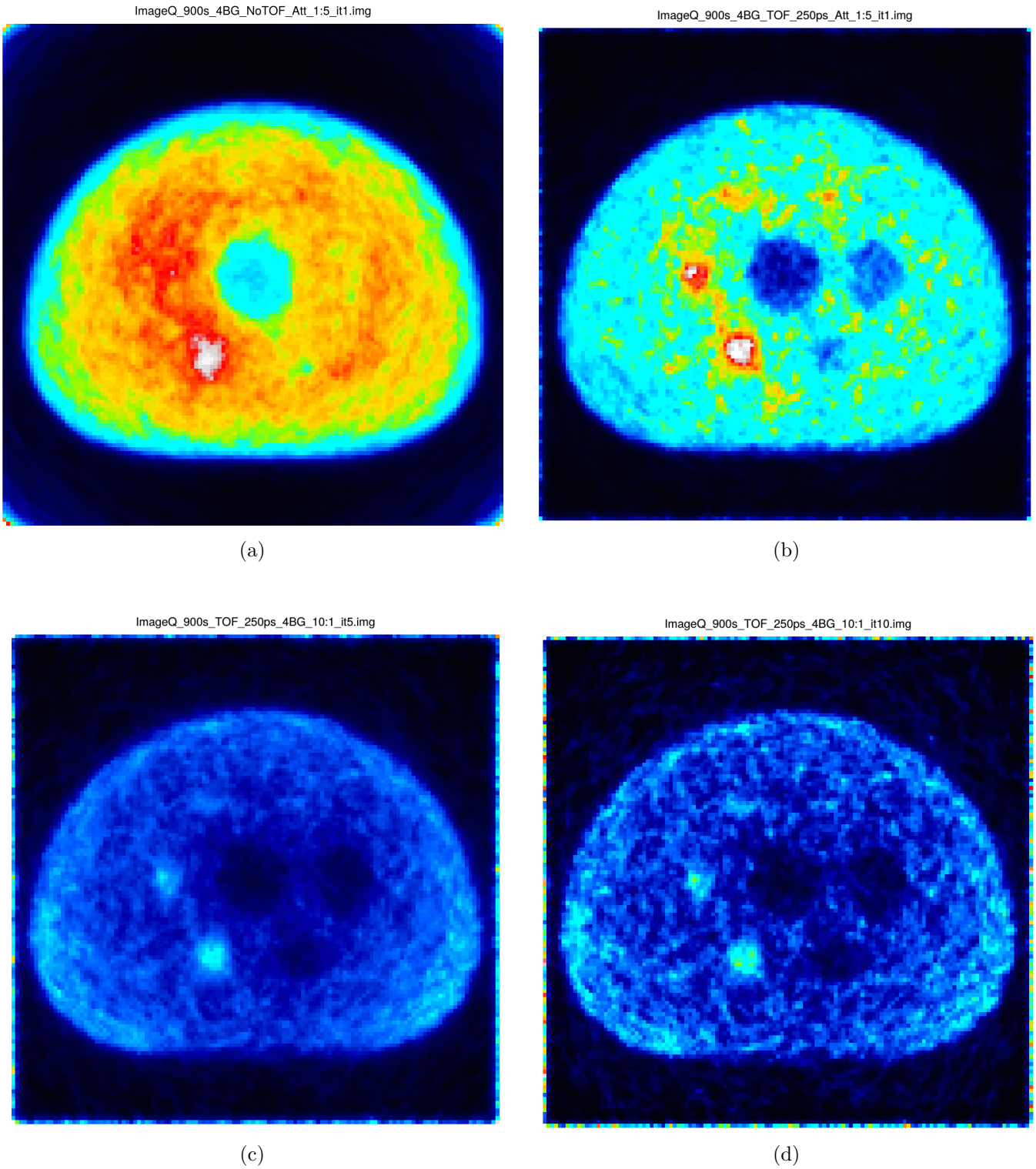

Figure 4.18: Reconstructed images of the Body Phantom NEMA, time of the scanning 900 s associated with Tab. 4.6 in case: (a) without TOF, with attenuation correction, 1st iteration with 5 subsets; (b) resolving time TOF 250 ps with attenuation correction, 1st iteration with 5 subsets; (c) resolving time TOF 250 ps, with attenuation correction, 5th iteration with 1 subset; 4) resolving time TOF 250 ps, with attenuation correction, 10th with 1 subset.

As was discussed in the Section 2.6.4, applying of the Cherenkov photons for creation a PET scanner requires another development of the random correction, which goes beyond the scope of the current study. In order to mitigate the absence of the scatter and random corrections, we reconstructed the PET image by taking into account only true coincidences. Indeed, the reconstruction of such image could be viewed as a reconstruction of all coincidences when perfect random and scatter corrections are applied. Of course, in the real life those corrections are never perfect, but we can reasonably expect that the result of the image reconstruction with random and scatter corrections will be located somewhere between two boundary cases: (1) image produced by all coincidences without any corrections and (2) the image created by only true coincidences. Therefore, Table 4.8 represents the results of the estimation of the contrast recovery coefficients and background variability in case taking into account only true coincidences for two activity concentrations of the hot spheres, 4 and 8 times over the background radioactivity (4xBG and 8xBG). For this estimation we used MLEM reconstruction algorithm and results of the 5th and 10th iterations are shown. As was expected, the increasing of quantity of iteration increases the CRC, but at the cost of the larger background fluctuations.

Furthermore, we studied the influence of the reconstruction parameters such as number of iterations and subsets on the image quality. For example, in case the OSEM reconstruction with 5 subsets, see Fig. 4.20. As once can see in Fig. 4.20a, 4.20c, increasing in CRC always corresponds to the increasing in the background fluctuation. In order, to determine the optimal point, we calculated the signal-to-noise ratio (SNR) defined as:

$$SNR = \frac{Q_{H,j} - Q_{B,j}}{\sigma_j}, \tag{4.7}$$

where $Q_{H,j}$ is average counts in the ROI for sphere j, $Q_{B,j}$ is average counts in a ROI for background, σ_j is standard deviation of the background ROI counts, corresponding to noise in the image. The best CRC is found to be for the first iteration in the case of the 5 subsets.

We also compare the obtained contrast recovery with the conventional hybrid scanner Biograph mMR by Siemens Healthcare [108], see Tab 4.7. As one can see the obtained contrast recovery are smaller than for the conventional scanner, but obtained value are still reasonable to identify all hot sphere at the high contrast (8xBG) and identify the two largest at the low contrast (4xBG).

The influence of the varying reconstruction parameters on image quality is demonstrated for the four smallest spheres in Fig. 4.20. It can be determined that contrast recovery coefficients increase with an increasing number of the iterations at the cost of higher background variability.

Sphere, mm	PECHE scanner		Biograph mMR by Siemens	
	Q_j, [%] 4xBG	Q_j, [%] 8xBG	Q_j, [%], 4xBG (MRI)	Q_j, [%] 4xBG, (CT)
10	5.0	20.6	16.8	30.5
13	11.0	27.0	31.7	50.5
17	16.8	42.6	52.7	72.9
22	21.1	51.3	64.8	74.5
28	61.9	63.1	68.8	56.6
37	69.3	67.6	76.1	64.8

Table 4.7: Contrast recovery factor Q_j cases TOF 180 ps, time of scanning 15 min, initial contrast is 4 and 8 (see Fig. 4.19) in case only true reconstructed coincidences and comparison with conventional scanners MR-based 3.0 Tesla PET/MR hybrid system (Biograph mMR, Siemens Healthcare) and CT-based [108].

Sphere	Activity 4xBG				Activity 8xBG			
	it5		it10		it5		it10	
	Q_j	N_j	Q_j	N_j	Q_j	N_j	Q_j	N_j
10	4.2	10.4	6.1	17.9	19.1	5.1	27.3	20.1
13	9.2	8.6	14.2	14.1	25.5	4.0	36.6	15.3
17	16.1	6.8	19.0	10.7	42.3	3.0	51.4	10.8
22	21.4	5.3	24.8	8.0	53.4	5.1	59.6	7.3
28	61.7	4.7	70.6	7.2	62.5	4.7	70.4	7.0
37	70.5	3.7	78.9	5.1	68.6	4.5	75.8	6.0

Table 4.8: Contrast recovery factorQ_j [%] and background variability N_j [%] of the image containing only true coincidence. Scan time 15 min, attenuation correction is included. Use MLEM reconstruction (no subsets), it5 corresponds to 5th iteration, it10 corresponds to 10th iteration.

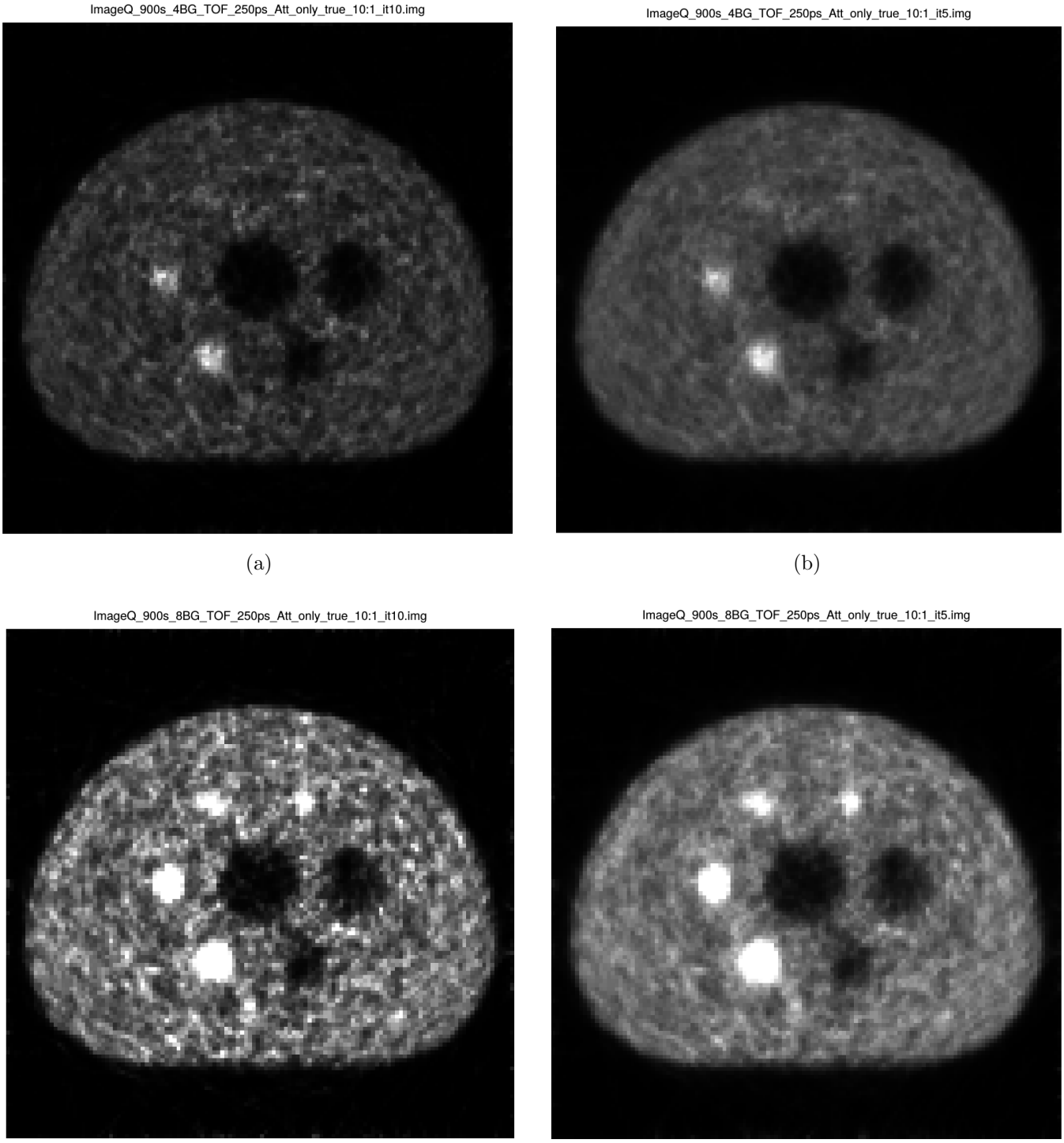

Figure 4.19: Reconstructed images of the Body Phantom NEMA, time of the scanning 900 s associated with Tab. 4.8 in case 10 iterations with 1 subset for only true coincidences (a) initial contrast 4, 10th iteration; (b) initial contrast 4, 5th iteration; (c) initial contrast 8, 10th iteration; (d) initial contrast 8, 5th iteration.

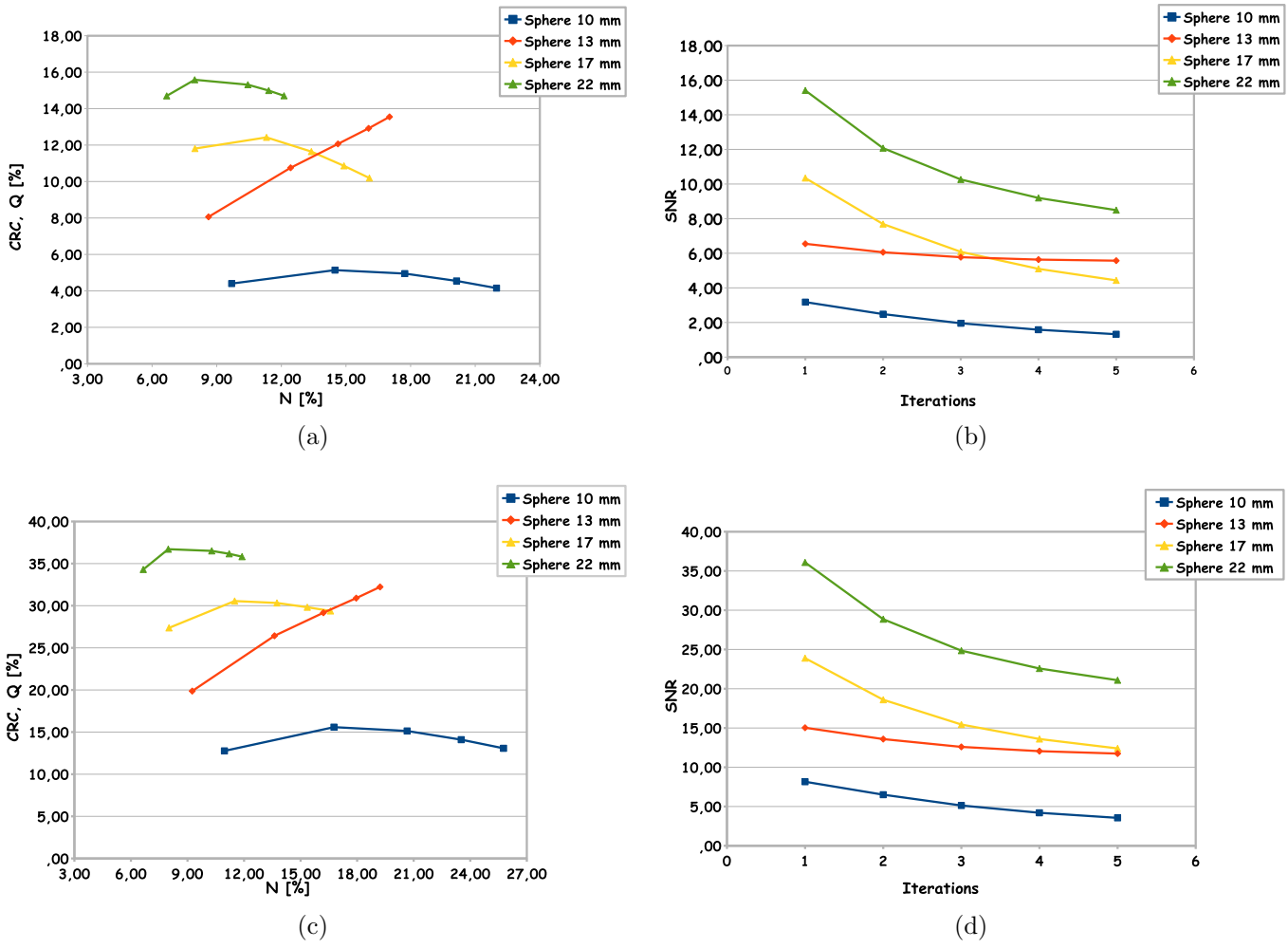

Figure 4.20: (a) Contrast recovery coefficients vs background fluctuation and (b) Signal-to-noise ratio vs iteration number for the initial contrast 4 and (c) and (d) the same for the initial contrast 8. OP-OSEM reconstruction with 5 subsets is used.

Conclusion

The time-of-flight technology has a very high potential to improve positron emission tomography. It increases the signal-to-noise ratio of the reconstructed images and provides the possibility to further improvement of already very high PET scanners sensitivity (the pico-molar level). If the present state-of-the-art coincidence time resolution of about 325 ps could be improved, it allows to get a significant reduction of the dose injected to a patient, and consequently, the possibility to extend the use of the PET scans to new categories of the patients.

The study presented in this manuscript demonstrated that the Cherenkov detection technology could reach the equivalent or even better performance than the conventional technology based on the scintillation crystals. In particular, we estimated that the TOF NECR values of the foreseen Cherenkov scanner are comparable or even better than ones reached by the commercial machine. The image quality parameters, i.e., contrast recovery versus background fluctuation are slightly worse than the chosen example of the commercial scanner, but this comparison still requires further optimization of the reconstruction parameters.

In the same time, the results obtained should be taken with caution. It is well known, that simulation is more often optimistic compare to the real installations. In particular, in our study we should underline the following "delicate" points. First of all, the current simulation of the PMT time response do not take into account any possible tails in the TTS distribution. As was discovered lately, the hardware tests at the IRFU [109] show that such tail exists and could degrade the detector time response. Secondarily, that this simulation assumes the molecular bonding between PMT window and crystal [88]. As was shown in the Section 4.2, such configuration is two times more efficient than the conventional optical interface using optical gel. In the same time, such configuration is technically difficult to realize. Indeed, the main principle of the molecular bonding consists of bringing in contact the PMT sapphire window and PbF_2 crystal, without using any additional material (e.g. optical gel). Such an operation requires surfaces polished to the level of roughness of 1 nm or better and planarity of these surfaces less than 1 μm. In addition, these surfaces must be also free from the dust particles and contamination, especially hydrocarbon films. This procedure was judged too difficult in realization and application on the PMT window, so we consider an another idea: direct deposition of the photocathode layer on the crystal surface and, thus, totally eliminate the total reflection between the photocathode and the crystal. This idea will be studied in the ClearMind project, which has similar performances concerning the Cherenkov radiation detection as ones was obtained in the current work.

Unfortunately, the lead fluoride is a fragile material. Moreover, when PbF_2 crystal is heated to the temperatures necessary for the evaporation of the photocathode

layer, it degases the lead compounds, mainly PbF, toxic for the photocathode deposition. To avoid these problems, the use of the lead tungstate ($PbWO_4$) crystal is proposed. This crystal has a high density (8.8 g/cm^3) and a high atomic number ($Z = 188$). It degases considerably less than PbF_2 and produces almost the same number of the Cherenkov photons. Additionally, it generates a small amount of the scintillation photons, which are relatively fast. This additional light increases the number of the detected optical photons and correspondingly the time resolution, and it also makes possible to measure the deposited energy and reconstruct the position of the gamma interactions using a monolithic crystal. As a continuation of this work it is planned to adjust the simulation for use of monolithic lead tungstate crystals and study the performances of the foreseen whole-body TOF PET scanner.

In this study we demonstrated that the relatively low detection efficiency of the Cherenkov crystals is compensated by the TOF gain due to the high CRT resolution. In the same time, current resolution is limited by the TTS of the existing photomultipliers. Even if the current performance of the Cherenkov scanner does not have sufficient motivation without additional developments, we expect that a continuous improvement of the photo-detection technologies and, in particular time resolution, this approach becomes more interesting either by use of the pure Cherenkov radiators, or by use of the scintillation crystals with a significant production of the Cherenkov light.

Acknowledgements

First of all, we acknowledge the financial support by the LabEx P2IO R&D project of the region Île-de-France, the IDI 2015 project funded by the IDEX Paris-Saclay, ANR-11-IDEX-0003-02, PhD financial support by the French embassy in Ukraine, Programme Transversal Technologies pour la Santé of the CEA, DRI University Paris-Saclay and Taras Shevchenko National University of Kyiv. This work is conducted within the scope of the IDEATE International Associated Laboratory.

In addition, I would like to thank my supervisor Viatcheslav Sharyy and co-supervisor Igor Kadenko for their participation and paying continuous attention to my scientific and non-scientific problems. I gratefully acknowledge the best group CaLIPSO at the IRFU for their patience and help in overcoming numerous obstacles I have been facing through my PhD research. Many thanks to the IRFU for its working and friendly atmosphere.

I am very grateful to Achille Stocchi, Gérard Montarou, Klaus Peter Schäfers and Oleg Bezshyyko for accepting to be part of the jury and their edits and corrections for this thesis.

Larisa Golinka-Bezshyyko deserves a lot of gratefulness for her advice.

I would like to thank all my friends for staying by my side and sharing various moments of my life.

Last but not the least, I would like to thank my family: my lovely and patient husband, my wonderful daughter and my super parents for incredible supporting me throughout writing this thesis and my existence in general.

Bibliography

[1] R. Bar-Shalomab, A. Y. Valdivia, and M. D. Blaufox, "PET Imaging in Oncology," *Sem Nucl Med*, vol. 30, pp. 150–185, 2000.

[2] E. de Groot *et al.*, "Optimized dose regimen for whole-body FDG-PET imaging," *EJNMMI Research*, vol. 3, no. 1, p. 63, 2013.

[3] B. Huang, M. W.-M. Law, and P.-L. Khong, "Whole-Body PET/CT Scanning: Estimation of Radiation Dose and Cancer Risk," *Radiology*, vol. 251, no. 1, pp. 166–174, 2009, pMID: 19251940.

[4] R. Campagnolo, P. Garderet, and J. Vacher, "Tomographie par emetteurs positrons avec mesure de temps de vol," *In Proc. Commun. au Colloque National sur le Traitement du Signal, Nice, France*, May 1979.

[5] T. Tomitani, "Image Reconstruction and Noise Evaluation in Photon Time-of-Flight Assisted Positron Emission Tomography," *IEEE Trans Nucl Sci*, vol. 28, no. 6, pp. 4581–4589, 1981.

[6] Ter-Pogossian *et al.*, "Photon Time-of-flight-assisted Positron Emission Tomography," *J Comp As Tom*, vol. 5, pp. 227–239, April 1981.

[7] Ter-Pogossian, *et al.*, "Super PETT I: A Positron Emission Tomograph Utilizing Photon Time-of-Flight Information," *IEEE Trans Med Imag*, vol. 1, no. 3, pp. 179–187, Nov 1982.

[8] M. Yamamoto, D. Ficke, and M. Ter-Pogossian, "Experimental Assessment of the Gain Achieved by the Utilization of Time-of-Flight Information in a Positron Emission Tomograph "(Super PETT I)"," *IEEE Trans Med Imag*, vol. 1, no. 3, pp. 187–192, Nov 1982.

[9] T. F. Budinger, "Time-of-Flight Positron Emission Tomography: Status Relative to Conventional PET," *J Nucl Med*, vol. 24, no. 1, p. 73, 1983.

[10] A. Mallon and P. Grangeat, "Three-dimensional PET Reconstruction With Time-of-flight Measurement," *Phys Med Biol*, vol. 37, no. 3, pp. 717–729, 1992.

[11] Vereos Digital PET-CT, Philips U.S.A.

[12] M. Berger *et al.*, "NIST Standard Reference Database 8 (XGAM)," https://www.nist.gov/pml/xcom-photon-cross-sections-database.

[13] S. Korpar *et al.*, "Study of TOF PET Using Cherenkov Light," *Nucl Instrum Meth A*, vol. 654, no. 1, pp. 532–538, 2011.

[14] S. Korpar *et al.*, "Study of TOF PET Using Cherenkov Light," *Physics Procedia*, vol. 37, pp. 1531–1536, 2012, Proceedings of the 2nd International Conference on Technology and Instrumentation in Particle Physics (TIPP 2011).

[15] S. Korpar *et al.*, "Study of a Cherenkov TOF-PET Module," *Nucl Instrum Methods Phys Res*, vol. 732, pp. 595–598, 2013, Vienna Conference on Instrumentation 2013.

[16] S. Ziegler, "Positron Emission Tomography: Principles, Technology, and Recent Developments," *Nucl Phys A*, vol. 752, pp. 679c–687c, 2005.

[17] D. L. Miller and D. Schauer, "The ALARA Principle in Medical Imaging," *AAPM Newsletter*, vol. 40, no. 1, pp. 38–40, 2015.

[18] M. Larobina, A. Brunetti, and M. Salvatore, "Small animal PET: a review of commercially available imaging systems," *Curr Med Imag Rev*, vol. 2, no. 2, May 2006.

[19] H. W. A. M. de Jong *et al.*, "Performance evaluation of the ECAT HRRT: an LSO-LYSO double layer high resolution, high sensitivity scanner," *Phys Med Biol*, vol. 52, no. 5, p. 1505, February 2007.

[20] C. Weirich *et al.*, "Simultaneous PET and MR Imaging with a Newly Developed 3TMR-BrainPET Scanner," *CEUR Workshop Proceedings*, pp. 201–205, 2010.

[21] V. Bettinardi *et al.*, "Physical Performance of the New Hybrid PET/CT Discovery-690," *Med Phys*, vol. 38, no. 10, pp. 5394–5411, 2011.

[22] IAEA, "Cyclotron Produced Radionuclides: Principles and Practice," *Technical Reports Series No. 465*, 2008.

[23] G. Saha, *Fundamentals of nuclear pharmacy*, 5th ed. Springer, New York, 2004.

[24] G. Saha, W. MacIntyre, and R. Go, "Cyclotrons and positron emission tomography radiopharmaceuticals for clinical imaging," *Semin Nucl Med*, vol. 22, pp. 150–161, 1992.

[25] D. L. Bailey *et al.*, *Positron Emission Tomography Basic Sciences*. Springer, London, 2005.

[26] B. Bendriem and D. Townsend, *The Theory and Practice of 3D PET*. Kluwer Academic Publishers, 1998.

[27] O. Klein and Y. Nishina, "Über die Streuung von Strahlung durch freie Elektronen nach der neuen relativistischen Quantendynamik von Dirac," *Z Physik*, vol. 52, pp. 853–868, 1928.

[28] J. H. Hubbell, "Review of photon interaction cross section data in the medical and biological context," *Phys Med Biol*, vol. 44, pp. R1–R22, 1999.

[29] E. Hecht, *Optics*, 5th ed. Pearson Education Limited, England, 2017.

[30] GEANT4 Collaboration, *Geant4 User's Guide for Application Developers*, 6 Dec 2013, version: geant4 10.0.

[31] A. Levin and C. Moisan, "A More Physical Approach to Model the Surface Treatment of Scintillation Counters and its Implementation into DETECT," *TRIUMF Preprint TRI-PP-96-64*, 1996.

[32] P. Cerenkov, "Visible Radiation Produced by Electrons Moving in a Medium with Velocities Exceeding that of Light," *Phys Rev*, vol. 52, p. 378, 1937.

[33] V. Jelle, "Cerenkov Radiation and Its Applications," *Br J Appl Phys*, vol. 6, pp. 227–232, 1955.

[34] G. Collins and V. Reiling, "Cerenkov Radiation," *Phys Rev*, vol. 54, pp. 499–503, 1938.

[35] National Electrical Manufacturers Association, "Performance Measurements of Positron Emission Tomographs," *NEMA NU 2-2007*, 2007.

[36] T. F. Budinger, "PET instrumentation: what are the limits?" *Sem Nucl Med*, vol. 28, pp. 247–267, 1998.

[37] https://explorer.ucdavis.edu/about explorer.

[38] G. Bolard *et al.*, "Performance comparison of two commercial BGO-based PET/CT scanners using NEMA NU 2-2001," *Med Phys*, vol. 34, pp. 2708–2717, 2007.

[39] C. Melcher and J. Schweitzer, "Cerium-doped lutetium oxyorthosilicate: a fast, efficient new scintillator," *IEEE Trans Nucl Sci*, vol. 4, pp. 502–505, 1992.

[40] Y. Hirano, K. Koshino, and H. Iida, "Influences of 3d PET scanner components on increased scatter evaluated by a monte carlo simulation," *Phys Med Biol*, vol. 62, no. 10, pp. 4017–4030, apr 2017.

[41] M. Gaens *et al.*, "GPU-accelerated Monte Carlo based scatter correction in brain PET/MR," *EJNMMI Phys*, vol. 1, no. 1, p. A32, Jul 2014.

[42] C. H. Holdsworth *et al.*, "Evaluation of a Monte Carlo scatter correction in clinical 3D PET," *2003 IEEE Nucl Sci Symposium. Conference Record (IEEE Cat. No.03CH37515)*, vol. 4, pp. 2540–2544, Oct 2003.

[43] D. Bailey, T. Jones, and T. Spinks, "A Method for Measuring the Absolute Sensitivity of Positron Emission Tomographic Scanners," *Eur J Nucl Med*, vol. 18, pp. 374–379, 1991.

[44] G. Saha, *Basics of PET Imaging Physics, Chemistry, and Regulations*, 2nd ed. Springer, London, 2010.

[45] A. Braem *et al.*, "Feasibility of a novel design of a high resolution parallax-free compton enhanced pet scanner dedicated to brain research," *Phys Med Biol*, vol. 49, pp. 1–16, 2004.

[46] G. Knoll, *Radiation detection and measurement*, 2nd ed. John Wiley & Sons, 1989.

[47] D. Yvon *et al.*, "CaLIPSO: A novel detector concept for positron annihilation detection," in *Proc. 3rd Int Advancements in Nuclear Instrumentation Measurement Methods and their Applications (ANIMMA) Conf*, Jun. 2013, pp. 1–9.

[48] D. Townsend *et al.*, "High-density avalanche chamber (HIDAC) positron camera," *J Nucl Med*, vol. 28, pp. 1554–1562, 1987.

[49] A. Jeavons, R. Chandler, and C.A.R. Dettmar, "A 3D HIDAC-PET camera with sub-millimetre resolution for imaging small animals," *IEEE Trans Nucl Sci*, vol. 46, pp. 468–473, 1999.

[50] K. Bolwin *et al.*, "Development of a clear sub-millimeter small animal PET scanner by reducing the influence of the non-collinearity effect," *Journal of Instrumentation*, vol. 12, no. 03, p. C03006, 2017.

[51] D. L. Thorek *et al.*, "Cerenkov imaging - a new modality for molecular imaging," *Am J Nucl Med Mol Imag*, vol. 2, no. 2, p. 163, 2012.

[52] M. Miyata *et al.*, "Development of TOF-PET using Cherenkov Radiation," *J Nucl Sci Technol*, vol. 43, no. 4, pp. 339–343, 2006.

[53] S. E. Brunner *et al.*, "Studies on the Cherenkov Effect for Improved Time Resolution of TOF-PET," *IEEE Trans Nucl Sci*, vol. 61, no. 1, pp. 443–447, February 2014.

[54] OpenGATE collaboration, *Users Guide V6.2, GATE collaborative documentation wiki*, 31 Jan 2013, Version: GATE 6.2.

[55] K. Iniewski, *Medical Imaging. Principles, Detectors, and Electronics*, 2nd ed. John Wiley & Sons, Inc., Hoboken, New Jersey, 2009.

[56] "CASToR: a generic data organization and processing code framework for multi-modal and multi-dimensional tomographic reconstruction," *Phys Med Biol*, vol. 63, no. 18, p. 5505, September 2018.

[57] http://www.castor-project.org.

[58] L. A. Shepp and Y. Vardi, "Maximum Likelihood Reconstruction for Emission Tomography," *IEEE Trans Med Imag*, vol. 1, no. 2, pp. 113–122, 1982.

[59] K. V. Slambrouck *et al.*, "Bias Reduction for Low-Statistics PET: Maximum Likelihood Reconstruction With a Modified Poisson Distribution," *IEEE Trans Med Imag*, vol. 34, no. 1, pp. 126–136, 2015.

[60] C. Byrne, "Iterative algorithms for deblurring and deconvolution with constraints," *Inverse Problems*, vol. 14, no. 6, pp. 1455–1467, 1998.

[61] L. Landweber, "An Iteration Formula for Fredholm Integral Equations of the First Kind," *Am J of Math*, vol. 73, pp. 1615–624, 1951.

[62] H. Zaidi and B. Hasegawa, "Determination of the Attenuation Map in Emission Tomography," *J Nucl Med*, vol. 44, pp. 291–315, 2003.

[63] S. R. Cherry *et al.*, "Total-Body PET: Maximizing Sensitivity to Create New Opportunities for Clinical Research and Patient Care," *J Nucl Med*, vol. 59, no. 1, pp. 3–12, Jan. 2018.

[64] E. C. Ehman *et al.*, "PET/MRI: Where Might It Replace PET/CT?" *International Society for Magnetic Resonance in Medicine*, vol. 46, no. 5, pp. 1247–1262, 2017.

[65] A. Mehranian and H. Zaidi, "Impact of time-of-flight PET on quantification errors in MR imaging-based attenuation correction," *J Nucl Med*, p. 635641, 2015.

[66] M. Conti, "Effect of Randoms on Signal-to-Noise Ratio in TOF PET," *IEEE Trans Nucl Sci*, vol. 53, no. 3, pp. 1188–1193, June 2006.

[67] S. Vandenberghe *et al.*, "Recent Developments in Time-of-flight PET," *EJNMMI Physics*, vol. 3, no. 1, pp. 1–30, 2016.

[68] P. Lecoq, "Pushing the Limits in Time-of-Flight PET Imaging," *IEEE Trans Rad Pl Med Sci*, vol. 1, no. 6, pp. 473 – 485, 2017.

[69] D. Sarrut *et al.*, "A review of the use and potential of the GATE monte carlo simulation code for radiation therapy and dosimetry applications," *Med Phys*, vol. 41, no. 6, p. 064301, 2014.

[70] http://www.opengatecollaboration.org.

[71] S. Jan *et al.*, "GATE: a simulation toolkit for PET and SPECT," *Phys Med Biol*, vol. 49, no. 19, pp. 4543–4561, 2004.

[72] G. Santin *et al.*, "Evolution of the GATE project: new results and developments," *Nuclear Physics B-Proceedings Supplements*, vol. 172, pp. 101–103, 2007.

[73] S. Jan *et al.*, "GATE V6: a major enhancement of the GATE simulation platform enabling modelling of CT and radiotherapy," *Phys Med Biol*, vol. 56, no. 4, pp. 881–901, 2011.

[74] J. Strydhorst and I. Buvat, "Redesign of the GATE PET coincidence sorter," *Phys Med Biol*, no. 61, pp. N522–N531, 2016.

[75] I. Martinez-Rovira, C. Jouvie, and S. Jan, "Implementation of biological washout processes within GATE/Geant4-A Monte Carlo study in the case of carbon therapy treatments," *Med Phys*, no. 42, pp. 1773–1778, 2015.

[76] V. Cuplov *et al.*, "Extension of the gate monte-carlo simulation package to model bioluminescence and fluorescence imaging," *J Biomed Opt*, vol. 19, no. 2, pp. 026 004–026 004, 2014.

[77] Q. Pham *et al.*, "Coupling of Geant4-DNA physics models into the GATE Monte Carlo platform: Evaluation of radiation-induced damage for clinical and preclinical radiation therapy beams," *Nucl Instr Meth Phys Res Sect B: Beam Interact Mater. Atoms*, no. 353, pp. 46–55, 2015.

[78] A. Mittone *et al.*, "An efficient numerical tool for dose deposition prediction applied to synchrotron medical imaging and radiation therapy," *J Synchrotron Radiat.*, no. 59, pp. 785–792, 2013.

[79] F. Lamare *et al.*, "Validation of a Monte Carlo simulation of the Philips Allegro/GEMINI PET systems using GATE," *Med Phys*, vol. 51, no. 4, pp. 943–962, 2006.

[80] C. R. Schmidtlein *et al.*, "Validation of GATE Monte Carlo simulations of the GE Advance/Discovery LS PET scanners," *Med Phys*, vol. 33, no. 1, pp. 198–208, 2006.

[81] P. Gonias *et al.*, "Validation of a GATE model for the simulation of the Siemens biographTM 6 PET scanner," *Nucl Instr Meth Phys Res A*, vol. 571, no. 1-2, pp. 263–266, 2007.

[82] F. Baldacci *et al.*, "A track length estimator method for dose calculations in low-energy x-ray irradiations: implementation, properties and performance," *Med Phys*, no. 25, pp. 36–47, 2015.

[83] F. Smekens *et al.*, "Split exponential track length estimator for Monte-Carlo simulations of small-animal radiation therapy," *Phys Med Biol*, no. 59, pp. 7703–7715, 2014.

[84] A. Kantz and R. Hofstadter, "Large Scintillators, Cerenkov counters for high energies," *Nucleonics (U.S.)*, vol. 12, no. 3, March 1954.

[85] E. Dally and R. Hofstadter, "A lead fluoride Cerenkov shower counter," *Rev Sci Instr*, vol. 658, no. 39, 1968.

[86] D. Anderson, Y. Kobayashi, M. Yoshimura, and C. Woody, "Lead Fluoride: An Ultracompact Cherenkov Radiator for EM Calorimetry," *Nucl Instrum Meth Phys Res*, vol. 290, pp. 385–389, 1990.

[87] Dolenec, R. and Korpar, S. and Križan, P. and Pestotnik, R., "Cherenkov TOF PET with silicon photomultipliers," *Nucl Instr Meth Phys Res Sect A: Acc Spect Det and Assoc*, vol. 804, pp. 127–131, 2015.

[88] CEA, "Detecteur de photons a haute energie," France French Patent N 1 361 037, BD15 034SG, 12 Nov 2013.

[89] H. Moriceau *et al.*, "Low temperature direct bonding: An attractive technique for heterostructures build-up," *Microelectronics Reliability*, vol. 52, no. 2, pp. 331 – 341, 2012, low Temperature Processing for Microelectronics and Microsystems Packaging.

[90] J. G. Timothy, *Microchannel plates for photon detection and imaging in space.* Springer New York, 2013.

[91] K. Blodgett, "Surface conductivity of lead silicate glass after hydrogen treatment," *J Am Ceram Soc*, vol. 34, pp. 14–27, 1951.

[92] P. Oschepkov *et al.*, "Application of a continuous secondary electron multiplication for amplifying small currents (Translation)," *Pribory Tekh Eksper*, vol. 4, pp. 89–91, 1960.

[93] G. Goodrich and W. Wiley, "Continuous channel electron multiplier," *Rev. Sci. Instrum.*, vol. 33, pp. 761–762, 1962.

[94] J. Adams and B. Manley, "The mechanism of channel electron multiplication," *IEEE Trans Nucl Sci*, vol. 13, pp. 88–89, 1966.

[95] W. Wiley and C. Hendee, "Electron multipliers utilizing continuous strip surfaces," *IEEE Trans Nucl Sci*, vol. 9, pp. 103–106, 1962.

[96] O. Siegmund *et al.*, "Microchannel plates: recent advances in performance," vol. 6686, p. 66860W, Sep. 2007.

[97] D. Washington *et al.*, "Technology of channel plate manufacture," *Acta Electronica*, vol. 14, pp. 201–224, 1971.

[98] T. Gys, "Micro-channel plates and vacuum detectors," *Nucl Instrum Meth A*, vol. 787, pp. 254–260, 2015.

[99] https://www.photonis.com.

[100] https://www.hamamatsu.com.

[101] PHOTONIS USA Pennsylvania, Inc. (2013, January) PLANACON XP85012 Datasheet. www.photonisusa.com.

[102] Nye Lubricants, Inc., "Nye Datasheet OCF-452: An optical fluid with a refractive index of 1.52 at 589.3 nm ," www.nyeoptical.com.

[103] C. Canot *et al.*, "Development of the Fast and Efficient Gamma Detector Using Cherenkov Light for TOF-PET," *Proceedings of iWoRiD 2017 International Workshop on Radiation Imaging Detectors*, 2017.

[104] KETEK GmbH. KETEK PM3350 Datasheet. www.ketek.net.

[105] OpenGATE collaboration, *Users Guide V7.1, GATE collaborative documentation wiki*, 26 March 2015, Version: GATE 7.1.

[106] Strother, S.C. and Casey, M.E. and Hoffman, E.J. , "Measuring PET Scanner Sensitivity: Relating Count-Rates to Image Signal-to-Noise Ratios Using Noise Equivalent Counts," *IEEE Trans Nucl Sci*, vol. 37, pp. 783–388, 1990.

[107] C. Rueden, the ImageJ development team at the Laboratory for Optical, and C. I. L. at the University of Wisconsin-Madison, https://fiji.sc.

[108] S. Ziegler *et al.*, "NEMA image quality phantom measurements and attenuation correction in integrated PET/MR hybrid imaging," *EJNMMI Physics*, vol. 2, pp. 1–14, 2003.

[109] C. Canot, "Détecteur Cherenkov de gamma 511 keV, rapide et efficace, pour la Tomographie par Emission de Positrons," *PhD Thesis, University Paris-Saclay*, 2018.

université PARIS-SACLAY | ÉCOLE DOCTORALE PHENIICS

Titre: Conception du scanner TEP Tchérenkov, corps entier, temps de vol en utilisant un logiciel de simulation GATE

Mots clés: TEP; temps-de-vol; imagerie médicale; rayonnement Tchérenkov

Résumé: Dans cette thése, nous présentons la conception et l'étude de performance d'un tomographe par émission de positrons (TEP) corps entier utilisant la radiation Chérenkov avec capacité de temps-de-vol (projet PECHE). Nos résultats et les conclusions sont basées sur la simulation GATE pour la configuration du scanner suivante: cristal de fluorure de plomb attaché à un photomultiplicateur à micro-canaux. C'est un cristal de haute densité, transparent pour les photons ultraviolet, et posséde la fraction photoélectrique la plus élevé de 46 %. Le photomultiplicateur choisi est un détecteur de grande taille, rapide et pixélisé avec une efficacité quantique raisonnable, de 25 % à une longueur d'onde de 400nm. Grâce à ces propriétés, il est possible d'envisager un détecteur efficace de gamma de 511 keV avec une épaisseur de cristal de 10 mm (une longueur d'interaction) et donc de minimiser la longueur et dispersion des trajectoires de photons, résultant à une résolution temporelle optimisée. Nous avons étudié les configurations différentes de détecteur élémentair tels que le cristal avec les épaisseurs de 10 et 20 mm, le diamétre de l'anneau de détection de 80 et 90 cm, diverses options de le revêtement de cristal (noir, blanc diffus et poli) et deux interfaces optiques (collage moléculaire et assemblage conventionnel avec un gel optique). Pour une configuration optimale, nous avons choisi un scanner TEP à trois anneaux avec un diamétre de l'anneau de 80 cm, cristal de 10 mm d'épaisseur, et un blindage en plomb. Nous avons estimé le potentiel du scanner envisagé en utilisant les tests recommandés par la norme NEMA NU 2-2007. En particulier, nous avons évalué le taux de comptage de bruit équivalent (NECR), la résolution spatial, coefficients de recouvrement de contraste de l'image et la variabilité de bruit de fond pour le fantôme de qualité d'image. La reconstruction des images est faite en utilisant l'algorithme itératif temps-de-vol implémenté dans la plate-forme de reconstruction "open source" CASToR récemment développée. Nous avons conclu que un scanner corps entier utilisant la lumiére Chérenkov pourrait atteindre des performances comparables à celles d'un tomographe classique à scintillation grâce à son excellente résolution temps-de-vol. L'utilisation du rayonnement Chérenkov permet d'atteindre une résolution en temps-de-vol encore meilleure. Les limitations physiques identifiés dans cette étude seront abordées dans le développement du futur photodétecteur amélioré utilisant le radiateur $PbWO_4$.

Title: Design of the Cherenkov TOF whole-body PET scanner using GATE simulation

Keywords: PET; time-of-flight; medical imaging; Cherenkov radiation

Abstract: In this thesis we present the conception and performance studies of the foreseen Cherenkov whole-body positron emission scanner with time-of-flight potential. Our results and conclusions are based on the GATE simulations for the following scanner configuration: lead fluoride crystal coupled with micro-channel-plate photomultiplier (MCP-PMT). This crystal is characterized by a high density, transparency for photons in ultraviolet region, and one of the highest photoelectric fraction of about 46 %. The chosen photomultiplier is a fast, large size, pixelized detector with reasonable quantum efficiency, 25 % for 400 nm photon wavelength. Due to these properties, it is possible to create an efficient 511-keV gamma detector with a thin crystal of the order of 10 mm thick (one interaction length) and hence minimize the length and dispersion of the photon trajectories, leading to better timing resolution. We considered different configurations of the elementary detectors such as crystal thicknesses of about 10 and 20 mm, diameter of the detector ring 80 and 90 cm, various options of the crystal coating (black, diffuse white and polished) and two optical interfaces (molecular bonding and assembling with an optical gel). As an optimal configuration was chosen three-ring PET scanner with diameter of the ring 80 cm and a 10 mm-thick crystal, protected with lead shielding. Each ring consists of 43 blocks of detectors. We estimated the potential of the foreseen scanner following the prescription of the NEMA NU 2-2007 standard. In particular, we evaluated the Noise Equivalent Count Rate, spatial resolution, image contrast recovery coefficients versus background variability for the NEMA image quality phantom. Reconstruction of images is done using iterative TOF algorithm implemented in the recently developed open source reconstruction platform CASToR. We concluded that due to an excellent TOF resolution a crystal-based Cherenkov whole-body scanner could achieve performances comparable with a conventional, scintillation-based tomograph. The limitations identified in this study will be addressed to the future developments of the improved photodetector using the $PbWO_4$ radiator.

Université Paris-Saclay
Espace Technologique / Immeuble Discovery
Route de l'Orme aux Merisiers RD 128 / 91190 Saint-Aubin, France